



HAL
open science

Patterning and characterization of polymer nanostructures for optical biosensing

Miguel Diez

► **To cite this version:**

Miguel Diez. Patterning and characterization of polymer nanostructures for optical biosensing. Micro and nanotechnologies/Microelectronics. Univ. Bordeaux, 2018. English. NNT: . tel-02519389

HAL Id: tel-02519389

<https://hal.science/tel-02519389>

Submitted on 28 Mar 2020

HAL is a multi-disciplinary open access archive for the deposit and dissemination of scientific research documents, whether they are published or not. The documents may come from teaching and research institutions in France or abroad, or from public or private research centers.

L'archive ouverte pluridisciplinaire **HAL**, est destinée au dépôt et à la diffusion de documents scientifiques de niveau recherche, publiés ou non, émanant des établissements d'enseignement et de recherche français ou étrangers, des laboratoires publics ou privés.

THÈSE PRÉSENTÉE
POUR OBTENIR LE GRADE DE
DOCTEUR DE
L'UNIVERSITÉ DE BORDEAUX

ÉCOLE DOCTORALE DES SCIENCES PHYSIQUES ET DE L'INGENIEUR
SPÉCIALITÉ ÉLECTRONIQUE

Par Miguel DIEZ

**Patterning and characterization of polymer nanostructures for
optical biosensing**

Sous la direction de : Corinne DEJOUS
Co-directeurs : Laurent OYHENART, Simon JOLY

Soutenue le 20 décembre 2018

Membres du jury:

M ^{me} DE FORNEL, Frédérique	Directrice de Recherche, ICB, UB	Présidente
M ^{me} BARDINAL, Véronique	Directrice de Recherche, LAAS, CNRS	Rapporteur
M CHOLLET, Franck	Professeur des Universités, Femto-ST, UST	Rapporteur
M RAIMBAULT, Vincent	Chargé de recherche, LAAS, CNRS, UPS	Examineur
M KRIBICH, Raphaël Kada	Maître de Conférences, IES, UM2	Examineur
M ^{me} DEJOUS, Corinne	Professeur des Universités, IMS, Bx INP	Directrice de thèse
M JOLY, Simon	Maître de Conférences, IMS, UBx	Co-directeur de thèse
M OYHENART, Laurent	Maître de Conférences, IMS, UBx	Co-directeur de thèse

Titre : Patterning and characterization of polymer nanostructures for optical biosensing

Résumé :

Les guides d'ondes optiques, les résonateurs en anneau et les coupleurs à réseau fabriqués à partir de polymères nanostructurés sont maintenant considérés comme des technologies prometteuses pour les systèmes de détection biophotoniques intégrés. De manière générale, la structuration des polymères à une échelle inférieure au micron nécessite l'utilisation d'équipements très coûteux tels que la lithographie par faisceau d'électrons. De nos jours, la structuration directe et rapide de dispositifs polymères à indice de réfraction élevé sur CYTOP est réalisable et fournit des guides d'ondes symétriques en contact avec l'eau. De plus, la transparence des polymères rend ces dispositifs adaptés à un fonctionnement dans le visible, étant d'un intérêt majeur pour la biophotonique. Dans cette thèse, nous proposons deux axes de recherche: le processus de fabrication et de caractérisation de nanostructures polymères sub-longueur d'onde sur CYTOP ainsi qu'une démonstration théorique de l'utilisation de ces structures pour la micro-spectrométrie visible. Les nanostructures optiques proposées sont composées d'un résonateur optique avec des coupleurs de réseaux sub-longueur d'onde. Les périodes du réseau sont inférieures à 300nm de manière à coupler efficacement la lumière, sur un seul ordre de diffraction, dans des guides d'ondes monomodes de 350nm x 350nm. L'ensemble du dispositif est imprimé en une seule étape à l'aide d'une méthode de lithographie dite à empreinte douce (NanoImprintLithography) qui consiste à comprimer un tampon sur une couche de polymère. Le dispositif fabriqué présente une couche résiduelle minimale (<50 nm) obtenue grâce à une conception spécifique du tampon principal afin d'améliorer le flux de polymère lors de la phase de compression. Les différentes caractérisations effectuées, à la fois sur la couche de polymère et sur le dispositif imprimé, montrent un bon accord avec les valeurs prédites par simulation. Cependant, une caractérisation ellipsométrique rigoureuse du coefficient thermo-optique suggère différents mécanismes d'instabilité de ces dispositifs sous cyclage thermique. Les performances de ces dispositifs en tant que micro-spectromètres à absorption sont démontrées analytiquement et par simulation, quelle que soit la plate-forme ou la longueur d'onde d'utilisation. Finalement, outre la description du processus de fabrication, nous fournissons un ensemble de règles de conception basées sur l'optimisation théorique du résonateur en anneau pour la mesure du coefficient d'absorption d'un liquide.

Mots clés : Nanostructures, polymères, optique guidée, nanoimpression, biocapteur

Title : Patterning and characterization of polymer nanostructures for optical biosensing

Abstract :

Optical waveguides, ring resonators and grating couplers based on polymer nanostructures are now considered as promising technologies for integrated biophotonic sensing systems. Commonly, the patterning of polymers at the sub-micron scale requires the use of time and cost-consuming equipments such as electron beam lithography. Direct patterning of high refractive index polymer devices on CYTOP is now achievable and provides symmetric waveguides with top water-like claddings. In addition, transparency of polymers makes them suitable for operation in the visible range, being of major interest for biophotonic applications. In this thesis, we report on two main topics: the fabrication process of sub-wavelength polymer nanostructures on CYTOP and the potential sensing capabilities of these structures as visible microspectrometers. The optical nanostructures consist in an optical microring resonator with sub-wavelength gratings to efficiently couple the light inside the photonic circuit. Periods shorter than 300nm are patterned to efficiently couple the input light into 350nm x 350nm waveguides allowing single-mode operation. The whole device is imprinted in a single step using soft imprint lithography called NanoImprint Lithography. We obtain a minimal residual layer (<50nm) which is achieved with a dedicated design of the master stamp to enhance the polymer flow during the pressure step. The different characterizations performed on both polymer layer and the imprinted device show good agreement with the predicted values by simulation. However, rigorous ellipsometry characterization of the thermo-optic coefficient suggest different instability mechanism of these devices under thermal cycling. The performance of these devices as absorption micro-spectrometers is demonstrated analytically regardless the platform or wavelength. Finally, in addition to the fabrication process we provide a set of design rules based on the theoretical optimization of the ring resonator for absorption sensing.

Keywords : Nanostructures, polymers, integrated optic, nanoimprint lithography biosensor

Unité de recherche

Laboratoire de l'Intégration du Matériau au Système (IMS)
UMR CNRS 5218
351 Cours de la Libération
33405 Talence Cedex
France

Declaration of Authorship

I, Miguel DIEZ, declare that this thesis titled, "Patterning and characterization of polymer nanostructures for optical biosensing" and the work presented in it are my own. I confirm that:

- This work was done wholly or mainly while in candidature for a research degree at this University.
- Where any part of this thesis has previously been submitted for a degree or any other qualification at this University or any other institution, this has been clearly stated.
- Where I have consulted the published work of others, this is always clearly attributed.
- Where I have quoted from the work of others, the source is always given. With the exception of such quotations, this thesis is entirely my own work.
- I have acknowledged all main sources of help.
- Where the thesis is based on work done by myself jointly with others, I have made clear exactly what was done by others and what I have contributed myself.

Signed:

Date:

"The best way to predict your future is to create it."

Abraham Lincoln

Acknowledgements

Contents

Declaration of Authorship	i
Acknowledgements	v
Introduction générale	1
General introduction	5
1 Optical structures for visible light wave guiding	7
1.1 Overview	7
1.2 State of the art	11
1.2.1 Why visible photonics?	12
1.2.2 Integrated spectrometers based on colorimetric reaction	12
1.2.3 Integrated photonics platforms for visible wavelength operation	13
1.2.4 Polymer nanostructures for visible light wave-guiding	14
1.2.5 Metal-dielectric integrated based structures and Fano resonances	15
1.3 Previous work	16
1.4 Scope of this thesis	18
2 Basis: Modeling, materials and fabrication	21
2.1 Nanofabrication tools for polymer patterning	22
2.2 Electron beam lithography	23
2.2.1 Organic resist	24
2.2.2 Refractive ion etching	25
2.2.3 Beam energy	26
2.2.4 Master stamp materials	28
2.2.5 EBL Resist choice	29
2.2.6 Process flow for multi-height master stamps	30
2.3 Nanoimprint lithography	32
2.3.1 Surface treatment: Anti-sticking and adhesion enhancement	33
2.3.2 The low index cladding	34
2.3.3 Soft-imprint lithography	34
2.3.4 Intermediate soft stamp materials	35
2.3.5 Defects associated to the soft stamp	37
2.3.6 Curable polymers for waveguide fabrication	38
2.3.7 Squeeze flow of thin films	40

2.3.8	Desired process flow	41
2.4	Integrated photonic devices: Design considerations	44
2.4.1	Main considerations concerning the simulation tool	45
2.5	Polymer waveguides:	47
2.5.1	Single mode operation	47
2.5.2	Waveguide bandwidth	49
2.6	Grating coupler	49
2.6.1	Effect of the period on the effective index	51
2.6.2	Effect of the input angle on the effective index	52
2.6.3	Calculation of the diffraction angle	53
2.6.4	Etch depth	55
2.6.5	Duty Cycle variation	56
2.6.6	Influence of the RL	57
2.6.7	Fabrication tolerances and proposed design	57
2.7	Ring resonators: Main parameters	60
2.8	Sensor architecture	64
2.8.1	Sensing strategies	64
2.8.2	Proposed structure and detection principle	64
2.8.3	Ring resonator absorption architecture	66
2.8.4	Analysis of the optical path enhancement	68
2.8.5	Optimization of the ring length	70
2.8.6	Detection limit	71
2.8.7	Validity of the model	71
2.8.8	Conclusion	73
3	Fabrication and characterization results	75
3.1	Nanostructure fabrication and characterization	75
3.2	Polymer patterning and characterization tools	76
3.2.1	Layout generation of the master stamp	76
3.2.2	EBL exposure	77
3.2.3	Master stamp results	78
3.2.4	Intermediate soft stamp	79
3.2.5	Cladding layer	80
3.2.6	Nanoimprint	80
3.2.7	Samples	82
3.3	Characterization of thin waveguide polymer films	83
3.3.1	General ellipsometry of thin films	83
3.3.2	Ellipsometry of the multilayer stack: TOC of the Si substrate	85
3.3.3	Thermo optic coefficient of thin polymer films	86
3.3.4	Incertitude associated to the refractive index variation	89
3.3.5	Final observations on the polymer film	90
3.3.6	Effective index measurement with a prism coupler	91

3.3.7	Conclusions about the characterization	93
3.4	Optical characterization of imprinted devices	94
3.5	Set-up requirements for integrated structure interrogation in the visible range	94
3.5.1	LED	95
3.5.2	Solid Lasers	96
Laser Diode	96
DPSSL	96
VCSEL	96
3.5.3	Supercontinuum	96
3.5.4	Other sources	97
3.6	Experimental set up: Grating-waveguide-photodiode	97
3.7	Characterization of ring resonator at fixed wavelength	101
3.7.1	Thermal resonance tuning of ring resonators	102
3.7.2	Effects of temperature on the set-up	104
3.7.3	Thermo-optic response of polymer grating coupler	105
3.7.4	Thermo-optic characterization of ring resonators	109
3.8	Conclusions about optical measurements	111
Conclusions and further viewpoints		113
Conclusion	113
Perspectives	114
Design	114
Fabrication	115
Characterization	115
A	EBL parameters	117

List of Figures

1.1	Sketch of the integration of microfluidics and optical chips inside a commercial package. The optical chips consist in a polymer ring resonator with a grating to perform the on-chip light coupling.	10
1.2	Sketch of the integration of microfluidics and optical chips inside a specific package. The optical chips consist in a polymer ring resonator with two gratings to perform the on-chip and out-chip light coupling.	10
1.3	Sketch of a structure including an on-chip coupling solution, a waveguide, and a ring resonator. The devices are patterned in the polymer on CYTOP to provide water-like cladding.	17
2.1	Description of the soft-NIL process. (a) First, the soft stamp is replicated from the master stamp in a soft polymer material. (b) Then, the polymer optical devices can be replicated from the soft stamp with an optimized polymer cross-linking. (c) The soft stamp is released	23
2.2	Conformal contact with soft nanoimprint lithography	25
2.3	(a) Layout example with the patterned area (green) in PMMA. The middle strip will remain on the resist after development (b) SEM image of the patterned design at 20 KeV. (c) SEM image of the patterned design at 30 KeV	26
2.4	Montecarlo simulation showing the different electron trajectories at 5 KeV on 400 nm of PMMA thickness (left) and on 40 nm of PMMA thickness (right). The Si wafer is considered infinite	27
2.5	Montecarlo simulation showing the different electron trajectories at 30 KeV on 400 nm of PMMA thickness (left) and on 40 nm of PMMA thickness (right).	27
2.6	EBL process flow with one etching process with negative resist (a) A thin layer of negative resist is exposed (green) with the electron beam. (b) The isolated resist remains, the unexposed resist is diluted in the solvent. (c) The device is etched, the remaining resist protects the waveguide region. (d) The remaining resist is removed thus the pattern is transferred to the master stamp	29

2.7	EBL process flow to pattern with positive resist. (a) A thin layer of positive resist is exposed (green) with the electron beam. (b) The isolated resist with broken polymer chains is removed by the solvent, the unexposed resist remains on the wafer. (c) The device is etched, the remaining resist protects the trenches for the waveguide region. (d) The remaining resist is removed thus the pattern is transferred to the master stamp	29
2.8	Transversal cross section showing the master stamp fabrication in two steps with two level height (for both grating and waveguide). (a) Resist coating of the wafer. (b) Fully exposure of the shallower features (grating). (c) We etch the exposed features to attain the desired height, the remaining resist is removed. (d) The wafer with the grating is re-coated with resist. (e) The deeper trenches (Waveguide) are developed and etched. (f) The rest of resist is removed	30
2.9	Transversal cross section showing the master stamp fabrication in a single step with the grating and waveguide features (a) Resist coating with the optimized thickness to completely etch the trenches defining the waveguide height. (b) Exposure at different doses of both waveguide (higher) and grating (lower). (c) Same resist development time provides different resist height profiles. (d) Two different heights are attained on Si after RIE. (e) Resist removal	31
2.10	Description of the nanoimprint process for waveguide replication. The polymer optical device can be replicated from the stamp. The stamp is held in contact during the cross-linking process of the polymer. Finally, when the stamp is released a thin slab residual layer remains which will affect optical performances.	33
2.11	Conformal contact with soft nanoimprint lithography	36
2.12	Defectivity associated to PDMS based materials and COP/COC materials	38
2.13	Comparison between different polymer flow regimes. (a) Polymer must flow over large distances to fulfill the nanostructures of the stamp. (b) The filling of a microcavity also needs to displace polymer over large distances. (c) By the introduction of several sink structures or indenter the polymer flow is enhanced.	40
2.14	Process flow comparison between the use of a non-optimized stamp and a stamp designed considering the MPSM	41
2.15	Summary of the final choices for the fabrication process.	42

2.16 Complete overview of the desired process flow (a) Master stamp fabrication: Two height patterning of the master stamp with the same polarity as the final aimed device in polymer. (b) Intermediate soft stamp fabrication with the hot embossing of TOPAS. (c) Utilization of the intermediate soft stamp to replicate structures in polymer. All sketches are accompanied of the cross-sectional front view showing the trenches around the structures optimizing the squeeze of the polymer (MPSM).	43
2.17 Overview of the waveguide cross-section in the MODE solver. Based on FDE calculations ($\lambda = 507$ nm) we are able to show the mode profile of the waveguide a) In this example: Waveguide width $W_w=450$ nm, $W_h=350$ nm, RL=50 nm, cladding layer (CYTOP $n = 1.34$) and PML as boundary condition. b) Resulting mode profile for air ($n = 1$) as background material ($n_{eff}=1.383$, $\Gamma=0.8$) c) Resulting mode profile with water ($n = 1.34$) background. ($n_{eff}=1.416$, $\Gamma=0.72$).	45
2.18 Different effective index calculated analytically for the proposed waveguide geometries.	46
2.19 Geometrical variation of the waveguide parameters W_w , W_h and RL, The curve indicates the boundary conditions for single-mode propagation depending all the geometrical parameters.	47
2.20 Effective index waveguide variations depending on the thickness of the RL. Simulations have been performed with LUMERICAL©MODE SOLVER package. The inset shows how the TE mode profile spreads out into a 150 nm thick RL compared to the mode profile without any RL.	48
2.21 Wavelength dependence of the effective indices of rib-like waveguides 350 nm x 350 nm onto a minimal RL of 50 nm. Water and air cladding are set up as top cladding.	49
2.22 Periodic structure	50
2.23 (a) Grating interface showing both transmitted and reflected waves of order q with an incident angle.	51
2.24 Plot of the effective index versus grating period ($q=-1$, $\theta_{in}=-20^\circ$, $\lambda = 507$ nm. For the stack of materials presented here (NILUV/CYTOP/Si).	52
2.25 Plot of the effective index versus the input angle. Allowed and forbidden regions are plot depending the effective index.	53
2.26 a) Color-map of the proposed grating coupler ($\Lambda = 290nm$) profile during diffraction. The inset shows the propagation direction of the guided wave b) Calculated diffraction angle with the FDTD solver showing a peak at -19°	54

2.27	Etch depth optimization. The figure shows the reflected power backwards and the optimal etch depth for the proposed grating coupler ($\Delta = 290nm, \lambda = 507 nm$). The inset shows a capture of the LUMERICAL software to calculate the transmitted and reflected power.	55
2.28	The angle of diffraction slightly changes when the etch depth is modified. The detuning is extracted from the simulation and it is around $0.0225^\circ / nm$	56
2.29	The angle of diffraction slightly changes when the duty cycle is modified. The detuning is extracted from the simulation and it is around 2.2° when the duty cycle changes form 0.1 to 0.9. Therefore the detuning is $2.75^\circ / \Delta DC$ The inset shows the different duty cycle displayed in the software b) The optimum duty cycle is found around DC=0.5.	57
2.30	The diffraction angle of a 350 nm height waveguide slightly changes when the RL is modified. The detuning is extracted from the simulation and it is around $0.02^\circ / nm$ when the RL increases from 0nm to 100nm. The inset shows transversal cross-section of a grating with a period of $\Delta = 290 nm$	58
2.31	a) Design of the tapered waveguide and the grating coupler. b) Cross-section view of the 3D structure showing the height of the waveguide layer $h=400nm$ corresponding to the waveguide height (350nm) with 50nm of RL. The grating depth (h_g) is set to 150nm.	59
2.32	ALL-pass (Notch filter) ring resonator.	60
2.33	All-pass (Notch filter) ring resonator transmission showing different coupling configurations with $a = 0.65$	61
2.34	Transmission of 350x350nm ring resonator waveguide for two different polymers with $R=15\mu m$. The RL is modified affecting the transmission of the ring. The quality factor $Q \approx 1700$	62
2.35	(a) Sketch of the ring resonator with a water cladding. The absorption of both the waveguide core and bottom cladding are constant and very dependent on the fabrication process.(b) Mode profile of the 350nm x 350nm polymer waveguide ($n=1.56$) with a confinement factor $\Delta = 0.65$. The absorption of the cladding depends on the top reagent extinction coefficient n_i	65
2.36	Transmission spectrum of an all-pass ring resonator for different complex refractive index variations. The increase of the complex refractive index ($n_i = 10^{-4}$ to 10^{-3}) can increase the transmitted power at resonance (decreasing the ON-OFF ratio.)	65

2.37	Enhancement of the single round trip sensitivity ($S(r = 0) = \frac{4\pi}{\lambda} L\Gamma$). Clearly, high quality devices provide best enhancement factor. The role of the autocoupling indicates that the best enhancement is obtained for slightly overcoupled/undercoupled rings. The operation point given par <i>Nitkowsky et al.</i> is indicated at $r = 0.9812$ and $a = 0.965$	68
2.38	Sensitivity curve for a resonator with intrinsic losses $a = 0.96$ ($n_{i0} \approx 5.8 \cdot 10^{-6}$). For small variations $n_{i0} \gg \Delta n_i$ the sensitivity curve will be stable around a fixed operation point. For large variations the behavior of the resonator is greatly affected	69
2.39	Sensitivity is represented with the colorbar versus the ring radius and the autocoupling factor r for two different propagation losses (a) 10 cm^{-1} , (b) 1 cm^{-1} . The dash line represents the critical coupling separating the undercoupling and overcoupling regimes.	70
2.40	(a) When $r = 1$ no power is coupled into the ring. When the gap is too small ($r \sim 0$) ($<70\text{nm}$), the power coupled into the ring resonator comes back to the bus waveguide. Simulations were done at $\lambda=532\text{nm}$. (b) Comparison between the proposed equation and the results from the 2.5 FDTD simulations ($\Gamma = 0.25$, $R=17.5 \mu\text{m}$ and $R=15 \mu\text{m}$)	72
3.1	Layout design of the structure for the master stamp. (a) Long waveguide (6mm) with/without ring resonators and grating couplers . (b) Close view of the trenches defining the ring resonator ($R = 15\mu\text{m}$). (c) Waveguides with/without ring resonator and a single grating coupler. (d) Linewidth/dose test to study the optimal grating coupler recipe	76
3.2	SEM images of the two height master stamp. (a) A cross-sectional view of two heights (150/300 nm). (b) A grating groove with a period of 400 nm of and 150 nm of etch depth. (c) Overview of a ring resonator of the master stamp. (d) Close image of the ring gap.	78
3.3	SEM image of the soft-imprint stamp. a) Grating coupler transferred to the COC(TOPAS) showing the trenches used to enhance the polymer flow (MPSM). (b) SEM image of the gap of the ring resonator. We can appreciate shrinking marks (red sports) around the gap, ring, and waveguide.	79
3.4	(a) SEM image of the transversal cross-section of a cleaved waveguide. (b) 350 nm^2 cross-section polymer waveguide with 50 nm of RL. This layer thickness is measured combining optical ellipsometry and a mechanical profilometer.	81

3.5	Comparison between the grating profile of the SOI master mold (red) and the final device (black) obtained with an intermediated COC8007 soft stamp. The final device is made in NILUV-394 deposited atop the CYTOP cladding on a silicon substrate. The inset shows a SEM picture of the fabricated grating ($\Delta = 289$ nm).	81
3.6	Table with the devices addressed in this work.	82
3.7	The change in polarization is measured with an ellipsometer. An incident plane wave with an angle Φ with a fixed polarization (p,s) is reflected from the surface. The reflected elliptical spot is analyzed. The ellipsometer measures the shift in Δ and Ψ	84
3.8	Stack of materials studied by a phase modulated ellipsometer.	85
3.9	Calculated I_c (Bluish) and I_s (Reddish) values for different input conditions, the model fit perfectly the obtained values. The curves are shown for two different wafer temperature 25°C and 85°C . Cyan and magenta are measured at 70° AOI with surrounding air. Blue and red curves correspond to two measurements at 70° AOI with a surrounding atmosphere of N_2	88
3.10	Refractive index dispersion for the UVNIL thin film obtained with the ellipsometry model (left). Direct measurement of the refractive index dispersion for the bulk of UVNIL. The similar dispersion trend obtained between the model and the bulk validates our model.	89
3.11	We show the thickness versus temperature for the UVNIL394 resist. The curves were taken in a row of 5 days. The thickness shows a mechanical hysteresis since the layer does not seem to recover the initial thickness	90
3.12	TOC versus CTE for different polymers used for waveguide applications. The curve is presented in [123]. We place the NIL UV regarding the behavior of the other polymers.	91
3.13	The set-up used to visualize the dark modes of the waveguide. The dark lines in the screen correspond to the guided modes into the waveguide.	92
3.14	The set-up used to measure the coupling angle of the guided modes of the waveguide. The device and the prism are rotated while a Si photodiode collects the reflected light.	92
3.15	Experimental set-up used for the optical characterization of the fabricated structures (taper, grating and waveguide). Input coupling is ensured through the grating and the output light is measured with a silicon photodiode.	95
3.16	Experimental set-up used for the optical characterization of the fabricated structures (taper, grating and waveguide). Input coupling is ensured through the grating and the output light is measured with a silicon photodiode.	98

3.17	Efficiency versus input angle for three different CYTOP claddings. Angular width is extracted at FWHM.	99
3.18	Simulation results of optical efficiency versus angular width for different CYTOP cladding thicknesses when considering only the grating (without waveguide). The input light corresponds to a focused Gaussian beam with $11 \mu m$ waist radius and 0.83 beam divergence. The center wavelength of the beam is 507 nm and the angular width at FWHM is 1.23°	100
3.19	The increase of device temperature implies a reduction of effective index proportional to T and the negative TOC of the polymer. The temperature variation from T_1 to T_2 allows us to modify the optical path between $neff(T_1)$ and $neff(T_2)$. In both points the ring is in resonance with the laser wavelength.	102
3.20	Thermal gradients create stress in the set-up and wafer which implies misalignment due to device expansion and wafer bending.	105
3.21	Efficiency versus input angle for three different temperatures. Measures where taken at $\lambda = 532nm$. The optimal input angle shift to the more negative angles (lower refractive index).	106
3.22	Draw of the angle-efficiency curve for different temperatures. If we consider the curve at $20^\circ C$ we can see how the efficiency will evolve for three different coupling angles.	107
3.23	Power variation versus temperature for different angle offset. The offset is applied to the optimum coupling angle at $T=20^\circ$. As the offset is higher the slope of the curve is larger.	108
3.24	Transmission spectrum of a Ormocore ring resonator a fixed wavelength. The temperature tuning allows for refractive index variations to observe the filtering operation of the all-pass ring resonator.	109
3.25	Transmission spectrum of a Ormocore ring resonator a fixed wavelength. The black curve fits the behavior of the ring resonator. The FRR found is 0.011 with an TOC close to $3.3 \cdot 10^{-4} K^{-1}$	110
	Sketch of the proposed set-up for the sensing experiments. The refractive index of the liquid is varied in-situ by means of the fluidic pumps and the mixer. The liquid is brought to the optical chip inside the microfluidic channel.	116
	Configuration of the EBL tool for the double exposure patterning	117

List of Tables

2.1	Thermomechanical properties of some soft stamp materials	36
2.2	Input data for waveguide and grating.	59
2.3	The table shows the gap for each value with the associated r factor. The transmitted power values for each r at the output of the water cladding resonator are compared to the output after adding an absorptive perturbation to the cladding ($n_i = 10^{-5}$).	72
3.1	Measured coupling angles with the prism coupling technique. The obtained effective index were calculated with the equation Eq.3.13 and compared with the values obtained with LUMERICAL for the stack of materials.	93
3.2	Considerations on the visible input beam source for microring resonator applications.	97
3.3	Experimental values of angular width ($\Delta\theta$), coupling angle (θ_c) and efficiency (α) for samples versus different thicknesses of CYTOP. The coupling length is determined analytically.	99

List of Abbreviations

OMR	Optical Microring Resonator
RI	Refractive Index
AOI	Angle Of Incidence
RL	Residual Layer
PML	Perfectly Matched Layer
TOC	Thermo Optic Coefficient
CTE	Coefficient of Thermal Expansion
OCT	Optical Coherence Tomography
RIE	Refractive Ion Etching
EBL	Electron Beam Lithography
SMC	Single Mode Condition
MMC	Multi Mode Condition
DC	Duty Cycle
AFM	Atomic Force Microscope
SEM	Scanning Electron Microscope
TEC	Thermo Electric Cooler
SCCM	Standard Cubic Centimeters per Minute

For/Dedicated to/To my...

Introduction générale

La qualité et la disponibilité de l'eau représentent un problème environnemental majeur ayant des répercussions très importantes au niveau sociétale et économique. Dans ce contexte, cette problématique est considérée comme un défi majeur du programme de l'Union Européenne H2020, d'une part pour 2016-2017, dans le cadre du défi sociétal 21, d'autre part, dans le programme de travail pour 2018-2020 avec l'appel « Water for our environment, economy and society ». Ces efforts font suite à un nombre croissant d'études qui ont établi le lien entre l'empoisonnement aux ions lourds et des maladies auto-immunes, notamment l'autisme ou les troubles du comportement. De plus, les ions lourds peuvent avoir des effets délétères sur la santé humaine, même à des niveaux d'ultra-traces ($\mu\text{g}/\text{L}$). Afin de neutraliser ces effets négatifs, la détection et l'élimination des polluants trouvés dans l'eau est actuellement un sujet hautement pertinent notamment dans le cadre de la recherche sur les biocapteurs [1].

La présence de ces éléments dangereux est complexe à traiter car ils sont largement utilisés dans l'industrie et l'agriculture, par exemple dans les revêtements de véhicules ou les pesticides. En outre, le suivi et contrôle des polluants dans l'eau n'est pas harmonisé entre les différents pays. De plus, les pays en voie de développement sont plus susceptibles de souffrir de problèmes de santé causés par une exposition directe ou indirecte via une pollution des ressources en eau. La surveillance de ces polluants est complexe et repose actuellement sur des équipements de laboratoire coûteux qui ne sont pas encore déployables sur le terrain. Plusieurs techniques spectrométriques sont utilisées pour mesurer la concentration de ces polluants. Parmi elles, la plus courante est la détection par spectrométrie d'absorption UV-VIS [2], fondée sur l'analyse spectrale visible des eaux polluées avec des ligands de la classe diarylthiocarbazone. Ces types de ligands sont d'intérêt particulier en raison du fait qu'ils produisent des complexes colorés avec les métaux lourds toxiques dilués dans l'eau [3]. Parmi les ions de métaux lourds les plus courants, le Chrome hexavalent est l'un des plus toxiques que l'on trouve dans l'eau. Sa complexation avec le ligand 1,5 diphénylcarbazide (Cr(VI)-DPC), présente un pic d'absorption dans le vert du spectre visible de la lumière ($\lambda=532$ nm); ainsi, la concentration de cet ion toxique peut être déterminée en mesurant le spectre d'absorption à la longueur d'onde sélectionnée.

Pour répondre au problème socio-environnemental, l'industrie des capteurs optiques bio / chimiques doit fournir une solution permettant de surveiller la présence des dits polluants de l'eau directement sur place [4]. De nos jours, les guides d'ondes optiques constituent une solution intéressante permettant de créer un ensemble complet de fonctionnalités intégrées sur puce, telles que la génération et détection de lumière et la transduction. Cependant, travailler avec des guides d'ondes optiques dans le domaine visible est moins fréquent qu'une utilisation plus standard dans le domaine des télécommunications ($\lambda=1550$ nm). La raison principale réside dans

la difficulté à réaliser des structures critiques dont le motif est inférieur à la longueur d'onde. Parmi les dispositifs optiques intégrés les plus courants, les micro-résonateurs optiques en anneau (Optical Microring Resonator : OMR) sont largement utilisés, en tant que filtres spectraux, interrupteurs ou convertisseurs de fréquence dans les circuits pour les communications optiques, mais aussi comme transducteur optique dans le domaine des capteurs.

Ce travail est axé sur la recherche et le développement d'OMR afin de répondre aux problèmes socio-économiques susmentionnés. Nous abordons les nouveaux protocoles de fabrication d'OMR compatibles avec les technologies à très bas coût telles que la lithographie par nano-impression. Les résultats présentés dans cette thèse invitent à une utilisation ultérieure de ces dispositifs dans des systèmes complets en utilisant les réalisations tant dans la chimie des couleurs et microfluidique numériques obtenus dans des travaux antérieurs. La principale innovation du procédé de fabrication repose sur la structuration directe de guides d'onde et les coupleurs de réseau pour le fonctionnement de la lumière visible, qui sont utilisés pour coupler la lumière provenant de nanoguides photoniques à résonateurs en anneau. Les structures sont conçues sur un polymère peu coûteux à indice élevé, qui, en complément du processus de fabrication, fournit des ensembles complets de dispositifs optiques intégrés.

Quatre partenaires de recherche et industriels sont impliqués dans ce travail. Les moyens de fabrication sont fournis par le LAAS à Toulouse (Laboratoire d'architecture et assemblage des systèmes). Tous les processus de fabrication y sont effectués, notamment les micro et nano-motifs des structures proposées ainsi que les installations d'impression 3D destinées à supporter les puces optiques. Le travail au laboratoire IMS (Laboratoire de l'Intégration du Matériau au Système) porte sur la simulation et la conception et la caractérisation optique des structures, mais également sur le développement d'un banc d'essai interne permettant d'étudier les performances des nanostructures. Le LOMA (Laboratoire Ondes et Matières d'Aquitaine) apporte son savoir-faire en matière de caractérisation des films polymères minces avec un banc d'ellipsométrie. Les laboratoires comptent sur le soutien d'un partenaire industriel international, TECNALIA, basé à San Sebastian, qui cherche à intégrer et à valoriser le dispositif complet via un transfert industriel.

Le premier chapitre de cette thèse est consacré à expliquer plus en détail le contexte des objectifs généraux, l'état général de l'art en tenant compte des limites du contexte (visible, spectrophotométrie, optique intégrée polymère), les travaux antérieurs et leurs limites, enfin est proposé un aperçu détaillé du travail présenté dans le manuscrit. Des travaux ont été réalisés dans le cadre du développement global de puces intégrées pour la détection des polluants de l'eau. Les dispositifs microfluidiques permettent la manipulation d'analytes et de réactifs, avec le contrôle numérique de la création, du déplacement ou du mélange de gouttes, tel un laboratoire sur puce. La détection homogène et l'utilisation de réactifs colorimétrique ont déjà fait l'objet de tests expérimentaux avec les OMR pour des applications autres

que la surveillance des polluants de l'eau. Issu de ces avancées majeures, l'objectif de ce travail est double. D'une part, il s'agit de mettre au point un processus fiable de fabrication de nanostructures en polymères pour le guidage d'ondes de lumière visible. Ce processus doit être compatible avec des techniques rapides et bas coût lesquelles permettront la commercialisation et l'usage industriel des nanostructures polymères. Le principal enjeu est d'obtenir des dimensions sous-longueur d'onde pour fonctionner dans la région verte du spectre visible. D'autre part, nous devons proposer un cadre théorique pour analyser la sensibilité des OMR et leurs performances en tant que spectromètres VIS, et comparer les résultats à ceux de la littérature. Cette thèse comprend trois chapitres principaux. Le chapitre 2 présente l'ensemble du contexte en matière de fabrication, de conception et de théorie. Nous présentons la technique de la lithographie à empreinte douce. Les principaux outils de la nanolithographie par faisceau d'électrons et de la lithographie par nanoimpression sont passés en revue. Nous présentons ensuite la conception des structures et leur adaptation pour les rendre compatibles avec le processus de fabrication présenté précédemment. La conception s'appuie sur des outils mettant en œuvre la méthode des différences finies (FD : Finite Difference) et des simulations s'appuyant sur le calcul de différences finies dans le domaine temporel (3D-FDTD : Finite Difference Time Domain). Dans la troisième partie du chapitre, nous proposons une approche analytique et des règles de sélection des paramètres du résonateur en anneau, pour l'étude de ses performances en tant que microspectromètre visible. La sensibilité, définie comme le rapport de la variation de puissance à la résonance sur la variation complexe de l'indice de réfraction, est discutée en fonction des paramètres de l'anneau. La configuration de couplage optimale est analysée en combinant la transmission du résonateur en anneau non perturbé et du résonateur en anneau en présence d'un milieu avec pertes (considéré comme une « gaine » avec pertes). Le rôle du champ évanescent, de la longueur optique et du mécanisme de couplage est discuté. Les simulations FDTD (2.5D) de résonateurs en anneau sont présentées pour différentes géométries afin de comparer les résultats avec les valeurs obtenues de manière analytique.

Le chapitre 3 est consacré aux réalisations expérimentales, visant à démontrer la faisabilité des coupleurs de réseau et des guides d'ondes en polymère fabriqués sur une gaine de CYTOP pour les applications en longueur d'onde visible. La première partie décrit l'ensemble du processus qui traite de la mise au point du processus de fabrication par impression, tandis que la deuxième partie présente la caractérisation des dispositifs et analyse l'impact des tolérances de fabrication sur le rendement optique. Les dispositifs sont imprimés à partir d'un tampon souple, différents matériaux de tampons, notamment des thermoplastiques et des mélanges durcis de PDMS, sont utilisés et comparés. Le tampon principal consiste en une structure SOI (Silicon-On-Insulator) à plusieurs niveaux, comprenant à la fois des guides d'onde submicroniques coniques (350 nm x 350 nm) et des coupleurs à réseau (d'un pas égal à 290 nm). Il permet un processus d'impression directe de la structure multi-hauteur

en une seule étape avec une couche résiduelle minimale (RL) car son épaisseur peut dégrader les performances optiques de la structure globale. L'efficacité de couplage optique mesurée en fonction de l'angle d'entrée est également présentée pour différentes épaisseurs de CYTOP. En utilisant cette technique de configuration directe, nous démontrons une efficacité de pointe et une grande largeur d'acceptation angulaire permettant un alignement aisé de la source, ce qui pourrait faciliter le processus de conditionnement de futures puces microfluidiques destinées à des applications de détection en optique intégrée. Enfin, nous concluons ce travail et argumente des points de perspective. Notamment, la caractérisation avec des sources laser à large bande est fortement recommandée pour caractériser le spectre de transmission du résonateur en anneau dans une phase d'étude. De manière complémentaire, nous proposons de caractériser les résonateurs en anneau à l'aide de différents mélanges de liquides à indices de réfraction distincts, qui permettront une modification in situ de l'indice de la gaine supérieure. Cette combinaison permettra de valider le fonctionnement du dispositif avec des sensibilités expérimentales quantitatives, avant d'envisager une intégration d'une architecture plus complète du capteur optique et de la microfluidique associée.

General introduction

Water quality and availability is a major socio-environmental issue with high social and economic importance. Recently, an increasing number of studies have established the link between heavy ions poisoning and diseases such as autoimmune diseases, autism and behavioral disorders. Moreover, heavy ions can have deleterious effects on human health even at ultra-trace levels. In order to neutralize these negative effects, the detection and removal of heavy ions found in water is currently a topic of main relevance for the biosensor research[1]. The presence of these hazardous elements is complex to address because they are present in vehicle coatings and pesticides widely used industry . Moreover, the tracking of water pollutants is not equally controlled between the different countries, being developing countries more susceptible from suffering health concerns. Monitoring these pollutants is very challenging and currently relies on expensive equipment that is not field-deployable yet. Several spectrometric based techniques are used to measure the concentration of these ions. Among these techniques the most common is tracking with UV-VIS absorption spectrometry [2]. This technique is based on the visible spectral analysis of polluted water with diarylthiocarbazon ligands. These type of ligands are of particular interest due to the fact that they produce colored complexes with the toxic heavy metals diluted in water[3]. Between the most common heavy metal ions, hexavalent Chromium is one of the most toxic found in public water. The complexation of Hexavalent chromium with the ligand 1,5 diphenylcarbazide: Cr(VI)-DPC, presents an absorption peak in the visible green region of the light spectrum ($\lambda = 532 \text{ nm}$); thus the concentration of this toxic ion can be determined by measuring the absorption spectra at the selected wavelength.

To answer this socio-environmental issue the optical bio/chemical sensor industry must provide a solution to track the presence of the mentioned water pollutants in-situ. [4]. Nowadays, optical waveguides are a comprehensive solution to build full sets of on-chip integrated functionalities such as light generation, light detection and sensing. However, working with optical waveguides in the visible range is less common than the standard utilization in the telecommunication range ($\lambda = 1550 \text{ nm}$). The primary reason is the critical dimensions required if sub-wavelength sized structures are needed. Between the most common optical integrated building blocks, optical micro-ring resonators (OMR) have been widely employed, as wavelength filters, switches and frequency converters in optical communication circuits, but also as a transducer for in-situ pollutant measurements.

This work focus on the research and development of OMR to answer the socio-economical issues stated above. We address new fabrication protocols of OMR compatible with ultra-low-cost technologies such a nanoimprint lithography. The results shown in this thesis invite to further utilization of these devices into complete systems regarding the advances in both color chemistry and digital microfluidics achieved in previous works. The main innovation of the fabrication process relies

in the direct patterning of waveguides and grating couplers for visible light operation, which are used to couple the light from photonic nanowaveguides to ring resonators. The structures are patterned with inexpensive high index polymer, which in complement to the fabrication process provide full sets of integrated optical devices.

Four research and industrial partners are involved for the presented purpose. The fabrication facilities are provided by the LAAS (Laboratoire d'architecture et assemblage des systemes). All the fabrication process are done there, notably the micro and nano-patterning of the proposed structures as well as the 3D printing facilities to support the optical chips. The IMS lab (Le laboratoire de l'Intégration du Matériau au Système) addresses the simulation and design and optical characterization of the structures. The IMS also develops an in-house characterization bench to study the performance of the devices. In addition, the LOMA (Laboratoire Ondes et Matière d'Aquitaine) provides know-how about the characterization of thin polymer films. The laboratories have the support of an industrial international partner TECNALIA which looks for the integration and translation of this kind of components into usable consumer products.

The first chapter of this thesis is devoted to explain in more detail the context with the overall objectives, the general state-of-the-art considering the context boundaries (visible/spectrophotometry/integrated optics/polymer), the limitations of previous work and a detailed overview of the work presented in the manuscript. The Chapter 2 reviews the basis of modeling, materials and fabrication needed to accomplish this work. Then, the experimental results related to the device fabrication and the characterizations, including the experimental set-up are described in the Chapter 3. Finally, we detail the conclusions and perspectives.

Chapter 1

Optical structures for visible light wave guiding

In this chapter, we look into the main parts of an optical device intended for in-situ sensing of liquids. After discussing each part, we state the main objectives of this thesis which focus on the fabrication and the study of the optical transducer. Complementary parts of the transducer are currently being studied in parallel, and they are only over viewed in this thesis. Then, we detail a state of the art based on the integrated technologies for visible light operation. First, we introduce the primary interest in visible photonics, to subsequently explore the studies concerning visible absorption based sensors. We review the main fabrication platforms used for visible operation, among them, we propose polymers as a suitable choice which fulfills the requirements of the final device. Main issues regarding the nanostructuring of polymers are also discussed. The chapter ends analyzing in detail the previous research supporting the academic interest of this work as well as the proposed structure of the manuscript.

1.1 Overview

Optical microring resonators have been used as an optical transducer for sensing biochemical elements. They present some unique advantages concerning other technological platforms directly based on the optical path. For example, in ring resonators, the interaction length does not correspond to the physical length of the device. Consequently, light propagates into the resonant cavity resulting in an overall device path length proportional to the quality factor [5]. The small footprint of these devices (usually less than $500 \mu\text{m}^2$) makes it a suitable choice to analyze small quantities of liquids compared with technologies based on the single-pass optical path iteration, such as plasmonic or optofluidics based devices. Moreover, as a planar technology, it provides easier integration and feasibility than 3D nanostructures such as micro-spheres or micro-toroids [6]. Nonetheless, very recent research have shown the direct patterning of sol-gel 3D structures [7] providing high quality factors ($Q = 3 \cdot 10^6$).

We can cite three very well-know main advantages of the OMR based devices. If we take a look to their general assets as integrated sensors :

- The functionalization of the waveguide surface allowing the enhancement of the selectivity and to detect a specific interaction between an analyte and a dedicated ligand.
- The fabrication of optical waveguide devices which are compatible with state-of-the-art micro and nanofabrication facilities.
- The integration within other micro and macro systems dedicated to sensing functionalities (e.g., electronics, microfluidic chips) making hybrid opto-fluid lab-on-chips

These advantages are well-known in research and industry. However, most of the sensors based on optical nanostructures remain “lab-demonstrators” that ultimately have little chance to be deployed at a large scale for specific applications and environments. Although ultra-integrated structures reduce the price of chip-per-wafer, these nm-sized objects as marketable products are still pricey for deployable solutions, which would be of main interest in point-of-care and in-situ environmental sensing. Deployable and portable integrated optical sensor reveals major counterparts regarding the three main advantages cited before:

- The functionalization of the surface requires a costly chemical process which only stands in lab conditions.
- The fabrication process should be compatible with low-cost materials and mass production tools. Are really III-V materials and silicon photonics based devices ready to be disposable products?
- The microfluidics set-ups usually require expert handling and very bulking elements such as pumps, power supplies, and complex standardization protocols. Is it a lab-on-chip or a chip-on-lab?

Surface engineering, nanofabrication, and microfluidics converge at this point, but revealing essential issues. The functionalization of the surface for surface sensing is considered a label-free technique which provides more substantial sensitivity results [8] [9] than homogeneous sensing ($\sim 115\text{RIU}$ [10] [11]). We must cite the complexity to compare both methods because neither the analyte nor the devices is the same. The main reason of the improved performance is that during surface sensing the molecules are bound to the surface while in homogeneous sensing they are distributed into the cladding, being the detection limited to the tail of the evanescent field. Most devices, integrated or not, focus on both label sensing and label-free sensing with functionalized surfaces. Portable and deployable devices would benefit from at least commercial-like performances based on homogeneous sensing which fits in a small single package. So, the challenge remains to achieve very integrated devices providing both state-of-the-art performances and portability being

compatible with a low-cost process. Moreover, the optical path length must be large enough to efficiently interact with the adjacent medium, which in turn, contributes to enhance the sensitivity. Regarding the signal analysis, optical spectrum analyzers and high resolution spectrometers are usually required. These tools present high instrumentation costs which are a limiting factor toward the development of portable photonic-based diagnostic systems. Even if the development of miniaturized, low-cost spectrometers is an active area of research, an alternative approach taken here is to design a sensor and sensing system that no longer requires spectrum analyzers, but rather a direct measurement of optical power with inexpensive photodiodes.

For the transducer fabrication platform, optical waveguides are now widely used components for light manipulation, independently of the final application. Extensive research has been carried out for infrared and near-infrared applications mainly addressing silicon photonics for high-speed data communications but also increasingly for sensing purposes. Particularly, semiconductor materials as Silicon-on-insulator (SOI) and III-V materials are widely accepted as mature and efficient technologies for photonics. Compared to these inorganic materials, optical polymers bring some substantial benefits such as low cost and ease of processing to meet a broad range of application-specific requirements. Moreover, their suitability to low-temperature and wet-coating processes over large areas for almost all sorts of substrates are recognized as critical requirements for mass production. Polymer waveguides are also highly transparent, with typical absorption losses of 0.1dB/cm or less at all fundamental communication wavelengths. However, the low refractive index contrast between core and cladding limits the light confinement and consequently limits the miniaturization of integrated polymer devices [12]. Finally, polymer materials can be nano-structured with low-cost fabrication processes such as photolithography and nanoimprint lithography.

The third part cited above concerns the integration of the microfluidic handling with the optical chip. The primary function is to bring the analyte in contact with the optical transducer. Microfluidic chips are commercially available; however, we need for extremely bulk pumps compared to the size of the circuit. Besides, microfluidic chips are made of elastomers or thermoplastics and the manipulation of these chips usually requires expert handling which is not suitable for mass production. Electrowetting on dielectric EWOD-based microfluidic chips are intended to overcome this issue by pumping and handling small quantities of liquids by electric pulses.

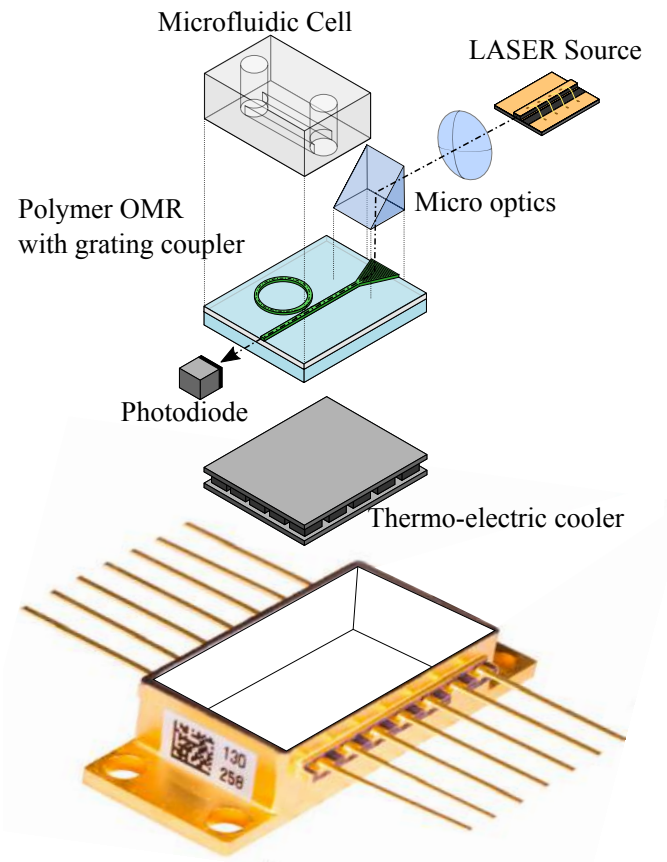


Figure 1.1: Sketch of the integration of microfluidics and optical chips inside a commercial package. The optical chips consist in a polymer ring resonator with a grating to perform the on-chip light coupling.

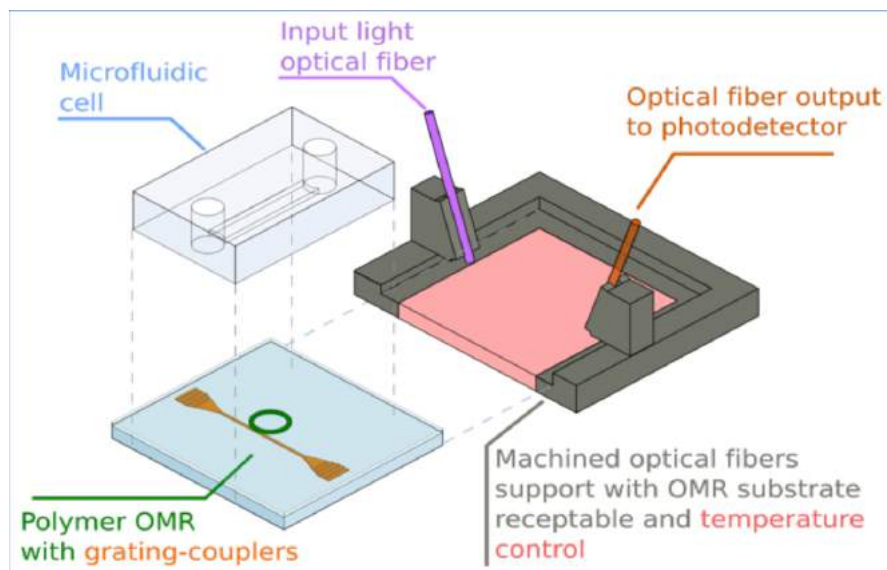


Figure 1.2: Sketch of the integration of microfluidics and optical chips inside a specific package. The optical chips consist in a polymer ring resonator with two gratings to perform the on-chip and out-chip light coupling.

Among our research partnership we converge towards the integration of the cited parts. The proposed elements can be assembled in a packaged device integrating all the functionalities as shown in Fig.1.1. We detail an example of a microfluidic cell with an optical chip inside a commercial butterfly-type package. The optical chip consists of an OMR to act as an optical transducer, in the same waveguide plane we can also include a grating structure to perform the on-chip light coupling. Alternative coupling structures like wedges or optical glues can be used. Further efforts can be addressed to improve the optical alignment and integration. As a second example, the Fig.1.2 shows a packaged chip where the on-chip and off-chip coupling is performed with grating couplers and micro-machined supports to hold the optical fibers. State-of-the-art 3D printing facilities allow for the low-cost plastic production of this kind of packages. Preferably, the sensing strategy must avoid further chemical or surface treatments of the optical transducer. The system must provide a position-tolerant on-chip coupling solution and a microfluidic circuitry as found in lab-on-chips. An optical transducer based on OMR must be present, this transducer must be also compatible with a low cost process which certainly involves an unexpensive platform such as polymer materials. The work presented in this thesis focus on the parts concerning the optical transducer, the optical coupling and the sensing strategy.

Prior to field-monitored measurements with an hybrid fluidic-nanophotonic device we must balance the performance, the processing cost and device complexity. In this thesis we address our efforts to study a fast and low-cost fabrication process of polymer nanostructures integrating an optical transducer, optical waveguides and a on-chip coupling solution based on grating coupler. Since the device is intended for bio-sensing in liquid media without functionalization, we propose a new sensing strategy based on the utilization of the OMR as microspectrometer with an innovative combination of labeled and homogeneous sensing. Also, we provide a theoretical insight to enhance the resonator performance. The main interest is to provide enough sensor performance with the most straightforward design and fabrication process to reduce the number of variables that negatively impact the final device.

1.2 State of the art

Within this section, we show the interest of the main applications and perspectives of integrated photonics in the visible range. Between these applications, we focus our attention on the use of integrated optical microring resonators as visible spectrometers for biosensing. The primary technological platforms to develop integrated optical elements at a visible wavelength is reviewed. Among these platforms, polymers provide similar integration possibilities than typical inorganic platforms. Finally, we focus our attention on the main issues affecting the nanostructuring of polymers for waveguide applications.

1.2.1 Why visible photonics?

There is a large room for the development of integrated photonic devices operating at visible wavelengths. Up to now, integrated photonics working in the visible range has captured less attention than infrared or near infrared photonics. This is mostly due to the high industrial maturity of the semiconductor microfabrication technology but also to the high absorption losses of these materials in the visible spectrum. However, visible integrated photonics based on alternative platforms such as polymer materials is being increasingly recognized as very promising in various applications, as bio/chemical sensing, on-chip spectroscopy, visible light communication, satellite laser ranging or on-chip quantum processing [13] [14]. Life sciences also benefit from visible wavelength based devices despite very long time-to-market product development [15]. One of the main applications of optics in medical sciences relies on Optical Coherence Tomography (OCT) [16] [17]. Most of OCT systems are based on Michelson interferometers to analyze different optical paths. Integrated optical waveguide Michelson interferometers have the potential to make OCT devices and components significantly smaller, more functional, and more cost efficient [18]. Although classically OCT focus on near IR, visible wavelengths have been used in the first non-integrated demonstrators of visible (520 nm to 630 nm) light optical coherence tomography (Vis-OCT), demonstrating accurate and robust measurement of retinal oxygen metabolic rate ($rMRO_2$) in rats [19]. The high transparency cornea, lens, and vitreous chamber allow cornea tomography due to their high transmission within the visible spectral range. Thus, medical diagnostics could benefit from integrated optical chips working in the visible region.

1.2.2 Integrated spectrometers based on colorimetric reaction

In addition to the mentioned applications, visible absorption spectrometry has been used for decades to determine the concentration of large amounts of components and reactions absorbing between 400 nm-780 nm (visible spectrum). Colorimetric reagents can be used in conjunction with optical devices such as optical fibers, to probe multiple analytes by measuring intrinsic absorption, or by incorporating sensing elements to enhance both selectivity and sensitivity [20]. Commercially available sensors based on optical fiber which rely on colorimetric absorption include CO_2 sensors in which a silica glass core is coated with a polymer cladding containing a colorimetric indicator. Upon exposure of any segment of the fiber, the CO_2 diffuses into the cladding and triggers a change in color [21] [22]. The same strategy can be used for sensing in aqueous media with the help of colorimetric reagents. However, one of the main drawbacks of colorimetric reactions is the toxicity of their solvents. The error during reagent manipulation and the need to use large volumes of dedicated reagents complicate the process for in-situ measurements. Integration trends combine the use of optical and microfluidic chips forming complete sets of optical

lab-on-chip to overcome these issues. For instance, direct absorption systems coupling LEDs and photodiodes with microfluidic channels are reported in [23], but the short optical absorption path limits the sensitivity [24]. A technique to increase the optical path based on random optical reflection inside metallic capillary tubes was reported in [25] [26]. Similarly, an optical link, based on a conventional Scotch tape waveguide operating at 632 nm was used for bulk homogeneous sensing [27]. Despite the low cost of the materials and process proposed here, the integration and repeatability of the sensing performances of these devices out of the lab environment have to be tested. Nowadays, it has been established that optical ring resonators coupled with microfluidic chips can become feasible integration solutions for in-situ absorption spectroscopy [28]. This type of opto-microfluidic assembly has been used for non-visible wavelengths performing the sensing of different types of glucose and oils are reported in [29] [30]. In addition, microring resonators can be manufactured in the main visible platforms such as Si_3N_4 and curable polymers leading to highly integrated low-cost devices [31].

Few studies have been published exploring the operation of microring resonators as micro-spectrometers. The cavity enhancement of light in a microring resonators enables to detect changes in its local environment. As a recent application example, colorimetric sensing for hexavalent Chromium Cr(VI) was published by Meziane et al. [32]. The chromate ions react with diphenylcarbazide (DPC) showing an absorption coefficient up to $\alpha = 0.2 \text{ cm}^{-1}$ (10^{-6} on the imaginary part of the refractive index) for concentrations nearby $200 \mu\text{g/L}$. Experimental measurements based on hollow-core metal-cladding optical waveguide sensor have shown variations in the extinction coefficient of the same magnitude order ($\Delta n_i = 10^{-6}$) [33]. Nitkowsky et al. [34] also demonstrated the absorption performance of a Si_3N_4 microring resonator experimentally as a biosensor by color-producing enzymatic reactions.

1.2.3 Integrated photonics platforms for visible wavelength operation

Fabrication of optical waveguide based devices such as grating couplers and ring resonators have been developed for visible wavelength operation in silicon nitride platforms (SiN), Triplex, TiO₂ and polymers. Excepting the polymers the other three platforms are CMOS compatible. Silicon nitride is presented as an alternative to the silicon photonic platforms due to the transparency of this material at visible wavelength [35]. Typical fabrication processes required for these platforms involve Low Pressure Chemical Vapor Deposition (LPCVD), patterning and refractive ion etching (RIE) and classical patterning methods such as optical lithography which able to achieve all kinds of optical microstructures [36] [37]. Other relevant platform is the Triplex platform is based on stacked layers of silicon nitride and silicon dioxide [38]. The sensing performance of OMR in the Triplex platform was already reported [39] showing similar performances to the silicon nitride based microring devices [40] [41]. Mainly, the light is coupled to the ring resonator through grating couplers or by butt-coupling from optical fibers. In the same way, the polymer can be also

structured and etched to fabricate ring resonator coupled to periodic structures [42]. Among the main advantages, polymer optical materials are also transparent in the visible spectrum and are compatible with fast and low-cost embossing methods [43]. Additionally, the relative wide range of low refractive index ranging from 1.33 to 1.7 is of great interest for MOEMS and sensing applications [44].

Different refractive index polymers are available depending on the application. Particularly, the use of low-index polymers as CYTOP ($n=1.339$ $\lambda = 580$ nm) enables enough core-cladding index contrast when paired with other high index polymer materials at visible wavelengths such as SU8 ($n = 1.57$), PMMA ($n = 1.5$) or Ormocore ($n = 1.56$). With CYTOP, symmetric waveguides can be designed with water-like refractive index top claddings. Potential applications of polymer platforms on CYTOP focus on hybrid photonic microfluidic devices with optical resonances to analyze water samples [45]. The main benefits of working in the visible range lie in the lower absorption of water at these wavelengths and the availability of selective colorimetric solutions.

1.2.4 Polymer nanostructures for visible light wave-guiding

Two significant drawbacks can occur when fabricating polymer optical devices for visible operation. First, building blocks such as grating couplers, waveguides, and ring resonators require sub-wavelength features that are more challenging to obtain at shorter wavelengths. The second limitation deals with the high sensitivity of polymeric photonic nanostructures to fabrication tolerances at the selected wavelengths. Up to now, these dimensions have been reliably achieved only with dedicated nanofabrication equipment such as Electron Beam Lithography (EBL) and NanoImprint Lithography (NIL). Specific parts such as waveguides and resonators have been successfully fabricated on CYTOP platforms for operation at visible wavelengths with EBL, this technique dedicated to prototyping remains time-consuming and costly [46]. In contrast, soft-NIL is more appropriate for fast and low-cost processing of polymers at the nanoscale. This technique has been successfully applied to direct patterning of polymer waveguides, grating couplers and ring resonators on SiO_2 claddings as reported in [47]. Ring-like structures benefit of both slots waveguides and randomly localized pores to enhance the wave-analyte interaction path. Porous polymers were patterned with nanoimprint lithography by selectively removing one polymer from a blend of two polymers [48]. Similarly, slot polymer waveguides can be used as sensors [49] with a great optical field enhancement. Slot polymer ring resonators are also imprinted with related-imprinting techniques [50]. The cited devices are intended to work at telecoms wavelengths. Very few studies have been published on nanoimprinting polymers for visible operation. For instance, M.Hiltunen et al. reported relevant results on optical sensors based on polymeric slot waveguides with an integrated Young's interferometer operating at 633 nm [51] [52]. Additionally, M. H. M. Salleh et al. have shown a gapless resonator integrated with a microfluidic chip operating at the upper limit of the visible

spectrum ranging from 740 nm to 780 nm [53]. Nevertheless, to our knowledge, full polymer (i.e. core and cladding) platforms on CYTOP using soft-NIL have not yet been addressed in the visible range. Using nanoimprint lithography will definitively represent a significant step forward for future disposable low-cost on-chip biosensors.

1.2.5 Metal-dielectric integrated based structures and Fano resonances

Plasmonic-based structures are also a mainstream transduction element in bio and chemical sensing. A surface plasmon resonance occurs along a metal-dielectric or metal-air interface mainly in the visible and infrared regions of the electromagnetic spectrum. To excite a surface plasmon, the most common configuration is the Kretschmann configuration. A prism is maintained in contact to the metallic layer [54], an input beam is reflected at the prism-metal interface which can generate the surface wave. SPR occurs in two distinct forms: Localized SPR (LSPR) and Propagating Surface Plasmon Polaritons (SPPs). LSPR occurs when the dimensions of a metallic nanostructure are less than the wavelength of incident light, leading to collective but non-propagating oscillations of surface electrons in the metallic nanostructure. Surface plasmon polaritons (SPPs) are the quasiparticles of the coupled modes of an EM field and a surface plasma oscillation. Although surface plasmons SP are not the same as surface plasmon polaritons, from the context, the two are usually confused. Due to their strong radiative damping, the LSPRs usually have a broad linewidth, which significantly limits the performance of the LSPRs-based sensors. An effective way to suppress the radiative loss of LSPRs is by Fano-like resonances, namely coupling LSPRs to other resonant modes with a narrow linewidth (e.g. optical modes) [55]. Due to the boundary conditions, only transverse magnetic (TM) polarized wave can be supported. Metal-dielectric waveguide systems represent the hybridization of plasmonic-optical structures which can be conveniently coupled to optical fibers or integrated with other sensors. The plasmonic mode can be excited with light coupled into a planar waveguide. Excitation of surface plasmon is achieved with an optical planar waveguide for sensing at visible wavelengths in aqueous media [56]. Reciprocally, the light coupling can be done from a plasmonic waveguide to a polymer optical waveguide (PWG), the interaction between the SPP and the optical waveguide mode produces the so-called sharp Fano resonances which can be used for bulk sensing [57]. Following this configuration a SPP mode is excited with the Kretschmann configuration, the metallic layer is maintained in contact with a PWG with a top Cytop ($n=1.34$) cladding forming the interface Ag-Cytop-PMMA. Similar Fano-like resonance predictions are found in [58] [59]. However, experimental results are not shown in the mentioned works. Fano resonances can also be obtained between SPP and SPR [60], despite the good theoretical results the fabrication of gold nanostructures are still incompatible with low-cost processing. An experimental work showing the performance of Fano resonances is reported in [61] where gold nanoslits are fabricated over polymer with an assisted

embossing process, the coupling between SPR and the cavity mode leading to sensitivities up to ≈ 1000 nm/RIU.

Commercial plasmonic devices are already available for both bulk and specific sensing. Due to the lossy propagation of the plasmons, hybrid structures combining broad and sharp resonances are used to produce Fano-like resonances. These devices are compatible with the integration trends. However, the fabrication methods and materials are still far for mass production.

1.3 Previous work

Three main previous works are extensively reviewed to inspire this Ph.D. Each one already addressed one problem regarding sensing and microfluidics, polymer patterning or the optical characterization. The first one was the thesis presented by Meziane [62]. This thesis was oriented towards the detection of hexavalent chromium Cr(VI) in water samples by the colorimetric reaction based on a reaction with the 1,5-diphenylcarbazide (DPC). An extensive study was carried out to integrate both the fluidic function based on Electro Wetting on Dielectric (EWOD) and the sensing function with optical microring resonators. The EWOD chip was achieved as well as the conception, simulation, and fabrication of submicronic microring resonators using stepper lithography. Polymer materials and glass substrates are selected however serious problems concerning fabrication and characterization are encountered:

- Non-repeatable fabrication process at gap and waveguide level
- Low-quality polymer waveguide facets to perform end-butt coupling with optical fibers
- Non-tunable sources at $\lambda = 532$ nm

The first problem is encountered since the waveguide dimensions are very restricted (500 nm x 500 nm) to allow single-mode propagation. These dimensions are difficult to attain with state-of-the-art UV optical photolithography steppers. The same problem is reported to the gap of the ring resonators. Besides, the waveguide present rounded corners. The second problem is related to the cleaving of the polymer, neither polymer nor SiO_2 present crystalline axis, therefore when "cleaved", the facets are of very low quality to perform input-coupling. Grating couplers are proposed in this thesis to overcome this issue. Additional issues are related to the bulky SiO_2 substrate which with a refractive index of 1.5 acts also as a waveguide. Since the refractive index of both SiO_2 and the polymer waveguide are very close, most of the light is coupled to the substrate as parasitic substrate modes, this is avoided by using high index substrates. The last point is the difficulty of characterizing the ring resonator resonances with single wavelength lasers, or relative large LED sources due to the impossibility of couple the light inside the waveguide, or due to the non-existent compact tunable green sources.

From our knowledge, A.Nitkowski (Cornell University of Ithaca) reports the first experimental verification of homogeneous sensing based on colorimetric reaction with microring resonators [63]. The small volume of reagents is managed by a microfluidic cell assembled onto the optical chip based on ring resonators. Nevertheless, in all these studies, the sensitivity and the optimal ring design was never addressed.

Therefore we must provide alternative solutions for the light coupling into the polymer waveguides. To develop a reliable fabrication process with proper polymer coupling structures, we rely on the thesis of Andreas Finn, from the Technischen Universität Dresden who proposed the fabrication of grating coupler structures and waveguides for operation at telecommunication wavelengths. These structures were patterned with fast and low-cost fabrication methods such as UV-nanoimprint lithography. Besides, most of the structure dimensions were transferred to the master mold with optical photolithography. Then, the polymer structures were directly patterned on SiO_2 substrates. The multi-height profile of a polymer grating couplers and waveguide are directly patterned in a single step. Finally, these devices are tested, however, despite ring resonators were also fabricated characterization results were not shown. In this context, our aimed structure is geometrically very similar as the structure shown Fig1.3. The device presents a high index substrate to avoid parasitic modes. Moreover, it is compatible with the deposition of polymer layers of CYTOP providing water-like claddings. The structures present long tapered waveguides with embedded grating couplers to achieve near vertical input coupling. Finally, a ring resonator is added to the design. The device is intended to operate with both air and water top cladding. Alternatively, an output coupler can be added to avoid the mentioned waveguide cleaving.

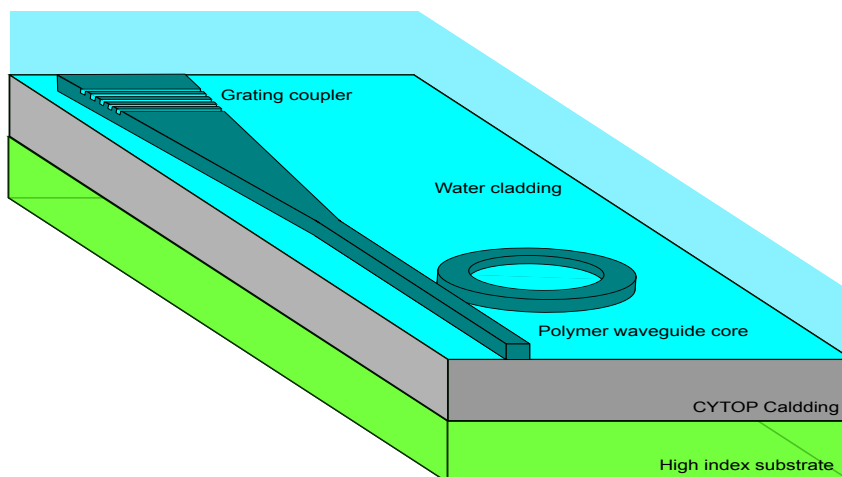


Figure 1.3: Sketch of a structure including an on-chip coupling solution, a waveguide, and a ring resonator. The devices are patterned in the polymer on CYTOP to provide water-like cladding.

1.4 Scope of this thesis

Some work was dedicated to the overall development of integrated chips for the detection of water pollutants. Microfluidic or EWOD based devices handles liquids of analytes and reagents performing the lab on chip task. The homogeneous sensing and the use of colorimetric reagents were already proven experimentally with OMR for other applications rather than monitoring water pollutants. From these main advances our work contributes to the mentioned research. First we provide a reliable process for manufacturing polymer nanostructures for visible light waveguiding. This process must be compatible with fast and low cost techniques which can bring nano-sized polymer structures to marketable devices in the future. The main issue would be leading with sub-wavelength features for operation in the greenish region of the visible spectrum. Besides, we also contribute providing a theoretical background to analyze the sensitivity of OMR for their performances as VIS-spectrometers. Besides, it will support the already present results found in the literature. Thus, this thesis consists of three main chapters:

- The whole background on fabrication, design, and theory is given in Chapter 2. We present the technique of soft-imprint lithography. The main tools of nanopatterning electron beam lithography and nanoimprint lithography are reviewed. We present the design of the structures and a specific design to assist the fabrication process presented before. The design of the structures is supported by finite difference eigenmode solver and finite difference time domain simulations. In the third part of the chapter we propose an analytical approach and design guidelines of the ring resonator parameters studying its performances as visible microspectrometer. The sensing principle is described using 2.5 FDTD simulations for a particular design of the microring. The sensitivity, defined as the ratio of power drop at resonance over the complex refractive index variation, is discussed based on the ring parameters. The optimal coupling configuration is analyzed combining the transmission of the unperturbed ring resonator and the ring resonator in presence of a lossy cladding. The role of the evanescent field, optical length, and coupling mechanism is discussed. FDTD simulations (2.5D) of ring resonators are presented with different geometries to compare the simulations results with the values obtained analytically.
- Within the Chapter 3 we aim to demonstrate the direct patterning of grating couplers and polymer waveguides fabricated on CYTOP by soft-NIL for visible wavelength applications. The first part describes the whole process addressing the main fabrication concerns of the imprint process while the second part allows to characterize and analyze the impact of fabrication tolerances on optical efficiency. As the devices are imprinted from a soft stamp, different soft stamp materials including thermoplastics and hardened recipes of PDMS

are used and compared to each other. The master stamp consists in a multi-height Silicon-On-Insulator (SOI) structure including both tapered sub-micron waveguides (350 nm x 350 nm) and grating couplers (with a pitch equal to 290 nm). It allows a direct imprint process of the multi-height structure in a single step with a minimal residual layer (RL) since excessive RL thickness can degrade the optical performances of the overall structure. Also, optical coupling efficiency measured as a function of the input angle is also presented for different thicknesses of CYTOP. By using such a direct patterning technique, we demonstrate state-of-the-art efficiency and the large angular acceptance width obtained allowing an easy source alignment, that could facilitate the packaging process of future microfluidic chips for sensing applications.

- Finally, we conclude this work and discuss further open questions. Characterization with broadband laser sources are highly recommended to characterize the transmission spectrum of the ring resonator. Complementary we propose to characterize ring resonators by means of varying the top cladding index. Different refractive index liquids can be mixed providing in-situ modification of the top cladding. This can be done with an appropriate microfluidic circuit which is already fabricated. The support to hold the microfluidic circuit is also provided. Regarding the fabrication process, we can stick to the two-step exposure however exposure in a single step is highly recommended since it will divide by two the exposure time. Since the master stamp is the most expensive part of the process, it is crucial to achieving this process for low-cost manufacturing. The cost of the imprint, polymers and others are negligible compared to the cost of the master stamp.

Chapter 2

Basis: Modeling, materials and fabrication

In this chapter, we explore the main aspects regarding fabrication technologies and the design and theoretical performance of the polymer photonic structures presented in this manuscript. The chapter is divided into three subchapters: the fabrication methods (Electron Beam Lithography and Soft-Nano-Imprint Lithography), the design and simulation of the polymer structures and the sensing strategy. The design is presented after the fabrication process since the latter can lead to structure variations that can directly affect the fidelity to the initial design, hence the need to incorporate fabrication process characteristics during the design phase.

The first part focuses on the fabrication of multi-height structures for waveguide applications. These structures combine nano and micro features along several millimeters on the same layer. This combination reveals challenging constraints concerning resolution and processing time for conventional projection lithography which are not optimal techniques to pattern multiple-scale structures over large surfaces. In this context, nanoimprint lithography emerges as an optimum solution to directly pattern micro and nano features overcoming the main issues of projection lithography tools.

Although almost all variations of nanoimprint lithography are reviewed in literature [64] [65], there are infinite combinations of material, dimensions and processing parameters available depending on the final application. Therefore, along with this chapter, we will give an overview of the main insights and considerations for the soft-nanoimprint process developed in this thesis. This process involves several unique aspects such as the realization of a two-height master stamp and a dedicated design to assist the polymer flow during the imprint. To do that, we review the main parameters for the master stamp fabrication including suitable techniques to pattern two-level structures in a silicon wafer. In the same way, we show the main elements to be considered during the nanoimprint lithography as well as the main issues regarding this technique, including residual layer management and soft stamp-related defects. This subchapter ends with the proposal of a complete optimized process flow covering the EBL master stamp realization and the full nanoimprint process.

The second part of this chapter is dedicated to the design of the polymer waveguiding structures. We study how the residual layer affects the operation of the different optical elements, especially regarding optical confinement. In the same way, we study how variations in the grating coupler depth can affect the experimental results. To do that we relied on a commercial mode solver and a finite difference time domain (FDTD) tool both dedicated to photonic design. The theory underlying the behavior of these structures is backed up with simulations or references from the literature. The different simulations provide insight into the optimal geometries to be implemented during the layout design phase.

The third part of this chapter is dedicated to the theoretical study of ring resonators as absorption spectrometers. Once the original background is given in the previous section, we use the main parameters of the ring resonators to define the sensitivity. This expression depends on the sensing strategy which will be previously explained. The expression for the sensitivity is then optimized depending on ring resonators parameter complementing the already well-understood strategies based on the refractive index shift. Simulations were carried out in parallel to check the proposed model.

2.1 Nanofabrication tools for polymer patterning

Micro/nano-optical structures are most commonly transferred to photoresists using projection lithography equipments. Some modern steppers (and scanners) offer appropriate resolution to expose nanometric patterns onto a silicon wafer. By doing this, polymer waveguides and microring resonators have been fabricated with related photolithographic techniques for sensing and telecoms applications [66] [67]. However, despite the ability for some advanced projection lithography tools achieving sub-100 nm resolution [68], the more affordable projection lithography tools (like the Canon FPA 3000i4i-line stepper) are limited to about 300 nm strips of resist, which may be enough depending on the application. On the other hand, Electron Beam Lithography (EBL) is able to directly write nanometric patterns from a layout without going through the intermediate step of generating a photomask, however this process is slow and thus expensive. Alternatively, replication or nano-impression of micro and nanostructures can also be done with mechanical contact between a mold with cavities and a resist. This approach is referred as Nano Imprint Lithography (NIL). The resist fills the cavities of the mold and is then cross-linked via different chemical reactions. This process can be repeated several times from a master, or an intermediate soft, depending on mold damages and aging properties. For example, the Fig.2.1 shows the main steps of a complete soft-NIL process. In Fig.2.1 (a) the intermediate soft stamp is fabricated from a rigid master mold transferred to a soft stamp material. In Fig.2.1 (b) the soft stamp is used to transfer the pattern polarity of the master stamp to an uncured polymer. Once the polymer is hardened, the soft stamp is released as shown in Fig.2.1 (c).

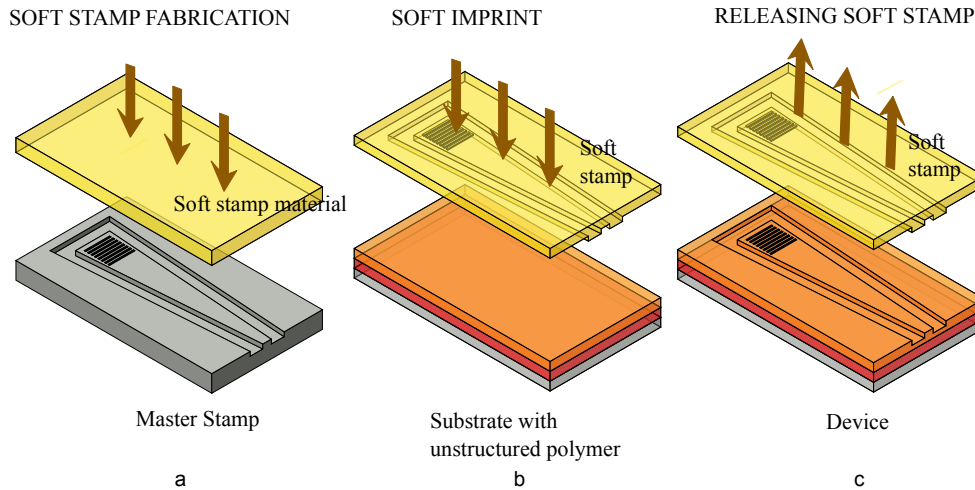


Figure 2.1: Description of the soft-NIL process. (a) First, the soft stamp is replicated from the master stamp in a soft polymer material. (b) Then, the polymer optical devices can be replicated from the soft stamp with an optimized polymer cross-linking. (c) The soft stamp is released

When fabricating polymer nanostructures with soft-NIL, the critical issues lie in the fabrication of the master and intermediate stamps. The master stamps are fabricated either with projection or electron beam lithography techniques depending on the resolution needed and the availability of the equipment. EBL is usually preferred for deep submicron structures. In this thesis, as the resolution provided by the available stepper is not enough, EBL will be used to pattern the features on the master stamp. The intermediate soft stamps allow high-resolution conformal imprints over large surfaces even at low pressures with the additional advantage of preventing master mold damage. However, these stamps are subjected to significant mechanical stresses during fabrication, especially in our case where nanometric, micrometric and millimetric structures cohabit on the same device. Also, special attention must be taken during the nanoimprint to deal with the residual layer (RL) of the photoresist remaining between the mold and the substrate. This layer is due to the difficulty to hold the mold in full contact with the substrate during the imprint process. In the following, we present the technology and the main considerations for the master stamp manufacturing. The same review is presented for the soft stamp replication and soft-imprint lithography. Additionally, we propose a design dedicated to managing the RL implementing dedicated structures around the waveguide to enhance the polymer flow.

2.2 Electron beam lithography

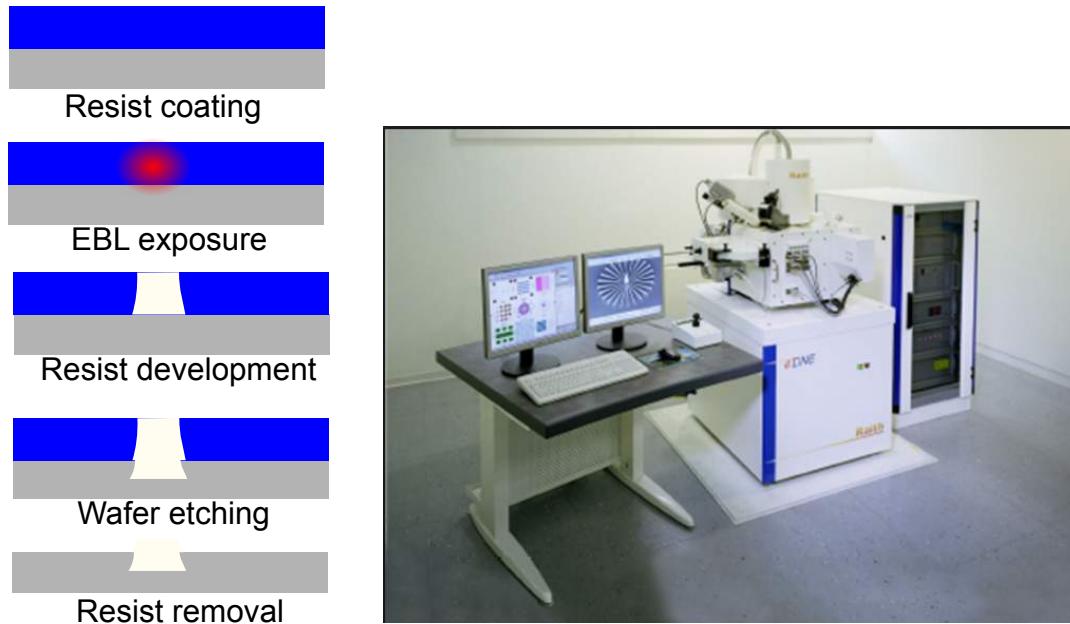
Electron Beam Lithography (EBL) is a direct writing technique that uses an accelerated beam of electrons to pattern features down to sub-10nm on substrates coated

with a sensitive resist. Exposure to the electron beam changes the solubility of the resist by breaking the polymer chains, thus, enabling selective removal of either the exposed or non-exposed regions with the appropriate organic developer. Extensive research have been carried out with EBL providing nanostructuration solutions and prototypes in different research fields (nanoelectronics, metamaterials, nanophotonics...) [69] [70] [71]. Nanometric resolution can be obtained by careful selection of numerous parameters, including exposure dose, beam energy and developer. Outside of a handful of simple cases, a solid process development and optimization phase is required for a concrete application, as this usually differs from the general processes found in the literature [70]. Therefore each application needs its prototype and its dedicated optimization process to correct all the parameters affecting the patterns, including proximity effects, wafer inhomogeneities or temperature drift. As a direct writing technique, the process itself is slow with high maintenance costs. Thus EBL remains a technology most suited for low-volume applications like prototyping, but not convenient for large-scale production where advanced projection lithography is preferred. EBL is also commonly used to fabricate device prototypes in research, as well as to produce industrial optical masks and stamps to be used with faster and high scalable lithographic techniques such as deep and extreme-UV lithography and NIL.

We can distinguish two main writing EBL strategies, the raster scan, and the vector scan. The raster-scan systems meticulously cover the area of the pattern, switching the e-beam on and off as required by the layout. The vector-control systems deflect the beam to follow paths dictated by the pattern. The beam goes to selected coordinates defined on the wafer and makes there the exposure. The electron beam lithography system available at the clean room facility of the LAAS-CNRS laboratory (Raith-150) is based on the raster scan method: this writing strategy must be taken into account when designing the EBL layouts as it will be discussed in the result section. In the Fig.2.2 (a) we show a single EBL process illustrating the main steps to transfer a layout into a silicon wafer: the resist is spin coated onto the wafer, the resist is then exposed to the electron beam according to the design layout before being developed with the appropriate developer. In this example, the unprotected areas are then etched to achieve the required height. Fig.2.2 (b) shows the Raith-150 EBL equipment available in the LAAS-CNRS cleanroom. In the following, we describe the essential elements required to produce a high-quality two-level master stamp.

2.2.1 Organic resist

EBL uses electrons coming from a source that is submitted to an acceleration voltage (expressed in KeV) and focused before reaching the resist. The inelastic collisions of high energy electrons with the resist produce secondary electrons that can be redirected in random directions. This impact produces physicochemical reactions within the resist producing the scission of the polymer chains which can be further removed



(a) EBL process

(b) Raith 150: EBL tool from the LAAS

Figure 2.2: Conformal contact with soft nanoimprint lithography

with dedicated organic solvents. EBL can employ two classes of resist: positive and negative tone resist. The positive resist is more popular for EBL because of the availability of poly (methyl methacrylate) (PMMA). In counterpart, the commercial ZEP resist from ZEON is also frequently used as it offers higher sensitivity and etching resistance than PMMA, but remains much more expensive. PMMA, with its long polymer chains, takes many scission events before the resulting fragments become significantly soluble. Contrarily, in a negative tone resist such as HSQ (Hydrogen SilsesQuioxane) the electrons convert the material to low solubility due to cross-linking reactions that transform small polymer chains into larger, less soluble ones. In this work, we have used PMMA as standard resists for all the EBL process due to the knowledge and previous experience on this photoresist at the LAAS-CNRS, as well as its inexpensiveness.

2.2.2 Refractive ion etching

Refractive Ion Etching (RIE) is an etching technique that combines the classic physical sputter etching and the pure chemical plasma etching [72]. This combination represents a good trade-off between anisotropy, selectivity, etching rate and damage. The process takes place inside a plasma reactor, and different gases are injected into the process chamber. The gases are maintained at low pressure. Then an electric field (RF) (13.56 MHz) is generated between two electrodes to ionize the gases, thus generating the plasma. During this process, several particles such as charged ions and electrons are generated. These electrons generate a DC bias voltage between the electrodes which serves to accelerate the ions (reactive ions) towards the surface. The

ions react chemically and physically with the wafer surface. RIE can produce very anisotropic etch profiles, which contrasts with the typically isotropic profiles of wet chemical etching. Concretely, RIE will be used in this thesis during the master stamp manufacturing process to create two-level structures in silicon wafers. By using silicon wafers and PMMA, we have been able to benefit from the previous experience of the LAAS-CNRS cleanroom on these materials through existing RIE recipes available on their Alcatel AMS4200. This equipment possesses an optical imaging system to monitor the etching process that dramatically facilitates the optimization phase. We are going to review the main factors contributing to the structure fidelity and their impact on the optical design and final performance.

2.2.3 Beam energy

One of the major considerations regarding EBL patterning is the beam energy. High resolution EBL needs high vacuum and high energies up to 200 KeV, implying complex high power electronics. Hopefully, regarding our resolution requirements (100 nm), typical EBL energies between 15 and 30 KeV are usually enough. Most of the in-house developed process have been optimized for these writing energies, thus focusing and corrections can be done easily. Typical dose and energy test are car-

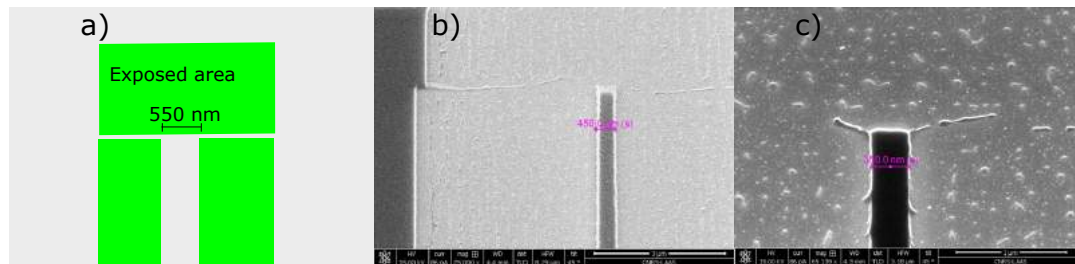


Figure 2.3: (a) Layout example with the patterned area (green) in PMMA. The middle strip will remain on the resist after development (b) SEM image of the patterned design at 20 KeV. (c) SEM image of the patterned design at 30 KeV

ried out to study the response of the resist to an arrangement of exposed areas defined by the layout. For example, in the Fig.2.3 we show the exposure (green) of a 400nm thick layer of PMMA containing two trenches, thus leaving a strip of resist in the middle. After exposure the device is developed with an organic resist and the broken polymer chains are removed. We can observe that the initial linewidth of 550 nm in the layout results in 450 nm for 20 KeV and 350 nm for 30 KeV of the electron energy for the same dose. However the final line width obtained on resist may be different for different doses, different resist developers, and different trench width (green). Monte Carlo simulations can be done to understand the correlation between beam energy and resist thickness by studying the trajectories of the electrons along the resist. Typically 5 to 10 KeV are needed to break the polymer chains of PMMA. The trajectories of the electrons for two different thicknesses of PMMA

resist at distinct accelerating voltages are simulated with the CASINO software¹. The Fig.2.4 show the penetration of 5 KeV accelerated electrons for 400 nm and 40 nm thick PMMA layers. These diagrams gives an insight of the final resist profile without considering neither the dose ($\mu\text{C}/\text{cm}^2$) nor the resist developer. The resulting resist profile shown is a combination of the incident electrons (yellow) which progressively lose their energy (blue) and the back-scattered electrons (red). While

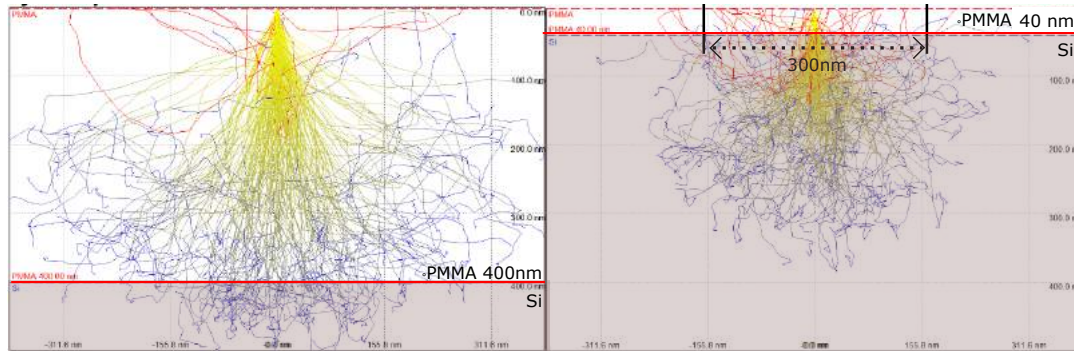


Figure 2.4: Montecarlo simulation showing the different electron trajectories at 5 KeV on 400 nm of PMMA thickness (left) and on 40 nm of PMMA thickness (right). The Si wafer is considered infinite

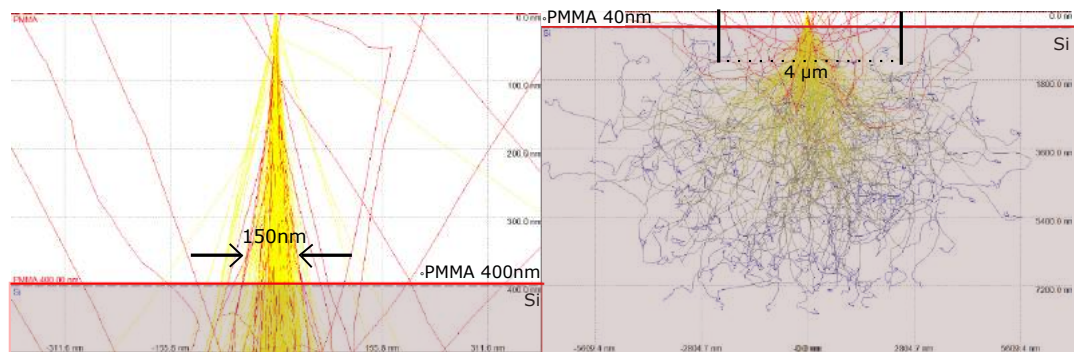


Figure 2.5: Montecarlo simulation showing the different electron trajectories at 30 KeV on 400 nm of PMMA thickness (left) and on 40 nm of PMMA thickness (right).

electrons break polymer chains during their travel through the resist thickness, some of the incident electrons are back-scattered (as shown in red on Fig.2.4) which also contributes to the polymer chain scission. However, a 5 KeV beam energy is not sufficient to fully penetrate the 400 nm thick layer of PMMA. Another phenomenon visible through this simulation is the forward broadening of the electron trajectories that produces a horizontal molecular weight gradient, which can produce the rounded pattern and undercuts on the resist after the revelation, thus expanding the impact point to (~ 300 nm). Contrarily if the PMMA thickness is reduced to 40 nm, this energy is enough to expose all the resist thickness. However, we can observe that the backscattered electrons are much more critical due to the presence of the Si interface. The Fig.2.5 shows the same material configuration when the resist is exposed

¹<http://www.gel.usherbrooke.ca/casino/What.html>

to electrons accelerated at 30 KeV. We appreciate that the electron beam profoundly penetrates along the full thickness of resist compared to the 5 KeV case. The electron beam broadening due to forward scattering is also significantly reduced in the resist at 30 KeV compared to the 5 KeV case, reducing molecular weight gradients both in the vertical and the horizontal direction. At 30 KeV backscattered electrons produce proximity effect several microns away from the beam impact point ($\sim 3 \mu\text{m}$ red trajectories). These proximity effects are of foremost importance when designing closely spaced patterns, like in our case for the grating couplers or the gap region of the ring resonator. Our efforts should focus on working with the highest energy to fully expose the 400 nm thick PMMA layer with a reduced beam broadening². At higher energies (30 KeV), backscattered electrons will be sent several microns away from the exposed features but compared to the 5 KeV case proximity effects are reduced locally. This will be depicted when optimizing the gap region of the ring resonator.

2.2.4 Master stamp materials

The choice of the master stamp material is usually derived from the resist properties in which the patterns need to be transferred. Opaque stamps such as Si, SOI, or nickel stamps well suited for T-NIL where the resist hardening process is performed with temperature. These traditional materials are compatible with conventional etching process and surface treatments. However, if UV-NIL is required, the master stamp or the wafer must be transparent to UV radiation. In that case, quartz or silica is the most commonly used. While Si molds are considered as easy to pattern with EBL, quartz or silica molds are a bit more challenging to obtain especially for features smaller than 50nm mostly because of charging effects [73].

However, the inherent fragility of these highly rigid molds makes them prone to failure, especially when exposed to dust particles during the imprint process, which considering the high price of these rigid molds is considered as a major drawback. Commercial rigid molds with dense grating networks can cost several thousand of euros depending on their resolution and surface. In the case of large-scale stamps, which have a high density of nanoscale patterns, the area of contact of the stamp with the NIL resin increases, thus increasing the risk of deterioration when the same silicon stamp is repeatedly employed. These drawbacks can be quickly resolved using metallic molds which can offer more excellent mechanical properties and durability than Si molds. Another popular alternative to preserve the master stamp is the use of an intermediate soft stamp to perform the imprint. Different soft stamp materials will be reviewed in the nanoimprint section. Despite the aforementioned drawbacks of Si as a master stamp, it remains the most obvious choice, especially

²This resist thickness is enough to etch waveguide strip with typical height between 300nm-600nm in Si.

when considering the availability of dry-etch processes with comparably high selectivity to conventional resist materials such as PMMA. Therefore, the material used for our master stamp will be a classical Si wafer.

2.2.5 EBL Resist choice

Several approaches can be used to fabricate two-level structures onto a Si master mold. In our case, to avoid contamination or degradation of the master mold, we favored the approach of an intermediate soft stamp. This choice implies that the polarity of the master stamp should be the same than the final device one as previously shown in the Fig.2.1.

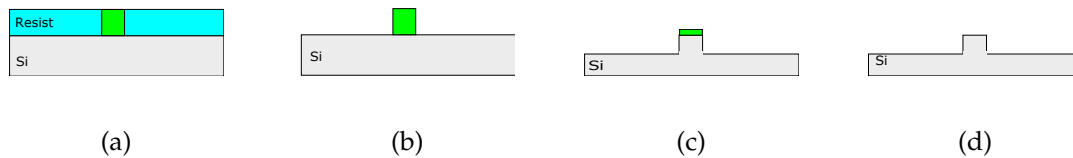


Figure 2.6: EBL process flow with one etching process with negative resist (a) A thin layer of negative resist is exposed (green) with the electron beam. (b) The isolated resist remains, the unexposed resist is diluted in the solvent. (c) The device is etched, the remaining resist protects the waveguide region. (d) The remaining resist is removed thus the pattern is transferred to the master stamp

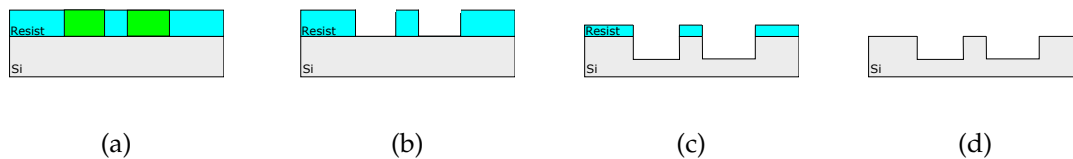


Figure 2.7: EBL process flow to pattern with positive resist. (a) A thin layer of positive resist is exposed (green) with the electron beam. (b) The isolated resist with broken polymer chains is removed by the solvent, the unexposed resist remains on the wafer. (c) The device is etched, the remaining resist protects the trenches for their waveguide region. (d) The remaining resist is removed thus the pattern is transferred to the master stamp

Such a structure can be obtained by directly patterning a strip waveguide and the grating coupler with a negative tone resist (HSQ) or by patterning the edges of the nanostructure using a positive-tone resist like PMMA. The straightforward isolation of a Si strip in negative tone resist is depicted in the Fig.2.6 for the case of a single level pattern. The desired waveguide region is isolated directly with the electron beam. Consequently, the resist protects the Si strip (waveguide) region during the Si etching process. Alternatively, the isolation can be done with a positive resist as shown in Fig.2.7. In this case, the edges of the structure are exposed creating two trenches with a strip of resist in the middle. Then, as the electron beam breaks the polymer chains of the resist, the isolated edges can be removed with the appropriate developer. The resist completely protects the wafer during the etching step except on the outline of the waveguide. The future waveguide height is determined by the

etching depth. This isolation strategy can greatly assist the imprint process and will be our preferred choice as we will discuss in the nanoimprint section.

2.2.6 Process flow for multi-height master stamps

Two main approaches to fabricate multi-level master stamps have been evaluated in this work. The first method consists of two continuous spin coating processes and one wafer alignment step. The second method consists of using variable doses to obtain distinct revelation ratio of the exposed areas, thus modulating the final structure height. The first method is outlined in the Fig.2.8. A thin layer of positive

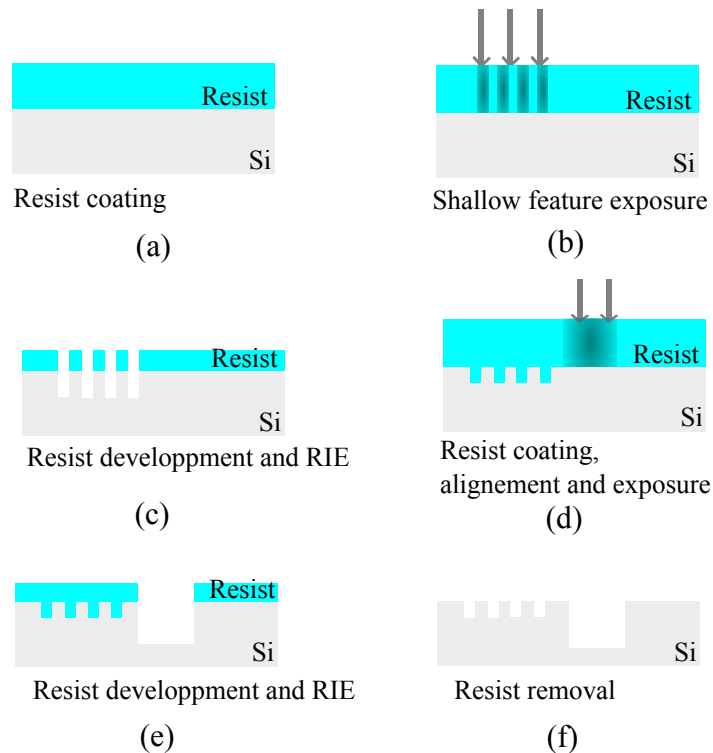


Figure 2.8: Transversal cross section showing the master stamp fabrication in two steps with two level height (for both grating and waveguide). (a) Resist coating of the wafer. (b) Fully exposure of the shallower features (grating). (c) We etch the exposed features to attain the desired height, the remaining resist is removed. (d) The wafer with the grating is re-coated with resist. (e) The deeper trenches (Waveguide) are developed and etched. (f) The rest of resist is removed

resist is spin coated onto the substrate (Fig.2.8 (a)), this layer should be thick enough to ensure adequate exposure (Fig.2.8 (b)) and etching (Fig.2.8 (c)) of the shallower structures, hereby the grating coupler. After the resist development and etching the second step consist in a second spin coating of the nanostructured wafer with a layer thick enough to ensure a flat layer of resist covering the gratings. The second exposure (Fig.2.8 (d)) will define the edges of the waveguide. These edges match the final waveguide height after the etching process (Fig.2.8 (e)). Finally, the resist is removed, and the master stamp is ready to be used (Fig.2.8 (f)). This method suffers from a few drawbacks: the need for a precise alignment step before the second

exposure (implying the need for alignment marks during the first exposure), and the need to perform two spin-coating/development steps that increase the potential process failure through contamination.

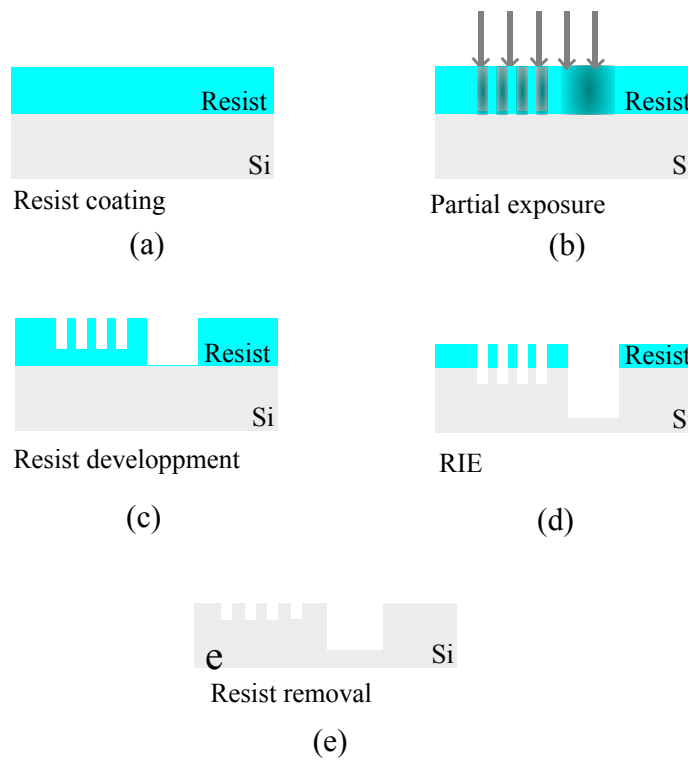


Figure 2.9: Transversal cross section showing the master stamp fabrication in a single step with the grating and waveguide features (a) Resist coating with the optimized thickness to completely etch the trenches defining the waveguide height. (b) Exposure at different doses of both waveguide (higher) and grating (lower). (c) Same resist development time provides different resist height profiles. (d) Two different heights are attained on Si after RIE. (e) Resist removal

Compared to the first method the second strategy is based on one single exposure and one single etching process and is known as gray-scale lithography (Fig.2.9). The main principle of the gray-scale lithography is based on the relationship between the applied dose and the solubility of the exposed resist. Higher doses break the resist in small fragments compared to features exposed at lower doses. Therefore, the features exposed at different doses will present different solubility (development ratio) in presence of the same developer. Thus, after the development process, more soluble structures present deeper features than the less soluble ones. Then, the higher doses are applied to the deeper structures (waveguide edges) while the lower doses are applied to the shallower structures (the grating couplers) as illustrated in Fig.2.9 (a) and Fig.2.9 (b). Therefore, during the development of the resist, the edges of the waveguide (higher doses) are fully removed while a thin layer of resist will still protect the grating couplers during the etching process (Fig.2.9 (c)). This thin layer of

resist will tune the height difference between the waveguide and the grating coupler due to the different etching rate between the wafer material (Si) and the resist (PMMA) (Fig.2.9 (d)). Finally the remaining resist is removed (Fig.2.9 (e)). Despite this process being more time efficient (single exposure), obtaining the appropriate set of parameters is time-consuming and challenging, because one needs to optimize the dose of the different features (grating/waveguide) to achieve two different heights during the etching. During this work, the double exposure was favored as it provided the best compromise in term of results vs. process development time, mainly due to the previous experience acquired by the cleanroom staff. Tests performed with the gray-scale lithography method were still encouraging but would need further tests that would have been out of the scope of this work.

2.3 Nanoimprint lithography

NIL technology is a direct nanoscale patterning method based on the deformation of a resist, which is then cured either by heat, UV, or an adequate combination of both. As the resist is patterned mechanically this technique is not limited by optical diffraction since the features are already defined on the Si master mold. The particular advantage of NIL compared to other lithography techniques is the ability to fabricate large-area and complex three-dimensional micro/nanostructures with low cost and high throughput. However, there are several parameters affecting the aimed patterning results which are the residual layer (RL) and the homogeneity of this layer. The RL appears due to the difficulty to get the mold in full contact with the substrate during the imprint process. The Fig.2.10 shows the cross-section of a wafer with a rectangular strip that should be obtained with a dedicated mold previously done using EBL or optical photolithography. This mold has the opposite polarity and geometry compared to the final device. First, a curable resist is spin-coated on a wafer, then the mold brought into contact and held with a controlled pressure onto the uncured polymer. Depending on the polymer, the cross-linking is achieved from Thermal Nanoimprint Lithography (T-NIL), UV Nanoimprint lithography (UV-NIL) or a combination of both. Some UV photoresist such as SU-8 rely on thermal heating to enhance the cavity filling before the cross-linking effect. Once the polymer is hardened, the soft stamp is released. However, an undesirable residual layer of resist remains between the aimed waveguide strip and the wafer. Therefore, the imprinted waveguide consists of a slab with a strip superimposed onto it. This will affect the confinement of the light and therefore the overall performance of both the grating coupler and the ring resonator. Additional defects can be found during the molding and mold removal. Several thesis and papers have been done studying the different defects as well as the destructive and non-destructive methods to analyze the imprinted devices [74] [75]. For example, particles on the wafer surface can lead to partial contact between the wafer and the mold, resulting in non-imprinted areas in a large radius around the particle or in the partial cavity filling [76] [77]. While

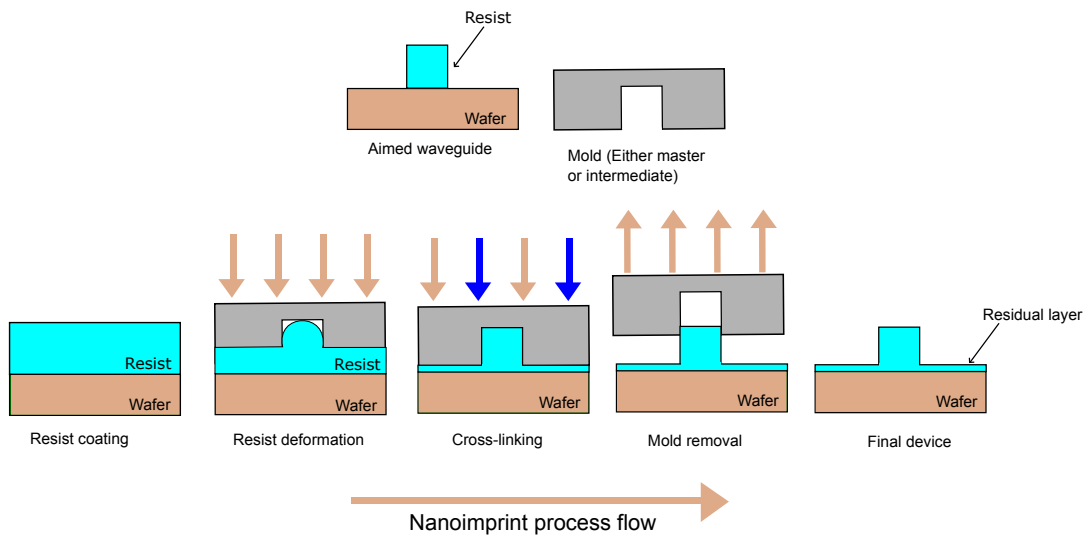


Figure 2.10: Description of the nanoimprint process for waveguide replication. The polymer optical device can be replicated from the stamp. The stamp is held in contact during the cross-linking process of the polymer. Finally, when the stamp is released a thin slab residual layer remains which will affect optical performances.

defects related to particles can be avoided by thorough cleaning procedures as well as meticulous filtering of the resists and chemicals, the residual layer is more problematic, especially for waveguiding applications. In this section, we review the main issues associated with the soft-NIL process. Different materials for the soft stamp are reviewed depending on the processing time and material properties, as well as the main issues affecting each material. Different high index photoresists are compared based on the processing guidelines found in the literature and our own experience. Finally, we present the obtained process flow integrating all the elements discussed along this section.

2.3.1 Surface treatment: Anti-sticking and adhesion enhancement

NIL processes rely on a mechanical contact between the stamp and the polymer. During molding and demolding imprint, layers can be subjected to temperature variations and high mechanical stress. Therefore, the adhesion of the stacked layers should be enough to hold the full process. It is, however, essential to minimize the interaction forces between the polymer and the stamp by providing stamps with good anti-sticking surface properties. These properties will ease the demolding step while reducing the eventuality of peeling up structures while preserving the stamp lifetime by limiting contaminations. Hydrophobic or anti-sticking treatments are applied to reduce the surface energy of the stamp and thus minimize the adhesion. Some thermoplastics and elastomers such as PDMS already present low surface energy, so anti-sticking treatment is usually not required on these soft stamp materials. However, an anti-sticking treatment is highly recommended on the Si master stamp to favor the mold release during the imprint of the soft stamp, avoid ripping-off the

structures and sidewall detachment of the waveguide embossed in the intermediate stamps. Several treatments exist depending on the surface and the feature size. During this work, we had access to a Surface Preparation Deposition (SPD) equipment from Memstar, that has the ability to deposit Self Assembled Monolayers of specific molecules through vapor phase deposition. In our case, an hydrophobic surface is obtained on the Si mold using Perfluorodecyltrichlorosilane (FDTS) [78] [79]. A contact angle up to 106° for deionized water droplets can be obtained with this treatment that can withstand numerous imprints of soft stamps and holds up against common organic solvents which makes cleaning the mold easy if necessary.

2.3.2 The low index cladding

While the adhesion between the soft mold and the sample must be kept to a minimum to favor unmolding, the adhesion between each stacked layers that compose the photonic structures must be maximized to avoid delamination. In our case, the structures are based on a Si substrate covered by a CYTOP cladding, atop of which a high index resist guiding layer is deposited. CYTOP is a fluoropolymer which has become popular for the fabrication of photonic structures, especially in the sensing field for liquid environments due to its refractive index of 1.34 which is similar to water [80] [81]. This material exhibits excellent optical and chemical properties. Our selected reference of CYTOP (CTL-809M) integrates functional groups that form chemical bonds after heat treatment with substrates like Si, resulting in covalent bonding and excellent adhesion without pretreatment like silanization. However, its highly hydrophobic nature (average contact angle for water is about 108°) renders spin-coating of additional layers almost impossible without prior treatment. It is well known that oxygen plasma induces hydrophilic response on silicon surfaces related to the formation of hydroxide groups [82] [83], but contradictory information of the effect of oxygen plasma on CYTOP can be found in the literature [84] [46]. In our case we came to the same conclusion as Agnarsson et al. with no significant decrease of contact angle after the exposition of CYTOP to oxygen plasma; thus the same method of aluminum coating followed by chemical etching before spin-coating of the waveguiding material has been adopted. This method has proved to be very reliable and gives a contact angle of less than 20° which allows spin-coating in good conditions.

2.3.3 Soft-imprint lithography

Several nanoimprint strategies can be envisaged, and are generally classified into two fundamental categories: Hot-Embossing Lithography (HEL), most commonly referred as Thermal Nanoimprint Lithography (TNIL) and UV-NIL. Soft Nanoimprint Lithography (soft-NIL) is a complementary technique of NIL consisting in patterning nanostructures by using a flexible and transparent stamp, made of poly (dimethylsiloxane) or thermoplastic materials, corresponding to the counterpart of a

single hard master mold. The process enables to define submicron patterns with different thicknesses over large areas in a single step process and appears as an optimal technique to imprint large waveguides with sub-wavelength grating on polymers. The use of intermediate soft stamps presents two main advantages over the use of master stamps:

- Intermediate stamps are usually done with rubbers, plastics or polymer which are easy and cheap to fabricate with thermal embossing or elastomer casting.
- They are usually transparent allowing UV cross-linking. Therefore master stamps can be done with non-transparent materials as Si.

The main inconvenient about directly imprinting with the master stamp is the risk of breaking an expensive wafer patterned by EBL. Optimizing the imprint parameters requires multiple tests to assess the optimum temperature and pressure conditions. These numerous imprints coupled with cleaning procedures can damage the master mold. An intermediate soft stamp can be fabricated by direct replication of the master stamp, and still be used for multiple imprints without deterioration, this solution is highly desirable especially during process optimization :

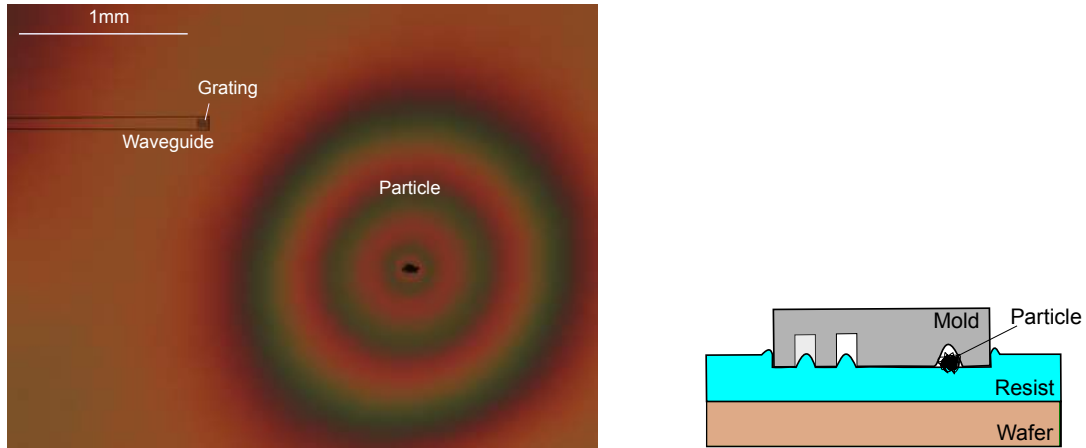
- Conformal contact is achieved over large areas since the flexible stamp follows the substrate shape. This is also useful because the stamp can locally deform around a particle avoiding damage of both the stamp or the substrate
- Flexible stamps can deform at ambient temperature facilitating the mold release which avoids wafer damage.
- Rubbers, silicones and thermoplastics usually have inherently low surface energy, therefore no anti-sticking treatment is required before using the soft stamp.

2.3.4 Intermediate soft stamp materials

We have considered several materials to manufacture the soft stamps. Considering the structure heterogeneity, for the intermediate soft stamp fabrication, we have selected two thermoplastics with different glass-transition temperature (T_g) and compared them to two PDMS recipes which are commonly used as soft stamps:

- Cyclic Olefin Polymer (COP) Zeonor 1060R from ZEONEX ($T_g=130^\circ\text{C}$)
- Cyclic Olefin Copolymer (COC)COC8007from TOPAS ($T_g=75^\circ\text{C}$).
- ClassicSylgard 184 PDMS (1:10 ratio)
- h-PDMS based on the formulation described in [85]

Each material presents different advantages and drawbacks depending on the feature size and the final application. The main thermo-mechanical properties to be



(a) Microscope image of a wafer covered with resist. The soft material allowed the conformal contact even in presence of a dust particle nearby the structures

(b) The conformal contact between the resist and the mold is achieved even in presence of a particle due to the deformation of the soft material

Figure 2.11: Conformal contact with soft nanoimprint lithography

Table 2.1: Thermomechanical properties of some soft stamp materials

Material	T_g	CTE	Processing	Time cost	Young Modulus (MPa)
PDMS	125°C	9.6×10^{-4}	Casting	hours	0.36-0.87
h-PDMS	-	-	Casting	hours to days	9-10
COP1060R	130°C	0.6×10^{-4}	Embossing	min	2100
COC8007	75°	0.6×10^{-4}	Embossing	min	2600-3600

considered for soft stamp fabrication are summarized in table 2.1. PDMS, a flexible elastomeric material which is extensively used in microfluidics and injection molding is very convenient for molding/demolding at ambient temperature. Imprint can also be done without specific clean room facilities due to the capillary forces between the resist and the PDMS stamp. However, due to his low Young modulus, deformations and collapses are routinely observed for structures smaller than $1\mu m$ [86]. The production of our structures using the standard PDMS, exhibited systematic ground collapse.

A modified PDMS with a Young modulus more than 10 times higher than conventional PDMS, namely h-PDMS, has been also considered. In that case, the soft stamp consists in an hybrid combination of hard/soft materials and is referred as hybrid nanoimprint-soft lithography [87]. To achieve sub-300nm period gratings, Philips and SCIL *Nanoimprint solutions* have developed X-PDMS for their hybrid stamps which is also a modified PDMS material with a Young modulus up to 80MPa.

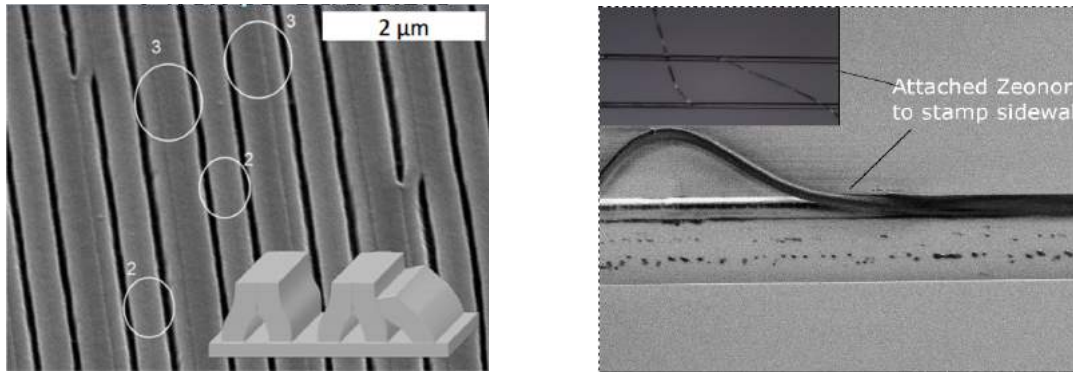
2.3.5 Defects associated to the soft stamp

While h-PDMS and X-PDMS can be considered as a viable option in some cases, their processing is highly time-consuming: in order to guarantee the structural stability of the patterns during the hybrid soft stamp processing, h-PDMS/X-PDMS curing steps must be performed at low temperatures (usually between 50°C to 80°C) over very long times (from several hours to several days depending on the resolution required). This time penalty is not desirable especially during a process optimization time, especially considering that these hybrid PDMS based stamps can be deformed during manipulation due to strain and bending, and are prone to contamination or aging. H-PDMS pushes the limits of the achievable resolution before observing structure collapses, offering the possibility to realize 440nm period gratings with only minor defects. Smaller features are however still out of reach, as illustrated by Fig.2.12 (a) that shows a partial collapse of 290nm period grating, which is usually attributed to the superficial charges built up during the imprint or the capillary forces [88].

On the other hand COC1060R (ZEONOR) and COC8007(TOPAS) are thermoplastic films used for optical molding due to the excellent properties in terms of low birefringence, low water absorption, and high stiffness that are important in optical components. TOPAS is the brand name of the cyclic olefin copolymer manufactured by Topas Advanced Polymers GmbH, and it is an amorphous transparent copolymer. Contrarily ZEONOR is the brand name of the cyclic olefin polymer furnished by ZEON corporation. Both materials are used in applications concerning submicrometric plastic molding [89] [90], microfluidics [91] but also for plastic optical fiber fabrication [92] [93]. Some more specific studies can be found on their suitability to nanoimprint lithography [94] or optical components [95] The Young modulus of ZEONOR and TOPAS allows for imprinting without collapsing problems with closely spaced structures. However, the processing of these materials requires much higher temperatures than PDMS-based stamps (above T_g), thus two main concerns can occur:

- Depending on the applied temperature and pressure it will be a gradual thermo-mechanical constraint created between the thermoplastic and the master stamp during the embossing.
- The difference in thermal expansion coefficient between the thermoplastic and the Si master mold during the cool down step can slightly alter the dimensions of the replicated structures.

The required pressure and temperature profiles during imprint is highly dependent on the substrate size and the pattern resolution, so it is a good practice to optimize these parameters for each geometry. The thermal expansion coefficient difference between the stamp and the thermoplastics can lead to a partial detachment of the sidewalls as illustrated Fig.2.12 (b). This type of defect, that appears during



(a) Collapsed grating of h-PDMS ($\Delta = 300nm$)

(b) ZEONOR scission attached to the master stamp

Figure 2.12: Defectivity associated to PDMS based materials and COP/COC materials

the demolding process, can be avoided with process optimization. It was visible only under certain conditions and is a consequence of the important length of our waveguides (up to 7 mm) and their relatively important depth (about 400nm). Previous experiments in the LAAS cleanroom with ZEONOR did not reveal these type of defects, implying that the geometry of our spatially heterogeneous structures was the most obvious reason. The optimum pressure/temperature profiles must allow complete cavity filling over the dense grating couplers, while minimizing thermo-mechanical problems to avoid the afore mentioned defects. During our testing campaigns, TOPASCOC8007, with its lower T_g (65°C less than ZEONOR COC 1060R), has shown significantly less thermo-mechanical associated defects since it allows for thermal embossing at lower temperatures. Each of these soft stamp materials offers various advantages and drawbacks, and as such one must select the most suitable based on the whole process. In our case, TOPAS COC8007 has proven to be the best match in terms of transfer quality, ease-of-use and processing time, while remaining the cheapest option. The PDMS based stamps can be very useful, but some special attention must be paid for sub-micron structures like our grating where adapting the young modulus becomes necessary to avoid collapsing phenomenon. However, PDMS preparation and curing is a much longer process compared with hot embossing of thermoplastics, and the hybrid stamps does not offer very long lifetime over repeated usage. Thermoplastic materials, after an optimization to minimize the thermo-mechanical constraints during the embossing, have proven to be a suitable alternative to hybrid PDMS stamps.

2.3.6 Curable polymers for waveguide fabrication

Thermoplastics like PMMA are commonly used in T-NIL but their high viscosity can lead to inhomogeneities of residual layer thickness in heterogeneous patterns. Oppositely, monomers exhibit low viscosity and are imprinted easily and polymerized with UV-NIL processes. Besides, these monomers can be also used for T-NIL

[96]. Hybrid polymers are also available, containing both organic and inorganic elements to tune their final physicochemical properties (viscosity, refractive index...). Ormocore from *micro – resist technology GmbH* offer glass-like material properties after UV curing with a relatively high refractive index ($n=1.56$, $\lambda = 580$ nm). Several polymers are affected by the so-called inhibition layer issue when exposed to atmosphere, or most specifically to oxygen. This phenomenon is observed especially on acrylate-based mono or oligomers. As Ormocore is an acrylic based polymer the presence of oxygen will also create an inhibition layer when exposed under ambient atmosphere. This is due to partial quenching of radical polymerization by oxygen that results in a layer of uncured material on the surface. To avoid this issue, the imprint should be performed within vacuum, or the purge of an active imprint site with inert gases might be used.

SU-8 is an epoxy-based amplified negative photoresist, that qualifies as an ideal candidate for NIL and optical photolithography due to its low glass transition temperature (60°C) and low volume shrinkage coefficient. However, it requires a thermal assistance before UV exposure (significantly above T_g , 60°C , of uncured SU-8) to physically deform the resist shape adopting the mold relief [97]. The rule of thumb is that imprinting temperature should be below 95°C to prevent degassing. The process is usually more complex to optimize and the soft stamps should present higher T_g than the required temperature for the SU-8 processing which is usually comprised between 70°C and 90°C [98]. Finally, the NIL-UV394 resist ($n=1.52$ $\lambda = 500$ nm) has been developed in-house at the LAAS-CNRS for UV-NIL applications. Based on methacrylate, it is designed so that it prevents dewetting upon contact with COP or COC based soft molds. The solvent-free composition ensures that no bubbles are trapped into the cured resist while allowing soft-UVNIL at room temperature polymer cross-linking is directly achieved with UV radiation.

During this thesis, the soft stamp materials and the curable polymers mentioned above have been tested and evaluated on our specific geometries. SU-8 2000.5 was initially selected as our material of choice for waveguides due to its good optical properties and its availability. However, due to the need for SU-8 to be imprinted at temperatures on the same order than the glass transition temperature of TOPAS soft stamp, this combination shown imperfections as the soft stamp was damaged during the imprint, resulting in deformed structures. Finally, a combination of TOPAS COC8007 and Ormocore or NIL-UV394 was retained. The combination of SU-8 and ZEONOR can still be used depending on the device geometry, but in our case the results were less reproducible than for TOPAS and Ormocore or NIL-UV394.

The final conclusions are described here

- PMMA: Thermal-NIL, compatible with hard stamps or soft stamps with high T_g .
- SU-8: Thermal UV-NIL, hard stamps or ZEONOR stamps are needed.
- Ormocore: UV-NIL, all kind of stamps can be used.

- NILUV394: UV-NIL, all kind of stamps can be used.

TheOrmocore and the NILUV394 were prioritized.

2.3.7 Squeeze flow of thin films

We must consider several key points about the polymer flow when is squeezed by the protrusions of the master stamp. It has already been shown that resist flows only occur near stamp cavities and protrusions, and that polymer volume is constant at the period scale [99] [100]. During the process of nanoimprint lithography a small vertical displacement of the stamp results in a large lateral flow of the polymer filling the cavity of the stamp. However, the displacement of thin films of polymers over large distances require high pressures and very long processing times which may lead to additional stresses on wafer and stamp. The Fig.2.13 shows a schematic representation of the polymer flow. A single array of nanostructures surrounded of semi-infinite protrusions will displace the thin film of polymer over a large distance. The same behavior is expected with a single microcavity occupying a similar space on the wafer as the nanostructure array³.

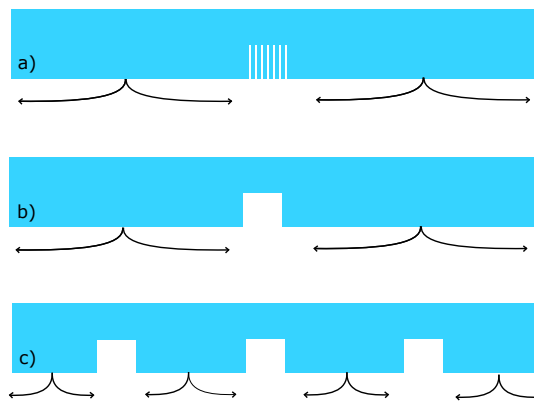


Figure 2.13: Comparison between different polymer flow regimes. (a) Polymer must flow over large distances to fulfill the nanostructures of the stamp. (b) The filling of a microcavity also needs to displace polymer over large distances.(c) By the introduction of several sink structures or indenter the polymer flow is enhanced.

We must take special attention to the fact that the residual layer and the filling ratio strongly depend on the processing parameters, but also on the cavity geometry. Short cavities are going to be fulfilled before larger cavities, [102] and this has important implications regarding the Residual Layer (RL). The different protrusion sizes imply different sinking rates producing inhomogeneities in the RL on the adjacent cavities. In addition, the soft-stamp can bend locally thus resulting in a residual layer height that may not be uniform over the entire embossing area. Therefore a specific design must be considered to overcome this issue. One technique to locally reduce the RL and enhance the polymer flow is the so called Minimum Polymer

³Overall the polymer flows similarly around the features but the filling regime may be different (single peak vs double peak) [101]

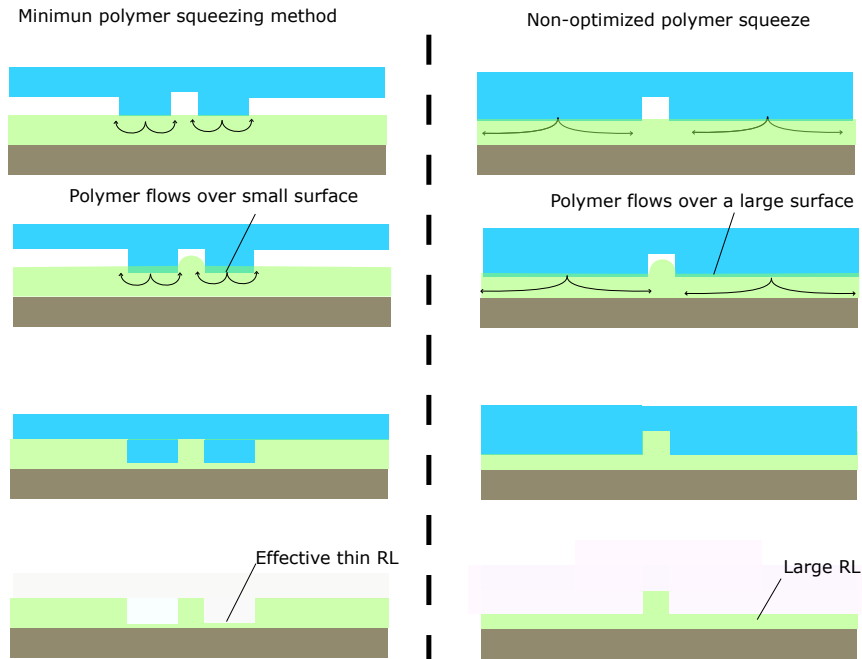


Figure 2.14: Process flow comparison between the use of a non-optimized stamp and a stamp designed considering the MPSM

Squeezing Method (MPSM) [103]. This technique consists in two trenches outlining the cavity which must be imprinted, in our case on both sides of the strip (waveguide). By doing this, the flow resistance of the polymer is lower because less quantity of materials needs to be moved. As the surface of the mold in contact with the polymer is smaller the shrinking velocity is greatly increased compared to the single cavity. Both methods are compared in Fig.2.14. We can appreciate that the main difference to fulfill the cavity is that the polymer must flow over different distances corresponding to the area of the protrusions. If the area is larger we will need more pressure to correctly fulfill the features compared to the MPSM. We would also like to draw the reader's attention to the minimized residual layer obtained with the MPSM. A cross-sectional front view of our waveguide consists in a slab with a strip which in integrated optics is referred as a rib waveguide. The optical confinement and the modal properties will depend on both the rectangular dimension and the slab height, so controlling the RL thickness is highly important.

2.3.8 Desired process flow

The summary of the materials for each step is shown in the Fig. 2.15. The main considerations regarding the presented device capabilities lead to the desired process flow shown in the Fig.2.16. In Fig.2.16 (a) the master stamp can be fabricated following either the double step exposure or the gray scale strategy. Independently, the isolation strategy followed by the master stamp must contain trenches that surrounds the structures to assist the polymer flow during the imprint. As mentioned earlier, the main problem with this strategy relies on the optimization of the proximity effects for the grating grooves, waveguide width and gap of the ring resonator. The

Stamps	Master stamp	Si substrate Positive resist (PMMA) EBL double step exposure
	Soft stamp	TOPAS COC8007
Device	Substrate	Si
	Cladding	CYTOP + Surface treatment
	Guiding layer	Ormocore/NILUV394

Figure 2.15: Summary of the final choices for the fabrication process.

Fig.2.16 (b) illustrates the fabrication process for the soft-stamp with the use of hot embossing. The process starts with a monolayer deposition of an anti-sticking layer to facilitate demolding. The use of low T_g thermoplastics as TOPAS is favored due to the lack of defects and the faster processing compared to hybrid PDMS stamps. The trenches patterned on the master stamp serves as protrusions on the soft-stamp to enhance polymer flow during the nanoimprint. The nanoimprint process with the soft stamp is illustrated in Fig.2.16 (c). Complementarily, we also show the cross-sectional front view in order to highlight the trenches at each fabrication step.

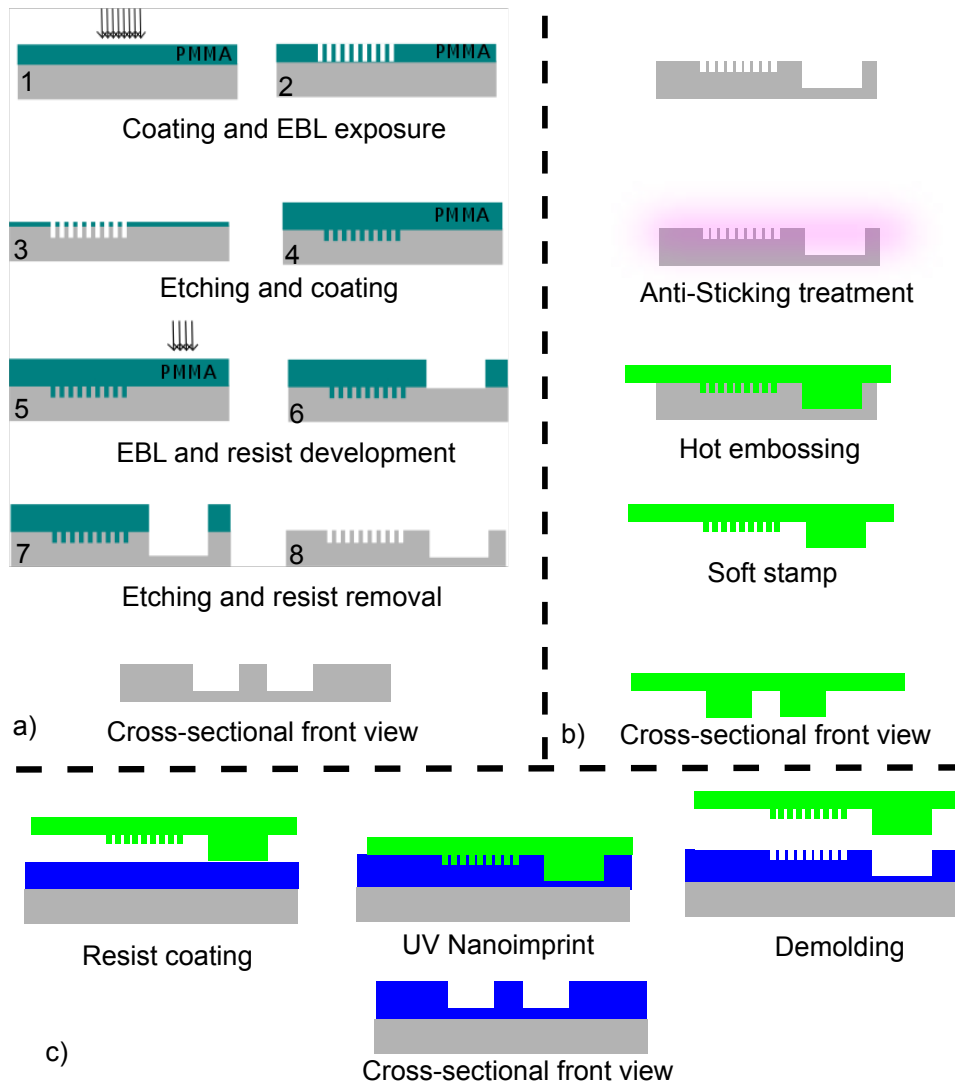


Figure 2.16: Complete overview of the desired process flow (a) Master stamp fabrication: Two height patterning of the master stamp with the same polarity as the final aimed device in polymer. (b) Intermediate soft stamp fabrication with the hot embossing of TOPAS. (c) Utilization of the intermediate soft stamp to replicate structures in polymer. All sketches are accompanied of the cross-sectional front view showing the trenches around the structures optimizing the squeeze of the polymer (MPSM).

2.4 Integrated photonic devices: Design considerations

Within this section we design the photonic structures proposed for the sensor operation. As shown in Ch.1.3 we must consider a diffractive element such a grating coupler, a polymer waveguide long enough to allow manual handling of microfluidic circuitry and an optical resonator based on ring structures. In parallel, we have shown that the drifts occurring during the fabrication processes can produce geometrical deviations in the fabricated structures. For example, grating grooves and period can shrink, waveguides can be not perfectly rectangular, or the residual layer underlying the rectangular waveguide present important inhomogeneities causing effective index variations along the waveguide. In addition, the mode will be partially confined into the slab waveguide (RL), increasing the propagation loss and affecting the quality factor of the resonator. Throughout this section we provide basic understanding of these structures studying the optimal dimension for correct operation. This study is supported with commercial mode solvers and FDTD simulation tools. The mode solvers are mainly used to calculate the waveguide cross-sections. The FDTD solvers are used to study both the grating coupler and the ring resonators.

A dielectric optical waveguide is composed of at least three layers of materials (including air) one of them with a higher refractive index than the surrounding layers. Therefore, this layer is know as waveguide core while the surrounding material are the cladding layers. The basic theory for optical waveguides can be found in general literature and it not will be addressed in this manuscript. As previously discussed, the main interest is using high index polymers to achieve enough index contrast (polymer-air) and to provide enough optical confinement. The index contrast is of main interest for the correct operation of the grating coupler since coupling efficiency depends on the index contrast of the periodic region. Also, waveguides benefit of a high index contrast with the surrounding medium providing high confinement and low bent losses, which is suitable for the major part of optical applications involving ring resonators. This may be not be of major importance for some optical sensors where a compromise between optical confinement and sensitivity should be found depending the sensing strategy. The optimum operation of the ring resonator is obtained with single mode waveguides; thus, the waveguide cross-section must be optimized to achieve single mode operation with the selected materials. This requirement is of main importance since single mode operation is needed to provide distinguishable resonances avoiding cross-talk between the different modes. Several parameters affect the mode number and the confinement of the optical waveguides such as waveguide dimension, refractive index and operation wavelength. In our case, the wavelength is determined by the final application ($\lambda=532$ nm) and the refractive index is given by the core material. However, we must also consider the variations of residual layer along the wafer, as mentioned, such geometrical variations can locally perturb the mode confinement resulting in large power loss or multi-mode operation within the ring resonator.

This section is divided into the different parts of the fabricated device. First, the mode operation of polymer waveguides is presented for different residual layers. The behavior of the grating couplers is studied varying the main parameters. In parallel, we verify the effective index of the fundamental mode with the well-know effective index method. A single diffraction order is chosen to couple the light inside the waveguides, this diffraction order will be chosen counter directionally to the propagation direction of the waveguide. The angle will be chosen to enhance the efficiency and to ensure that no parasitic light is being measured during the optical characterization. Finally we propose a design for the ring resonator studying the influence of the RL on the optical confinement.

2.4.1 Main considerations concerning the simulation tool

For the study of the optical devices, a commercial product from Lumerical Solutions Inc. is employed as the simulation tool for all grating couplers, waveguides and ring resonator in this thesis [104]. Several packages are included in Lumerical products, we use a MODE solver, 2D, 2.5D and 3D- FDTD packages to study the devices presented. The Finite Difference Eigenmode (FDE) solver (MODE) calculates the spatial profile and frequency dependence of modes from Maxwell's equations on a cross-sectional mesh of the waveguide. The solver calculates the mode field profiles, effective index, and loss. Finite-Difference-Time-Domain (FDTD) calculation is a straightforward physical basis since it is a numerical solution of Maxwell's equations. It can simulate electromagnetic interaction between the wave and a complex geometries proving accurate predictions which can be used for real photonic design.

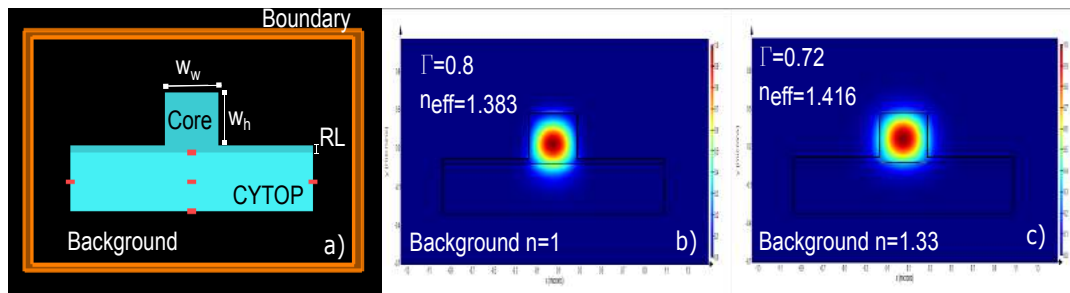


Figure 2.17: Overview of the waveguide cross-section in the MODE solver. Based on FDE calculations ($\lambda = 507$ nm) we are able to show the mode profile of the waveguide a) In this example: Waveguide width $W_w=450$ nm, $W_h=350$ nm, $RL=50$ nm, cladding layer (CYTOP $n = 1.34$) and PML as boundary condition. b) Resulting mode profile for air ($n = 1$) as background material ($n_{eff}=1.383$, $\Gamma=0.8$) c) Resulting mode profile with water ($n = 1.34$) background. ($n_{eff}=1.416$, $\Gamma=0.72$).

In the Fig.2.17 (a) we show the profile of a rectangular waveguide with a polymer core of NILUV394 ($1.52, \lambda = 500$ nm) onto a CYTOP cladding ($n = 1.33$) The waveguide width W_w , waveguide height W_h , the residual layer and the waveguide surrounding medium (background material) can be varied. We also show the mode

profile of a 450 nm x 350 nm polymer waveguide with an air cladding ($n = 1$) (Fig.2.17)(b) and a water cladding (Fig.2.17)(c) as surrounding medium. The effective index of the fundamental mode (n_{eff}) and the optical confinement factor (Γ) is shown in each figure respectively. Both results present a single mode waveguide operation at $\lambda = 507$ nm. When simulating optical structures, we must pay special attention to the boundary conditions applied to the simulation region. We can choose either PML (Perfectly matched layer) boundary conditions or metallic conditions (reflective boundary layer). PML absorbs incident electromagnetic (EM) waves with no reflection [105] while metal conditions reflect the outgoing waves. For very accurate calculations the PML conditions should be the preferred option because despite a higher calculation time it approaches more to the reality. Oppositely, metal boundaries are unrealistic boundaries, and the evanescent tails should be far from the boundary to avoid reflections. If this condition is fulfilled the resulting mode profile does not differ from the mode profile calculated with PML conditions. For example, no difference was found using metallic conditions and PML conditions for these geometries. We obtain $n_{eff} = 1.383$ and $n_{eff} = 1.416$ for Fig.2.17 (b) and Fig.2.17 (c) respectively. Besides the simulation time is reduced because we avoid the simulation between the absorbent PML layer and the wave. Although metallic structures can be effectively used, we should consider not to extend the structure through the metallic boundaries, the strong iteration between the boundaries and the EM field will create artifacts in the guided modes.

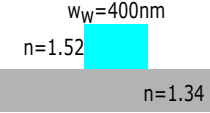
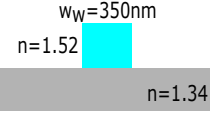
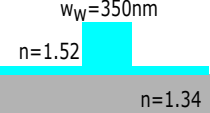
		n_{eff}	Lumerical	Yariv	C.Photo.eu	CAMFR
	$w_h=350\text{nm}$	TE0	1.447	1.447	1.447	1.447
	$h=500\text{nm}$	TM0	1.43	1.429	1.429	1.429
	$w_w=400\text{nm}$	TE0	1.352	1.348	1.346	1.351
	$h=500\text{nm}$	TM0	1.358	1.356	1.355	1.36
	$w_w=350\text{nm}$	TE0	1.336	1.325	1.322	1.329
	$h=500\text{nm}$	TM0	1.345	1.345	1.343	1.347
	$w_w=350\text{nm}$	TE0	1.351	-	1.339	-
	$RL=50\text{nm}$ $h=500\text{nm}$	TM0	1.363	-	1.357	-

Figure 2.18: Different effective index calculated analytically for the proposed waveguide geometries.

Complementarity, we have calculated similar waveguide structures analytically with different methods to study the convergence of the simulations with the analytical methods found in the literature [106]. In the Fig.2.18 we overview different results for the effective index calculated with different methods. As we can appreciate, all methods provide a similar result with no significant differences. The results

were obtained from different sources; the effective index method was used as proposed by Yariv [107] [108]. The effective index was also calculated with CAMFR [109] and an online mode solver ⁴

2.5 Polymer waveguides:

The geometry of the waveguide must allow single mode propagation. In order to do that we must study the effective index of the calculated mode for several geometries. The geometrical parameters considered in this work are the W_w , W_g and RL. This study can be done for different claddings. As the device will be intended for utilization with water, we must ensure single mode operation with both water and air cladding. If the single mode condition is fulfilled with an air cladding, the single mode condition will also be accomplished with a water cladding. This is due to the slight reduction of the RI contrast (core-cladding)⁵

2.5.1 Single mode operation

We propose to study the waveguide dimensions of the master stamp. In the Fig.2.19 we shown the variation of the waveguide geometry W_w , W_h for different RL with an air cladding. The wavelength of operation was fixed at $\lambda = 507$ nm for three residual layers ranging from 0 to 60nm.

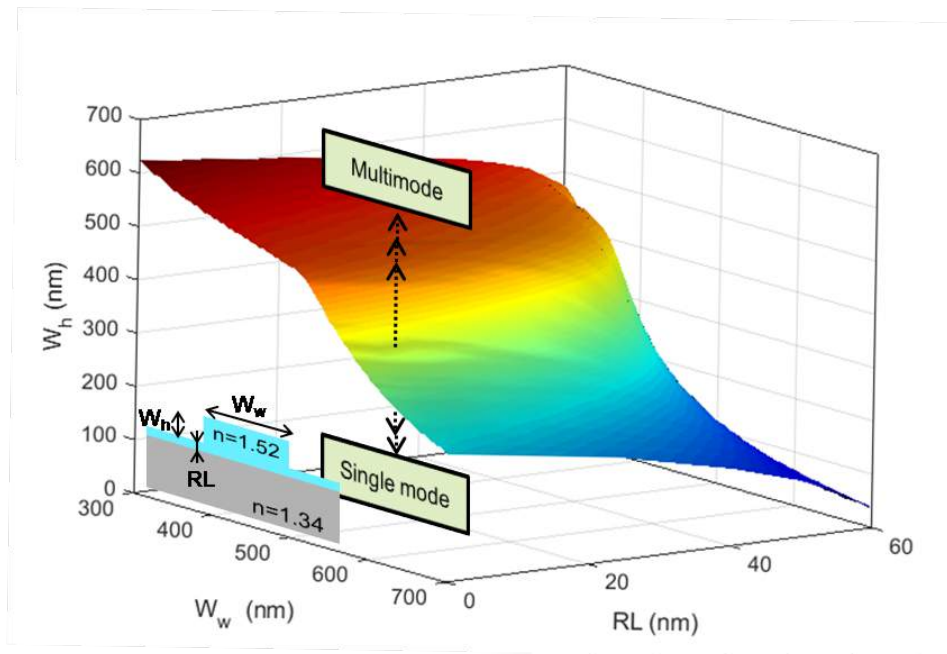


Figure 2.19: Geometrical variation of the waveguide parameters W_w , W_h and RL, The curve indicates the boundary conditions for single-mode propagation depending all the geometrical parameters.

⁴<https://www.computational-photonics.eu/oms.html>

⁵This is valid as a qualitative assumption, if the RI contrast is greatly reduced we can reach the cut-off condition for a fixed geometry. Complementary simulations sweeping the RI top cladding can be done to study refractive index limit for the top cladding.

The curve shows the limit between the single-mode (SMC) and multi-mode conditions (MMC). This limit is chosen from the n_{eff} obtained by calculation which must fulfill the condition $n_{core} > n_{eff} > 1.34(n_{cladd})$. As the RL layer increases the cross-section of the waveguide must be reduced overall to maintain single-mode condition.

As we can see when the RL becomes larger, the waveguide cross-section must be reduced to maintain single-mode operation. Oppositely, if there is no RL the waveguide geometry can be larger. Hereby, we must chose a geometry allowing SMC with a margin of error to include the fabrication variations which can occur during the fabrication process (EBL, etch, nanoimprint). Thus, we expect a RL lower than 100 nm; therefore 350 nm x 350 nm waveguide cross-section allows single-mode condition. Further simulations are related to the waveguide bandwidth and the slab waveguide height for a fixed cross-section.

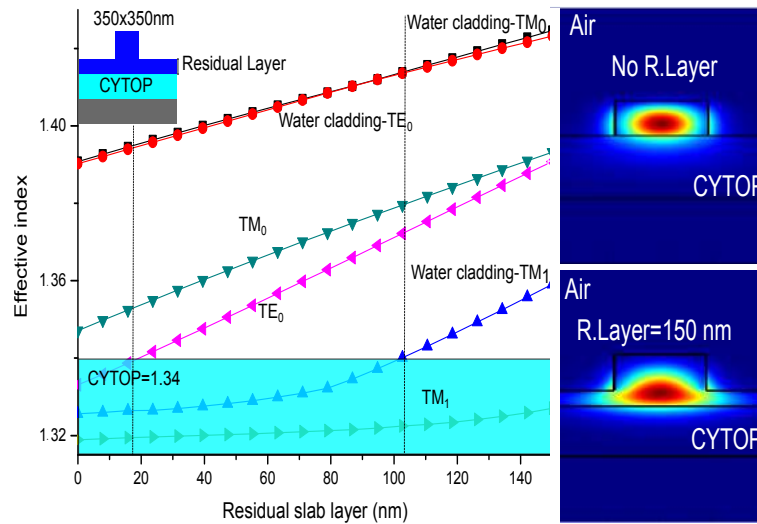


Figure 2.20: Effective index waveguide variations depending on the thickness of the RL. Simulations have been performed with LUMERICAL@MODE SOLVER package. The inset shows how the TE mode profile spreads out into a 150 nm thick RL compared to the mode profile without any RL.

A $1.5\mu\text{m} \times 1.5\mu\text{m}$ simulation region, larger than the physical dimensions of the waveguide, was selected as well as reflective layers for the transversal boundary conditions. The MODE solver is used to study the spatial variations of the mode profile depending on the RL thickness. The simulation results are displayed in Fig.2.20. In the case of air cladding, a RL thickness over 18 nm enables single-mode propagation of the TE-like mode while below this value, only the fundamental TM-like mode can propagate. For water top cladding, a multi-mode propagation is demonstrated over a 110 nm thick RL. Therefore, assuming a homogeneous RL on the wafer is of major importance since large RL variations lead to wide effective index changes that can affect the properties of the mode propagation. The inset of Fig.2.20 shows the TE mode profile distribution with and without a 150 nm thick RL. When the RL increases the lateral confinement is affected and the mode clearly spreads out in the

slab region. As RL becomes larger the effective index for the mode increases as it interacts more with the core material; however this does not mean that the mode is more confined. (less lateral confinement).

2.5.2 Waveguide bandwidth

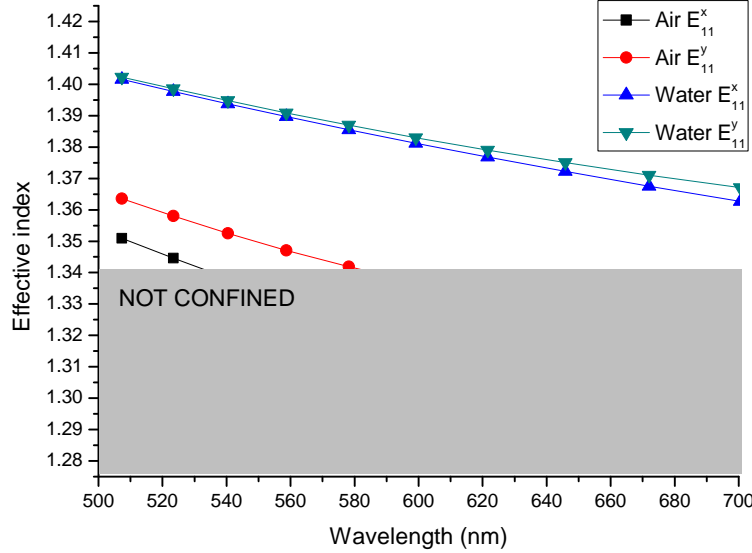


Figure 2.21: Wavelength dependence of the effective indices of rib-like waveguides 350 nm x 350 nm onto a minimal RL of 50 nm. Water and air cladding are set up as top cladding.

The Fig.2.21 shows the dispersion diagram for 350nm x 350nm waveguides with a minimal RL of 50 nm. We have studied the dispersion of the fundamental modes at visible wavelength (500 nm-700 nm) for both water and air cladding for future operation in liquid media. The notations of the modes were taken from [110] where E_y , E_x represents respectively the TM-like and TE-like fundamental modes. Compared to air cladding, water cladding allows for small effective index differences between TE-TM modes. The difference is more important when the index contrast is increased (air cladding). Broadband transmission at visible wavelength is therefore allowed with symmetric water cladding waveguides. Single mode condition is accomplished for the green region of the visible spectrum for waveguides with air claddings.

2.6 Grating coupler

Grating couplers embedded in optical waveguides can achieve light coupling from the air to the chip. In this section, we review the fundamental equation of the grating coupler. Then, we study the coupling depending on grating parameters. Grating couplers are periodic structures with the period Λ comparable to the wavelength of the incident light. To introduce the mathematical description, we consider a simple periodic structure as show Fig 2.22.

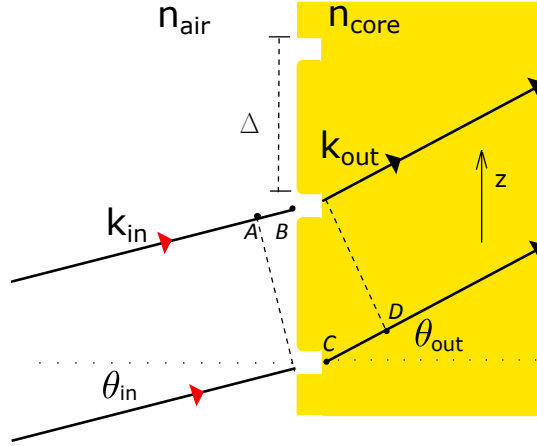


Figure 2.22: Periodic structure

We can write the phase mismatch ϕ in function of the optical path difference $[AD]$ and the wavevector k_0 as follows:

$$\phi = k_0[AD] = k_0([AB] - [CD]) \quad (2.1)$$

With the the optical path and imposing constructive interference between two adjacent beams we can write:

$$\frac{2\pi}{\Lambda}q = k_{in}\sin\theta_{in} - k_{out}\sin\theta_{out} \quad (2.2)$$

Where $K = 2\pi/\Lambda$ is the phase constant of the grating. The equation can be written along the z direction

$$qK = k_{z,in} - k_{z,out} \quad (2.3)$$

This equation is usually found as grating coupler equation. Where $k_{z,out}$ and $k_{z,in}$ are the output and input wavevectors, K is the grating wavenumber or reciprocal wave vector. If the input coupling is performed from the air, the transmitted wave follows the grating equation as:

$$n_{core}\sin(\theta_{out}) = \sin(\theta_{in}) - q\lambda/\Lambda \quad (2.4)$$

Depending on the phase constant of the grating, the incident beam is separated in several q harmonics as shown in Fig.2.23. These harmonics have a different phase constant than the input wave. The diffracted waves with the same phase constant than the waveguide modes are coupled into the waveguide. Several q waves can appear, but the location of the $q = 0$ order is always found at an angle equal and opposite to the incident angle. If we fix the incident angle to normal incidence $\sin(\theta_{in}) = 0$, as $q=\pm 1, \pm 2, \dots$ we can extract the number of modes for an operation wavelength and a period as follows:

$$n_{core}\sin(\theta_{out})\Lambda/\lambda \leq q \quad (2.5)$$

The number of modes increases with a large Λ or a short λ . If we consider an incident angle θ_{in} , the number of modes is determined imposing the condition $-1 < \sin(\theta_{out}) < 1$. It can be written as follows:

$$\Lambda/\lambda(\sin(\theta_{in}) - n_{core}) \leq q \leq \Lambda/\lambda(\sin(\theta_{in}) + n_{core}) \quad (2.6)$$

The term on the left is negative as $n_{eff} > \sin(\theta_{in})$. Similarly, the term on the right stands for the positive values.

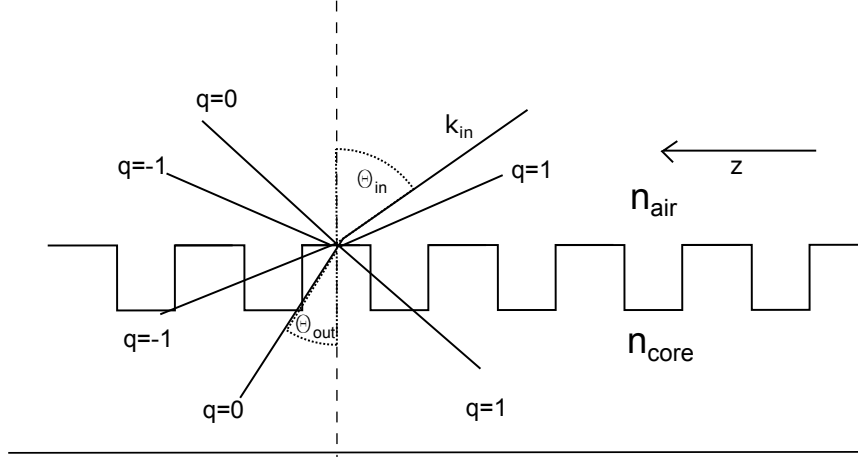


Figure 2.23: (a) Grating interface showing both transmitted and reflected waves of order q with an incident angle.

2.6.1 Effect of the period on the effective index

Depending on the values of the grating equation two coupling regimes can be obtained, co-propagative where the coupled mode stands in the same sense as the incident wave and counter-propagative where the coupled wave propagate in the opposite direction to the incident wave. If we consider a guided mode with an effective index : $n_{eff} = n_{core}\sin(\theta_{out})$ the equation Eq.2.4 can be written as:

$$n_{eff} = \sin(\theta_{in}) - q\lambda/\Lambda \quad (2.7)$$

As an example, we chose the stack of materials selected in this work (NILUV/CYTOP/SI with RI 1.52/1.34/4). Multiple parameters can be chosen, in this case, we for simplicity we chose to plot the effective index of one single diffraction order ($q=-1$). The wavelength is set to 507 nm and $\theta_{in} = -20^\circ$. The values of the effective index allowed by this grating configuration are represented by the colored regions in the Fig.2.24. Guided modes are allowed when the effective index is comprised between $n_{clad} < n_{eff} < n_{core}$. When the effective index is comprised between $n_{clad} < n_{eff} < n_{air}$ the light will be coupled to the cladding. For periods smaller than 270 nm or larger than 380 nm most of the light will be coupled to the substrate or the air (radiated) respectively. This result is valid for the parameters stated for this example. Therefore a grating coupler with a period Λ comprised between 270 nm and

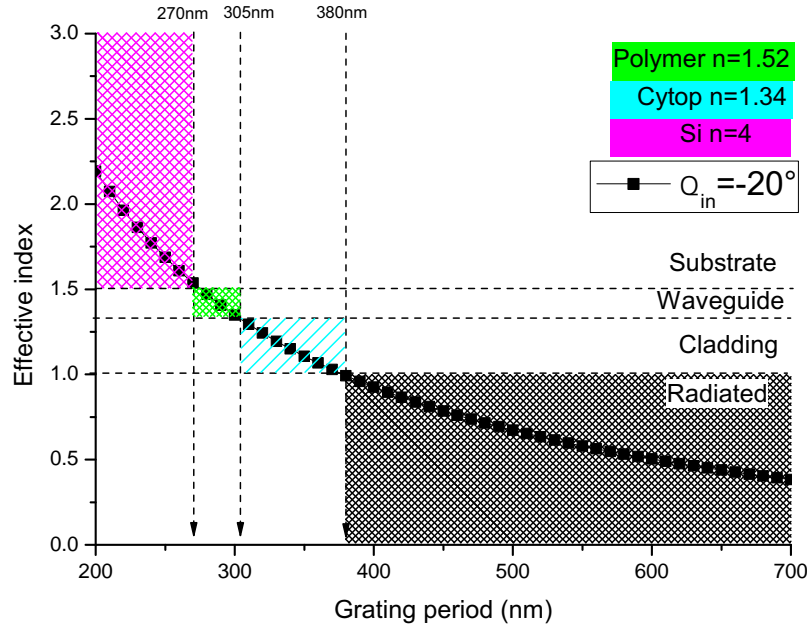


Figure 2.24: Plot of the effective index versus grating period ($q=-1$, $\theta_{in}=-20^\circ$, $\lambda = 507 \text{ nm}$). For the stack of materials presented here (NILUV/CYTOP/Si).

305nm allows for light coupled at this input angle regardless fabrication variations affecting the effective index. More positive values of the input angle shift the curve towards higher effective index.

2.6.2 Effect of the input angle on the effective index

We can study how the input angle tunes the effective index. For example, we select two different periods 290 nm and 425 nm, for a grating coupler operating at $\lambda = 507 \text{ nm}$ with the same material configuration (NILUV/CYTOP/SI with $n = 1.52/1.34/4$). In the figure 2.25 we plot the grating coupler equation for two different periods. By selecting a short period of 290 nm the first diffraction order can be coupled to the waveguide (black) for coupling angles (or diffraction angles) comprised between the limits established by the refractive index of the core and cladding. The second diffraction order (red) for this period cannot be guided into the waveguide as far as the diffracted wave cannot reach the required effective index. If a larger period is chosen (425 nm) the first diffraction order can be used for co-propagative coupling (green). The second diffraction order (blue) also allows for light coupling (or diffraction) around 80° .

The coupling angles are reciprocal either if input or output coupling configuration is selected. Since we can only perform the coupling with a single incident beam, the additional (second) diffraction order will reduce the coupling efficiency overall. Thus the total efficiency is split between the different diffraction orders. Similarly, if a guided mode encounters the corrugated region of the grating the power will

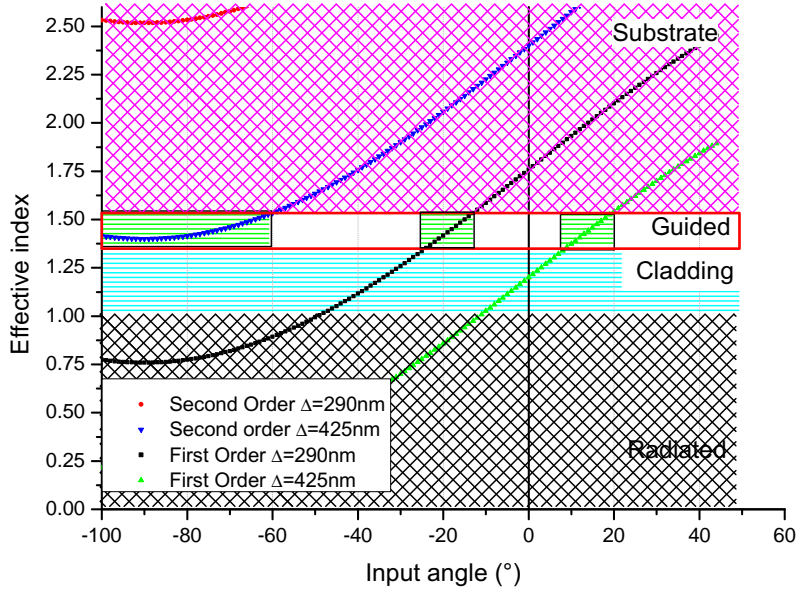


Figure 2.25: Plot of the effective index versus the input angle. Allowed and forbidden regions are plot depending the effective index.

be split between the allowed diffraction orders for that geometry. Further simulations to calculate the power coupled to each diffraction angle are out of the scope of this work. Within this manuscript, we try to use single diffraction order at counter propagative angles to enhance the efficiency and reduce parasitic reflexion of unwanted diffraction orders. A guided wave propagates into the waveguide, then it encounters the corrugated region and the guided wave is diffracted (coupled out). In the following we present the optimization of the grating parameters considering the output coupler configuration.

2.6.3 Calculation of the diffraction angle

In order to calculate the diffraction angle we can use a first approach to estimate the effective index of the grating. The effective index of the corrugated region can be approximated as an average between the effective index of the slab waveguide and the grooves. The effective index for a slab-like waveguide ($h=400$ nm, $n=1.52$) is $n_{eff1} = 1.45$ approximately. If we choose a grating with an etch depth of $h/2 - h/3$ we can for example calculate an effective index for the etched slab waveguide $n_{eff2} = 1.41$. The waveguide of $h = 400$ nm with a etch depth of $h_d=150$ nm (slab height= 250 nm) presents a periodic combination of two fundamental effective index ($n_{eff1} = 1.45$, $n_{eff2} = 1.41$). We can calculate the effective index of the grating as the average of effective index in both regions.

$$n_{eff.g} = n_{eff2}(1 - F) + n_{eff1}F \quad (2.8)$$

We define fill-factor (or duty cycle) as the region of the grating period that allows passing the light through. Therefore for the stated values the $n_{eff.g} = 1.43$ and $\Delta = 290$ nm would give approximately a diffraction angle of 19° . This calculation

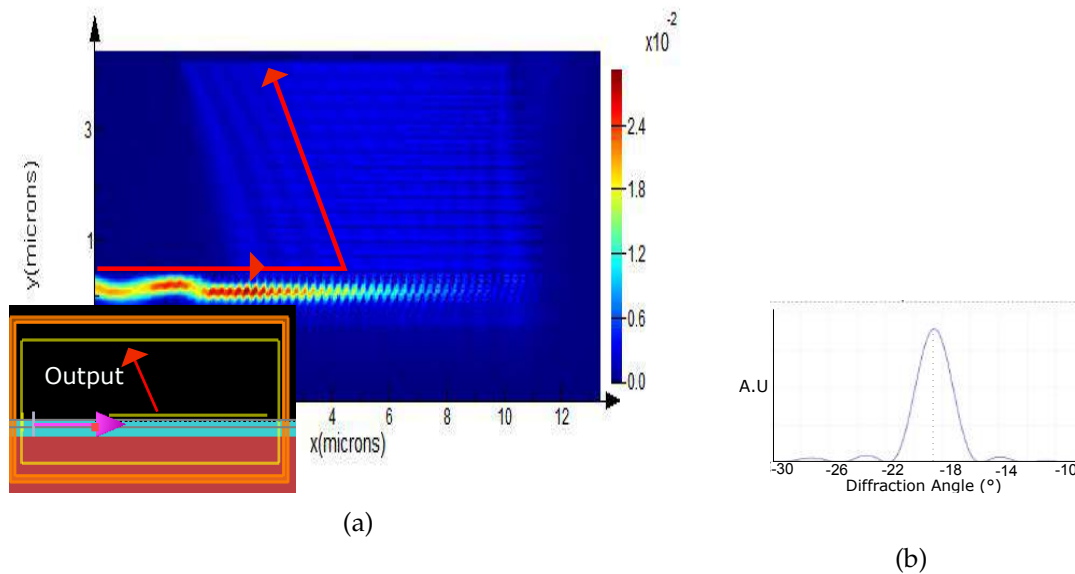


Figure 2.26: a) Color-map of the proposed grating coupler ($\Lambda = 290nm$) profile during diffraction. The inset shows the propagation direction of the guided wave b) Calculated diffraction angle with the FDTD solver showing a peak at -19° .

is supported by the simulation shown in Fig.2.26. In Fig.2.26 (a) we show the color-map of the single diffraction angle at -19° . In Fig.2.26 (b) we show the calculated diffraction angle at -19° . The shape of the diffraction peak is a *sinc* function which is the typical diffraction pattern by a rectangular grating. This shape is related to the shape and depth of the grating. Other diffraction functions are possible as detailed in [111]. As the grating coupler is a reciprocal system, the same behavior can be expected if the grating is used as input coupler.

2.6.4 Etch depth

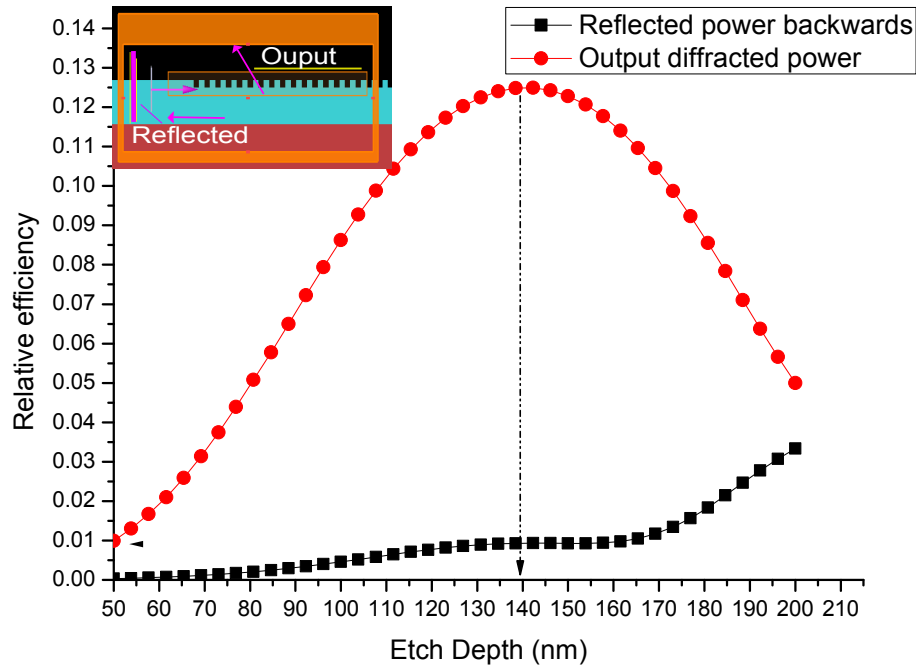


Figure 2.27: Etch depth optimization. The figure shows the reflected power backwards and the optimal etch depth for the proposed grating coupler ($\Delta = 290\text{nm}$, $\lambda = 507\text{nm}$). The inset shows a capture of the LUMERICAL software to calculate the transmitted and reflected power.

As stated before, the variations on the groove fill factor and dimensions during fabrication can produce deviations of the angle of diffraction from the predicted value. The main effect of the grating parameters variation can be reviewed in the theory [112]. Therefore, we propose to quantify the main deviations depending on the grating coupler fabrication parameters.

The Fig.2.27 shows the optimization of the etch depth for a given grating period, material and operation wavelength. The grating is set to operate as an output coupler. A mode propagating into the waveguide suddenly encounters the diffraction grating. Then, depending the etch depth, a ration of the the guided power will be redirected (diffracted) outwards but, also some part of the propagating light will be redirected backwards to the waveguide. Achieving high efficiency is important, however we must minimize backward reflexion against the set-up and to the waveguide. Backward reflections to the laser or to the waveguides can produce undesirable interferences thus they must be minimized. For this purpose we propose a grating etch depth of around 140 nm which represents the best trade off between efficiency and reflected power. This depth will be etched on the master stamp. The deviations of the diffraction angle with the etch depth are shown in Fig.2.28. As the structures are shallowed etched the detuning of the diffraction angle due to etch depth variations are small compared to the detuning suffered by structures with higher refractive index contrast. The angular detuning regarding the etch depth is defined

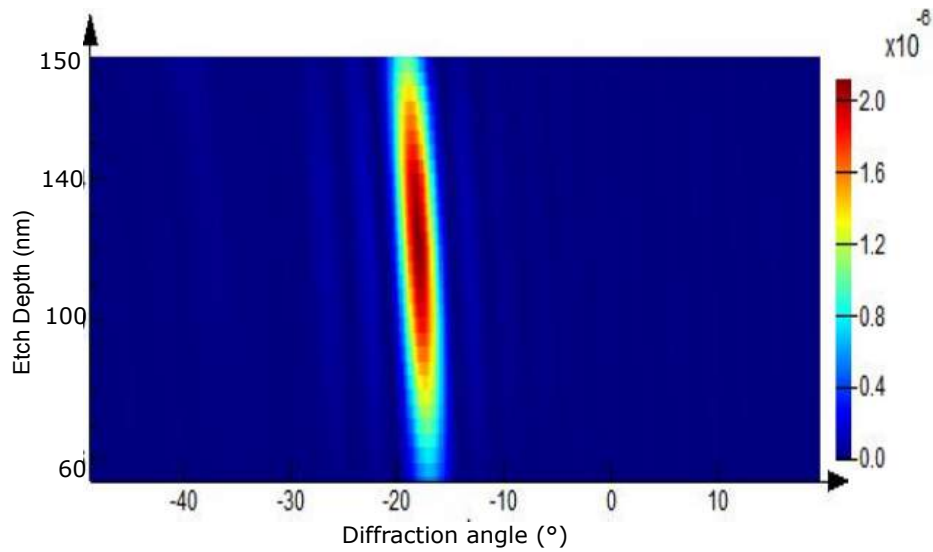


Figure 2.28: The angle of diffraction slightly changes when the etch depth is modified. The detuning is extracted from the simulation and it is around $0.0225^\circ/\text{nm}$.

as Δ°/nm . The detuning extracted from the simulation is $0.0225^\circ/\text{nm}$. As we can appreciate, the diffracted angle becomes more negative as the etch depth increases since it implies a reduction of the n_{effg} calculated by the average effective index.

2.6.5 Duty Cycle variation

The duty cycle DC or fill factor variation can also be affected by the fabrication process since during EBL patterning dose, energy or development resist variation can give different groove width. Despite the fabrication process must be optimal we must study if the obtained device is optimal for the expected operation. In the Fig.2.29 we shown the variation of the diffraction angle when the duty cycle is swept from 0.2 to 0.9. Diffraction gratings with fill factor being half of the period are more common since it gives optimal efficiency, but other relationships between period and fill factor are possible [113].

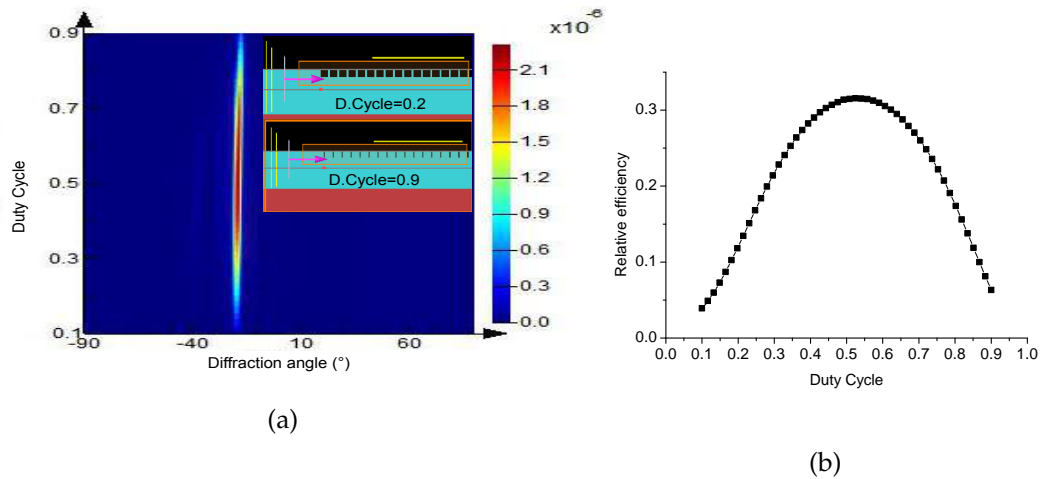


Figure 2.29: The angle of diffraction slightly changes when the duty cycle is modified. The detuning is extracted from the simulation and it is around 2.2° when the duty cycle changes from 0.1 to 0.9. Therefore the detuning is $2.75^\circ / \Delta DC$. The inset shows the different duty cycle displayed in the software. b) The optimum duty cycle is found around $DC=0.5$.

The angular detuning regarding the duty cycle is directly extracted from simulation. The diffracted angle becomes more positive as the duty cycle increases since it implies an increase of the n_{effg} .

2.6.6 Influence of the RL

The duty cycle and the etch depth may have an influence on both grating efficiency and diffraction angle. These parameters depend on the EBL parameters and can be optimized. However, RL thickness homogeneity mostly depends on the imprinting process. As discussed before, different cavities present different sinking velocities and thus, locally different residual layer since variations of the coupling angle can be attributed to RL variation. Typically the measure of the diffraction angle is a non-destructive method to quantify the residual layer during a nanoimprinting process [114] [115].

The Fig.2.30 shows the variation of the angle of diffraction with the residual layer. The residual layer acts as the slab height of a rib waveguide increasing the effective index of the waveguide mode. Therefore, when the RL increases the diffraction angle becomes larger (less negative). For a fixed rectangular waveguide geometry $350\text{nm} \times 350\text{nm}$, the diffraction angle changes from 19.85° to 17.77° for a RL ranging between zero and 100 nm. Thus, the angular detuning in this case is $0.021^\circ / \text{nm}$.

2.6.7 Fabrication tolerances and proposed design

In the Tab.2.2 we show the benchmark for the waveguide and the grating coupler. The fabrication tolerances and variations are discussed from the experience with the patterning facilities. The devices will be fabricated with curable polymer. UVNIL

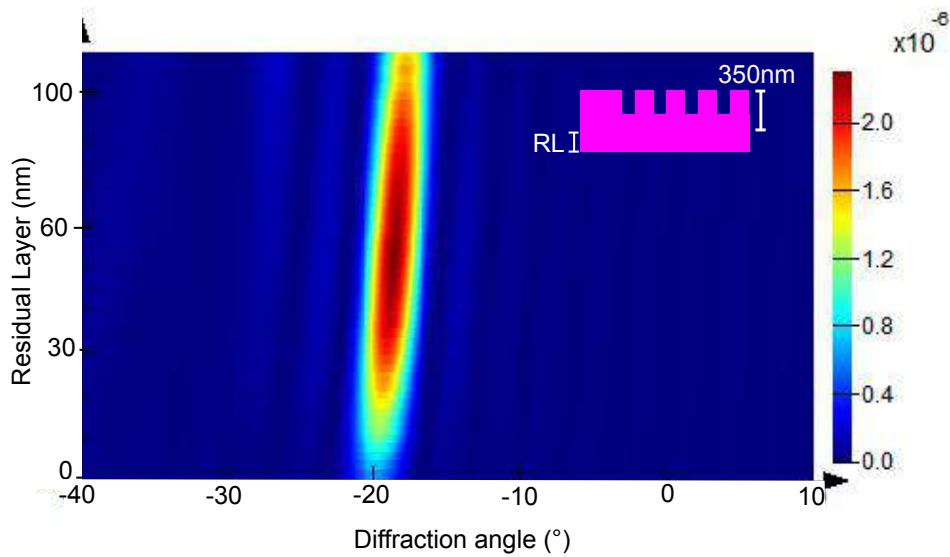


Figure 2.30: The diffraction angle of a 350 nm height waveguide slightly changes when the RL is modified. The detuning is extracted from the simulation and it is around $0.02^\circ/\text{nm}$ when the RL increases from 0nm to 100nm. The inset shows transversal cross-section of a grating with a period of $\Delta = 290$ nm.

was used at the beginning with a green laser for testing at 507 nm. Complementarity, some devices will be imprinted with ORMOCore and tested with other green laser emitting at $\lambda = 532$ nm. The waveguide patterned by EBL on the master stamp will present a cross-section of 350 nm x 350 nm. This stamp will be used to imprint the structures on 400 nm of resist. A thin residual layer around 50nm will be enough to guarantee the correct replication of the devices while maintaining single-mode operation as shown in Fig.2.20. The dimensions for the grating coupler are given considering the optimal efficiency for a single diffraction order (counter-propagative). The devices are transferred to the master stamp with EBL and RIE. EBL patterning will not present significant drifts on the waveguide width. Contrarily, the duty cycle is greatly affected by the EBL process but even a 10% (0.5 ± 0.1) of variation will provides good transmission performances. The etch depth is mainly controlled by RIE process, up to 20% of variation on the etch depth can be accepted without affecting the diffraction angle grating coupler. An estimation of the RL tolerance is very complex to obtain because it depends on the concrete design of the master stamp. However, obtaining less than 10% of variation seem reasonable for a RL=50nm. Another nanoimprint variation will come from the shrink of the thermoplastic which is approximately 0.6%.

The global view of the waveguide with the grating coupler is shown in Fig.2.31. We show a tapered waveguide (adiabatic mode converter) of 4mm including the grating coupler. This important length facilitates simultaneously the future integration of microfluidic circuitry and the handling of future packaged microsystems.

Table 2.2: Input data for waveguide and grating.

Waveguide	Parameter	Other
Material	NILUV394 (1.52)	ORMOcore (1.56)
Waveguide Layer	400nm	-
W_h	350nm	-
W_w	350nm	-
Wavelength	507nm	532nm
Grating	Dimension	Detuning
Period	290nm	-
Etch Depth	150nm	$0.0225^\circ/\text{nm}$
Duty Cycle	0.5	$2.75^\circ/\Delta DC$
R.Layer	50nm	$0.02^\circ/\text{nm}$
Fabrication variations	EBL & RIE	Nanoimprint
Period	-	0.6%
W_w	2%	0.6%
W_h	5%	0.6%
Duty Cycle	10%	-
Etch Depth	20%	-
R.Layer	-	10%

The length of the taper is considered infinite regarding the grating size and the operation wavelength, therefore the simulations for the adiabatic mode converted are not shown in this work. Due to the small taper angle (0.4°) the losses due to the adiabatic mode conversion are neglected. The grating coupler area is over-sized to $35\mu\text{m}\times 35\mu\text{m}$.

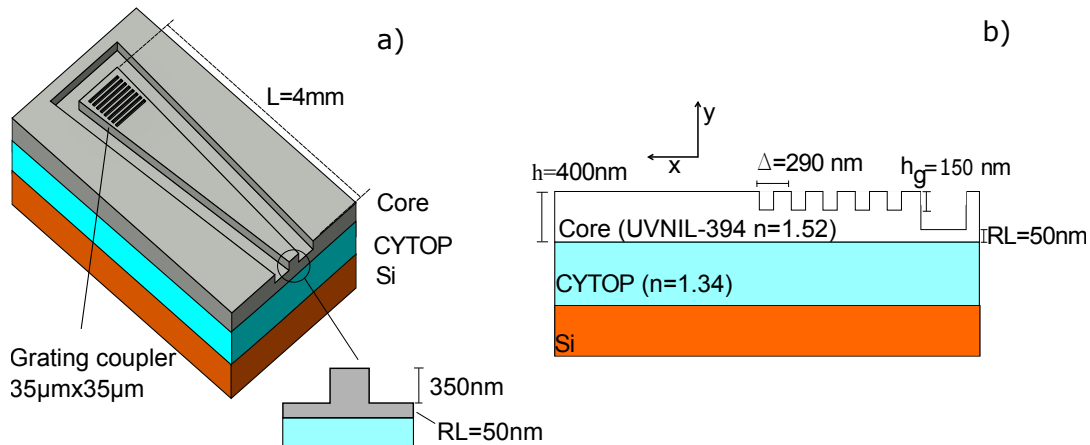


Figure 2.31: a) Design of the tapered waveguide and the grating coupler. b) Cross-section view of the 3D structure showing the height of the waveguide layer $h=400\text{nm}$ corresponding to the waveguide height (350nm) with 50nm of RL. The grating depth (h_g) is set to 150nm.

These dimensions were chosen to allow all the light to be radiated from the waveguide and ease the beam alignment during characterization. Further works

can be done studying the coupling strength of the grating in order to adapt the input beam to the coupling length of the grating to further enhance the efficiency.

2.7 Ring resonators: Main parameters

Integrated optical ring resonators are waveguide based devices used to provide high optical Q factors in photonic circuits. In this manuscript we devote a chapter/section towards the utilization of the ring resonator as optical micro spectrometers. Therefore in this section we review the main parameters affecting the ring resonator. The theory underlying the operation of the ring resonator can be found in literature [116]. In this work we focus on the simplest design of a ring resonator, a Notch filter, which consists in a straight waveguide and a ring waveguide. This is shown in the Fig.2.32. The auto-coupling factor r is the fraction of power remaining in the waveguide, a is the round trip loss and k the power coupled into the waveguide. If we assume no coupling losses the split factors are related by $k^2 + r^2 = 1$. The propagation loss includes all loss mechanism $a^2 = e^{-\alpha L}$ and the absorption coefficient α . The losses are cumulated all the round trip of the ring length L . The waveguides are placed

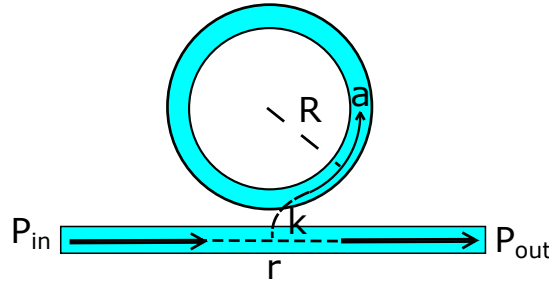


Figure 2.32: ALL-pass (Notch filter) ring resonator.

close to each other, making the light affect each between the two structures. If the propagation length around the ring is an integer number of wavelengths m , the field becomes resonant and a strong field builds up in the ring. This condition can be written as follows:

$$2\pi R n_{eff} = m \lambda_{res} \quad (2.9)$$

Where R is the ring radius and λ_{res} is the resonant wavelength. After propagation around the ring waveguide, some light couples back to the straight waveguide and interferes with the incident light. At resonance, completely destructive interference can be obtained, with no transmitted light. This makes the optical ring resonator an ideal Notch filter, blocking the light at the resonant wavelength. Two important parameters defining the ring resonator are the transmission and the free-spectral range. The transmission is the ratio between the input and the output power, it can be written as:

$$T(\lambda) = \frac{P_{out}(\lambda)}{P_{in}} = \frac{a^2 - 2r a \cos(\phi) + r^2}{(1 - 2r a \cos(\phi) + (ar)^2)} \quad (2.10)$$

Where $\phi = \omega n_{eff}L/c$ is the phase shift. The power transmission spectrum has dips at resonance frequencies f determined by:

$$\phi = 2m\pi = 2\pi n_{eff}L/\lambda \quad (2.11)$$

where the ratio or dip resonance periodicity is the FSR= $c/(n_{eff}L)$

The power at resonance $\phi = 2m\pi$ can be rewritten:

$$T(\lambda_{res}) = \frac{P_{out}(\lambda_{res})}{P_{in}} = \frac{(r - a)^2}{(1 - ra)^2} \quad (2.12)$$

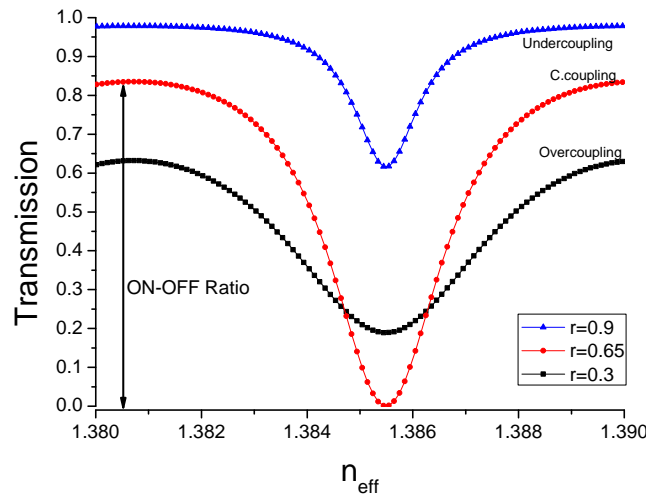


Figure 2.33: All-pass (Notch filter) ring resonator transmission showing different coupling configurations with $a = 0.65$.

Depending on r and a , several configurations can be distinguished. There are three coupling regimes.

- $a = r$: The critical coupling occurs and in this case, no light is transmitted through the waveguide. Light that enters the ring has the same magnitude with 180° phase shift since the light being coupled out of the ring and all the light is lost into the ring. In this case, the intensity build-up of the ring is the highest. The ON-OFF ratio or power contrast between the on and off resonance is maximum at this point.
- $r > a$: Such a regime is called “under-coupled”. The amount of light that couples out of the ring, back into the waveguide, is not of a sufficiently high intensity to completely interfere in a destructive way with the light that passes the ring and transmitted through the waveguide. Therefore, the intensity in the ring is lower compared to the previous regime.
- $a > r$: Such a regime is called “over-coupled”. Most of the light is coupled out of the ring, into the waveguide. When this happens, the light makes fewer

round trips inside the ring. As a result, a larger range of wavelengths can couple into the ring due to the shorter coupling distance.

These coupling regimes are tuned by the distance between the straight waveguide and the waveguide ring, this separation is called the gap. The confinement of the mode inside the straight waveguide will also influence the optimal distance to obtain critical coupling. As example in the Fig.2.33 we show transmission of a single-coupled ring resonator for different coupling regimes. The ON-OFF ratio in the case of $a = r = 0.65$ (critical coupling) is larger compared to the under-coupling and over-coupling regimes, in this case the power at resonance drops to zero. Destructive interference occurs between the light traveling inside the ring and in the waveguide. In the case of overcoupling the transmission does not vanish at resonance. A decrease a means a larger attenuation loss with a spectral dip larger than in the case of critical coupling. If the propagation loss increases the transmission decreases (Decreasing ON-OFF ratio). In the case of undercoupling, the resonances are sharper than in critical coupling however, the transmitted power neither vanishes at resonance. Further increase of the propagation loss will decrease the transmission at resonance (Larger ON-OFF Ratio).

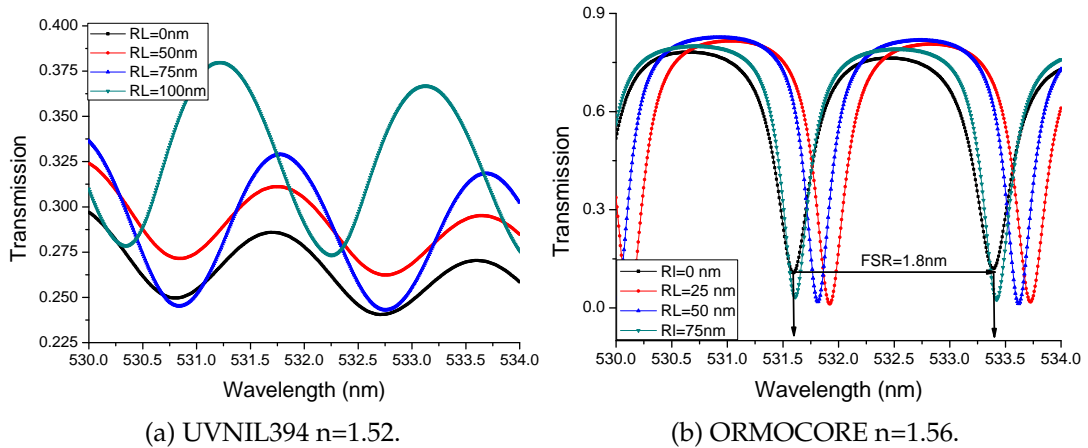


Figure 2.34: Transmission of 350x350nm ring resonator waveguide for two different polymers with $R=15\mu m$. The RL is modified affecting the transmission of the ring. The quality factor $Q \approx 1700$.

The coupling behavior of the ring resonator will be of main importance in this work not only to understand the influence of the RL, but also to understand how an increment in the loss affects the coupling regime. In order to study the influence of the RL we present 3D-FDTD simulations of the ring resonator. 3D-FDTD simulations are powerful tools to calculate the propagation of the EM field. However, it is very time consuming and the dimension of large structure will exponentially increase the simulation time. We have simulated ring resonators for the proposed waveguides with $R = 15\mu m$. In a first step, this radius has been chosen to have a short FSR of few nanometers (2nm). Also it will provide accurate results with 3D-FDTD in a reasonable amount of time. Two ring resonators with the same geometry were

simulated for two different polymer materials: UVNIL394 and ORMOCORE (1.56) with a fixed gap of 100nm. We have set an air cladding ($n=1$).

The Fig.2.34 shows the transmission of two ring resonators for two different polymers the UVNIL394 ($n=1.52$) and ORMOCORE which has a higher refractive index ($n=1.56$). For a given $R = 15\mu m$ the ring resonator made of UVNIL (Fig.2.34 (a)) do not provide sharp resonances as the ring made of ORMOCORE (Fig.2.34). This is due to the higher refractive index of the ORMOCORE which provides higher confinement and therefore reduced bending losses. In the same way, the variation of the RL affects more the UVNIL394 ring than the ORMOCORE ring for the same device geometry. As we shown in Sec.2.5 the increase of RL reduces the lateral confinement spreading the mode in the slab layer. This implies an increment of the bending losses which is translated in broader resonance dips. In the Fig.2.34 none of the plots shows critical coupling since the transmitted power does not fall to zero. We observe a larger ON-OFF ratio when the RL is increased, if the ON-OFF ratio increases at the same time that losses do we are working with an over-coupled resonator. However, in this particular case not only the loss raises, there is also an increment in the coupling factor due to the larger RL. The final coupling configuration of the ring will be influenced by the competition between the both rising coupling factor and losses. It means that if RL increases r diminishes and a also does, therefore the resonance dip will be enlarged at the same time as the ON-OFF ratio.

The same configuration was tested by the ORMOCORE, however in this case we are close to the critical coupling compared to the UVNIL ring for the same geometries. The resonances are sharper and the light is more confined due to the higher refractive index than the UVNIL. The effects depicted above about the RL are less obvious as we are already almost at critical resonance. As we can see, when increasing RL from 0 to 25nm the ON-OFF ratio increases being at almost critical coupling for $RL=25nm$, which means that we were slightly over-coupled. Further increment in the RL seems to switch the behavior and reduce the ON-OFF ratio, therefore, at this point, it seems that the losses become dominant over the coupling factor.

The influence of the residual layer in the behavior of the ring resonator can increase the losses but it can also increase the coupling factor, due to the competitiveness of both parameters. However this is determined by the geometry of the waveguide and the material combination. Despite the difficulty of the experimental verification of these figures, they are extremely meaningful. We can explain why an imprinted device with a larger RL can show both larger ON-OFF ratio and resonance dip, which can be counterintuitive during the optical testing of both devices.

2.8 Sensor architecture

2.8.1 Sensing strategies

Commonly, two main sensing strategies can be found in literature [117], homogeneous sensing and surface sensing. In homogeneous sensing the cladding index is modified leading to an overall effective index variation. Oppositely, surface sensing involves functionalized surfaces with dedicated binding elements improving the specificity of homogeneous sensing techniques. In both cases, the main sensing strategy relies on a shift on the resonant wavelength due to the effective index modification of the ring resonator waveguide. Optical spectrum analyzers or high resolution spectrometers are required to detect such a shift enabling to extract the analyte concentration. Alternatively, the sensor measurement reference can be performed in presence of water top cladding by simply matching the ring resonance and the laser wavelength. Then, once the analyte is added to the liquid cladding, the shift of the resonance can be directly correlated to an output power variation. Hence, the analyte concentration can be determined measuring only the power variation collected by an appropriated photodiode.

By this way, absorption sensing using microring resonators and photodiodes has been also demonstrated [118]. In this case, specificity of the sensor can be obtained externally with colorimetric chemistry and wavelength-tunable short-linewidth lasers. The measured power variation can be related to the absorption coefficient and thus, the concentration of the analyte. Although spectrum analyzers with tunable lasers would provide broadband sensing, integrated systems allowing on-site deployment would benefit of direct power measurement via on-chip photodiodes. Indeed, from the end-user's point of view, although that sensitivity and specificity are key parameters, portability, regeneration, response time and long-term reliability are also crucial issues but are often relegated to a lower priority in the research and development steps, despite outstanding degree of innovation of the sensing part.

2.8.2 Proposed structure and detection principle

In order to show and support the sensing strategy, FDTD simulations of single coupled ring resonator structures have been performed. The polymer structure is shown in Fig.2.35a. For the waveguide core, high polymer index can be selected, for example some commercial UV curable polymers present relative high refractive index (1.55-1.56 $\lambda = 532nm$). In this work, we have chosen a refractive index of $n_f=1.56$. The dimension of the waveguides are 350nmx350nm ensuring single mode operation at visible wavelength ($\lambda = 532nm$). The mode profile is depicted in Fig.2.35 showing an effective index of 1.40 and power confinement factor of $\Delta = 0.65$. The bottom cladding is chosen to match the refractive index of water which will act as

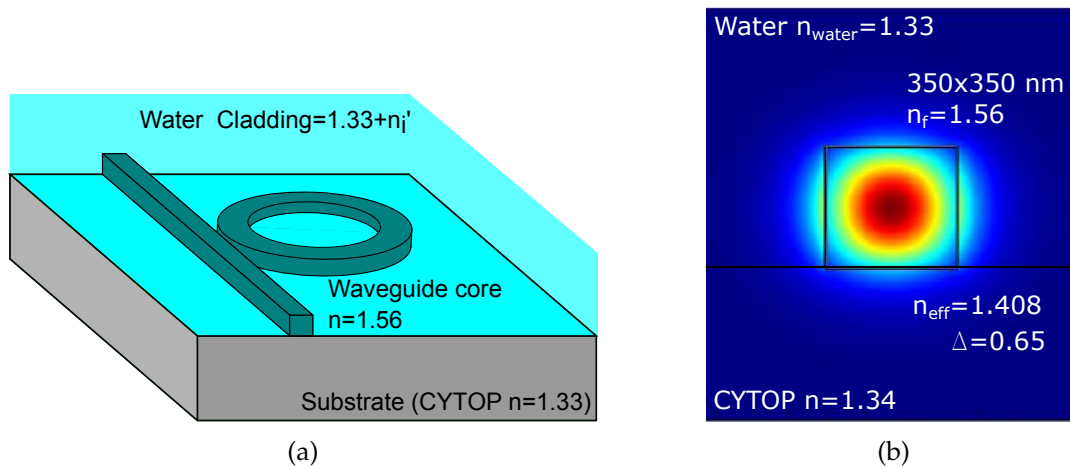


Figure 2.35: (a) Sketch of the ring resonator with a water cladding. The absorption of both the waveguide core and bottom cladding are constant and very dependent on the fabrication process. (b) Mode profile of the 350nm x 350nm polymer waveguide ($n=1.56$) with a confinement factor $\Delta = 0.65$. The absorption of the cladding depends on the top reagent extinction coefficient n_i .

top-cladding. Perfluorinated polymers such a CYTOP provide good thermal stability with water-like refractive index which is adequate for symmetric waveguide operation. The absorption of the cladding is tuned with color chemistry. Colorimetric reaction will modify the absorption of water thus modifying the complex refractive index of the top cladding ($n + jn_i$).

Lumerical MODE solutions software was used to study the effect of the Δn_i on the top cladding of the resonators presented in this study. The MODE package provides a 2.5 dimensional tool to easily simulate the optical resonance of planar structures. This method is based in the collapse of the main slab mode in a 3D structure. The key assumption is that there is negligible coupling between the different slab modes supported by the vertical waveguide structure. Fig.2.36 shows a typical re-

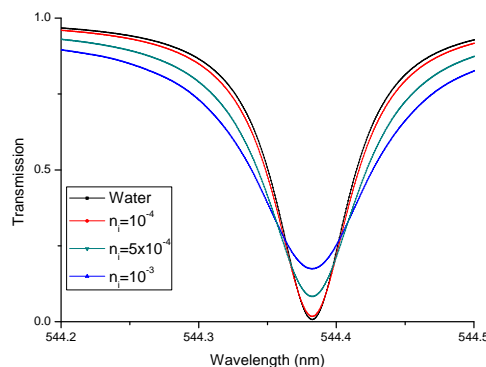


Figure 2.36: Transmission spectrum of an all-pass ring resonator for different complex refractive index variations. The increase of the complex refractive index ($n_i = 10^{-4}$ to 10^{-3}) can increase the transmitted power at resonance (decreasing the ON-OFF ratio.)

sponse for ring resonator acting as a notch filter with $15\mu m$ of radius. Water presents

very low absorption in the visible region of the spectrum, therefore no losses were considered for the reference water cladding during the simulations. Progressively, the top water cladding was modified increasing the complex refractive index ranging from 10^{-4} to 10^{-3} and decreasing the transmitted power. This modification can be adapted depending the reagent concentration used and the colorimetric indicator. Basically, the experimental extraction of the ring parameters can be achieved with curve fitting of the transmission function or by directly measuring the power drop or the ON-OFF ratio, which is the power contrast between the power transmitted at resonance and out resonance.

2.8.3 Ring resonator absorption architecture

The theory underlying the operation of the ring resonator has been intensively described in literature [116]. Here we consider the transmission function of a single coupled ring resonator acting as a notch filter. From microring resonator equations, the power at resonance can be written as a function of the resonator coupling parameters.

$$T(n_i) = \frac{P_{out}(n_i)}{P_{in}} = \frac{(r - a(n_i))^2}{(1 - ra(n_i))^2} \quad (2.13)$$

Where P_{out} and P_{in} are the input and output power, a represents the round-trip loss along the ring path L . In the following we have omitted the λ term at resonance.

$$a^2 = e^{-\alpha(\Gamma, n_i)L} \quad (2.14)$$

The absorption coefficient $\alpha = \alpha_{bent} + \Delta\alpha_{core} + \Gamma\alpha_{cladd}(n_i) + \alpha_{rough}$. All losses can be considered fabrication-dependent excepting the cladding losses which are affected by the variation of absorption coefficient of the colorimetric complex. r is the auto coupling factor which represents the ratio of power remaining in the input waveguide. Each term corresponds to the absorption coefficient due to the bent radius α_{bent} , the intrinsic absorption of the core α_{core} and cladding α_{cladd} , and the absorption losses produced by the waveguide roughness α_{rough} . The factors Δ and Γ refer to the ratio of guided power in the core and in the cladding respectively. Therefore, when Γ is large, the evanescent field extends into the lossy cladding increasing the total propagation loss. For a constant r factor, the transmitted power is tuned by the propagation loss of the ring waveguide. In this case the loss a depends on the variable losses of the top cladding n_i .

The sensitivity can be written in terms of the power at resonance as:

$$S = \frac{P_{out}(n_i) - P_{out}(0)}{n_i P_{in}} \quad (2.15)$$

Where P and n_i represent the optical power and the complex part of the refractive index (extinction coefficient) respectively. This equation represents the ratio of transmitted power loss due to a lossy perturbation added to the waveguide. For small

perturbations in the n_i , the equation can be approximated as follows.

$$S = \lim_{\Delta n_i \rightarrow 0} \frac{T(n_i + \Delta n_i) - T(n_i)}{\Delta n_i} \quad (2.16)$$

We can rewrite Eq.2.16 as follows:

$$S = \frac{dT(n_i)}{dn_i} \quad (2.17)$$

The derivative of T with respect to the extinction coefficient n_i :

$$\frac{dT(n_i)}{dn_i} = \frac{d\alpha(n_i)}{dn_i} L\Gamma a \frac{(a-r)(1-r^2)}{(1-ra)^3} \quad (2.18)$$

The sensitivity depends on the round-trip losses a and the autocoupling factor r that is proportional to the optical path. The imaginary part of the refractive index n_i is related to the absorption coefficient:

$$\alpha(n_i) = \frac{4\pi n_i}{\lambda} \quad (2.19)$$

Where we have only considered the influence of the absorption due to the lossy cladding. Therefore for $\lambda = \lambda_{res}$:

$$S = \frac{dT(n_i)}{dn_i} = \frac{4\pi}{\lambda_{res}} L\Gamma a \underbrace{\frac{(a-r)(1-r^2)}{(1-ra)^3}}_{\text{Enhancement factor}} \quad (2.20)$$

The first factor of this equation is proportional to the optical path ($S_0 = \frac{4\pi}{\lambda_{res}} L\Gamma$) while the enhancement factor is related to the augmentation of the optical path inside the ring resonator. We should note that the proposed equation is valid for small perturbations of the cladding ($\alpha \gg \alpha_{cladd}$). In different terms, the model is valid when the Δn_i to be measured is negligible compared to the intrinsic losses of the resonator.

When $r = 1$, the gap between the guide and the ring is too large therefore all the power inside the waveguide circulated to the photodiode and no power is coupled to the ring resonator. Then, the resonance damping is zero because no power travels within the ring. Oppositely, when $r = 0$ all the power inside the waveguide is coupled to the the ring resonator then:

$$\frac{dT(n_i)}{dn_i} = \frac{4\pi}{\lambda_{res}} L\Gamma a^2 \quad (2.21)$$

When $r = 0$ the sensitivity which is related to the power contrast at the output is given by a single round trip absorption. Therefore, it will be only dependent on the optical path and on the waveguide losses. The mode interacts with the analyte and the sensitivity will not be affected by any intensity build-up in the ring resonator.

2.8.4 Analysis of the optical path enhancement

Fig.2.37 shows the enhancement factor as a function of the autocoupling factor. We have considered different propagation losses which will affect sensor performance. The losses considered in this example can be intrinsic to the waveguide material or produced by the variable absorption of the top liquid cladding. The single round trip absorption is obtained when the autocoupling factor is $r = 0$. However, if losses are small the single-round optical absorption path can be enhance up to 10 times for $a = 0.98, r = 0.95$.

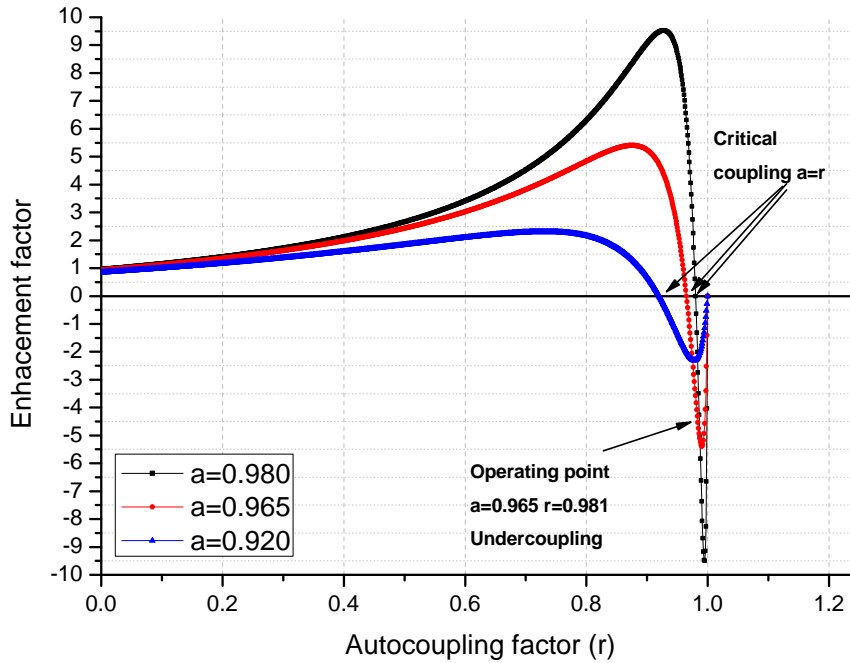


Figure 2.37: Enhancement of the single round trip sensitivity ($S(r = 0) = \frac{4\pi}{\lambda} L\Gamma$). Clearly, high quality devices provide best enhancement factor. The role of the autocoupling indicates that the best enhancement is obtained for slightly overcoupled/undercoupled rings. The operation point given par *Nitkowsky et al.* is indicated at $r = 0.9812$ and $a = 0.965$.

During critical coupling ($r = a$) small perturbations in the cladding absorption do not affect significantly the ring transmission, this point corresponds to the intersection with the horizontal axis. Maximum sensitivity contrast is obtained during a slight under or overcoupling. Negative sensitivity values appear once the critical coupling is achieved, that can be explained as follows: when the system is overcoupled ($a > r$) an increase in the propagation losses ($a \rightarrow 0$) implies a drop in the transmission ($T_{out}(n_i) < T_{out}(0)$) and so an increment of the ON-OFF ratio. In contrast, if ($a < r$) an increase in the propagation losses ($a \rightarrow 0$) implies a reduction on the ON-OFF ratio ($T_{out}(n_i) > T_{out}(0)$). Physical sensitivity values are taken in absolute value.

Ring resonators presented by *Nitkowsky et al.* [34] shown a resonance quality factor of $Q=120000$. Without any gap optimization the presented devices operate

with slightly under coupled conditions ($a = 0.965$, $r = 0.981$). Such devices exhibited an effective path length 6 times higher than a single round-trip that agrees with our predictions. It is important to note that the critical coupling provides a negligible shift in the output power since the major part is lost in the ring. Therefore, in order to increase the sensitivity, overcoupled or undercoupled ring resonators are preferred. In particular, slightly overcoupled schemes would be preferred because the devices shown a smooth slope in the optical path enhancement compared to the sharp peak occurring for the undercoupling configuration. Nonetheless, overcoupling will occur for small gaps which can be more complex to obtain depending the operation wavelength. As mentioned critical coupling provides null resonance power contrast

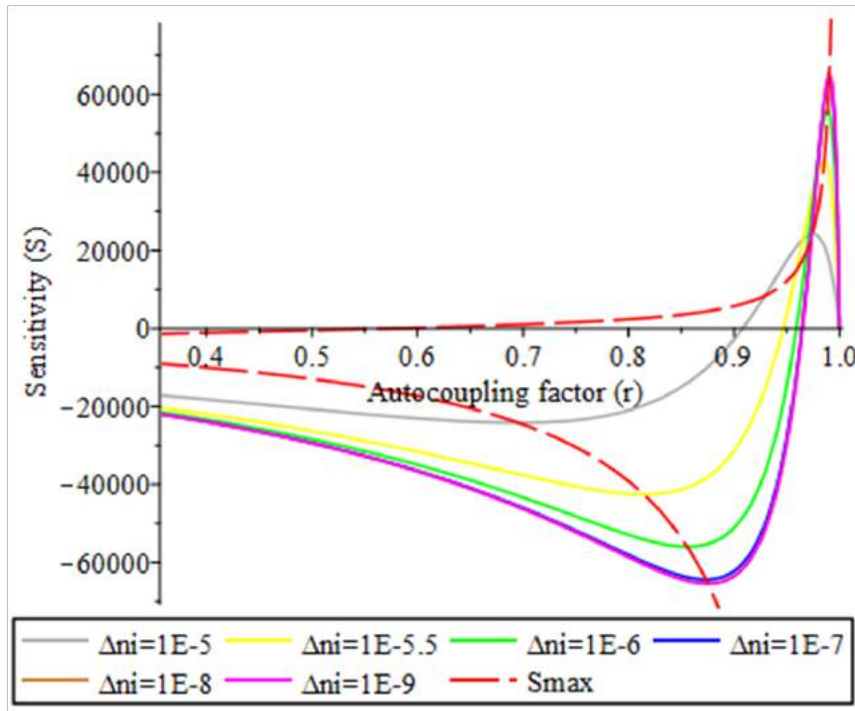


Figure 2.38: Sensitivity curve for a resonator with intrinsic losses $a = 0.96$ ($n_{i0} \approx 5.8 \cdot 10^{-6}$). For small variations $n_{i0} \gg \Delta n_i$ the sensitivity curve will be stable around a fixed operation point. For large variations the behavior of the resonator is greatly affected

in presence of a small perturbation, in order to maximize the sensitivity the can extract the optimum r factor r_m to maximize the sensitivity $S_{max} = S_0 \cdot E_{max}$. We can distinguish two r values for the over-coupling and under-coupling configuration to which both impose maximum sensitivity. Analyzing the Eq.2.20 we obtain for the under-coupling $r > a$:

$$r_m = \frac{\sqrt{3}(a^2 - 1) - 2a}{a^2 - 3} \quad (2.22)$$

And in the same manner, for the over-coupling $r < a$:

$$r_n = -\frac{\sqrt{3}(a^2 - 1) + 2a}{a^2 - 3} \quad (2.23)$$

For a resonator with well know loss factor a we can directly obtain the coupling factor leading to the maximum enhancement of the optical path allowed. Considering the pair of values r_m and r_n , the maximum enhancement factor becomes:

$$E_{max} = \pm \frac{2a}{3\sqrt{3}(a^2 - 1)} \quad (2.24)$$

2.8.5 Optimization of the ring length

High sensitivity with high optical path enhancement is obtained by using low-loss cavities (High Q) or by increasing the optical path. Nevertheless, ring resonators with very large radius can lead to dominant propagation losses due to an excessive optical path. It is clear that an optimum radius exists depending on the propagation losses. Thus, we have studied the influence of the ring radius and the autocoupling factor for different propagation losses in the ring resonator. For that, it is considered a moderate confinement factor $\Gamma = 0.25$ with $\lambda = 532$ nm. As the main source losses in microring resonators is considered to be due to propagation, we have considered negligible bent loss ($a_{bent} \sim 1$) for large resonators $R > 40 \mu m$. In Fig.2.39 (a) propagation losses are set to $\alpha = 10 \text{ cm}^{-1}$. In this case, strong coupling is needed to maintain correct device performance. In addition to the strong coupling regime if the ring radius is larger than $R = 140 \mu m$, device losses become dominant and the device performance decreases. In Fig.2.39 (b), if ring resonators are fabricated with low propagation losses $\alpha = 1 \text{ cm}^{-1}$, the device footprint can be extended while maintaining correct performances. Compared to the ring with higher propagation losses, we should note that larger r factor are needed to maintain optimal operation. Although the optical path increases, the sensitivity remains stalled due to the increase of the round-trip losses. Moreover, the free spectral range (FSR) is inversely proportional to the optical path, thus large radius provides closer resonances which can enhance sensor dynamics using tunable laser sources.

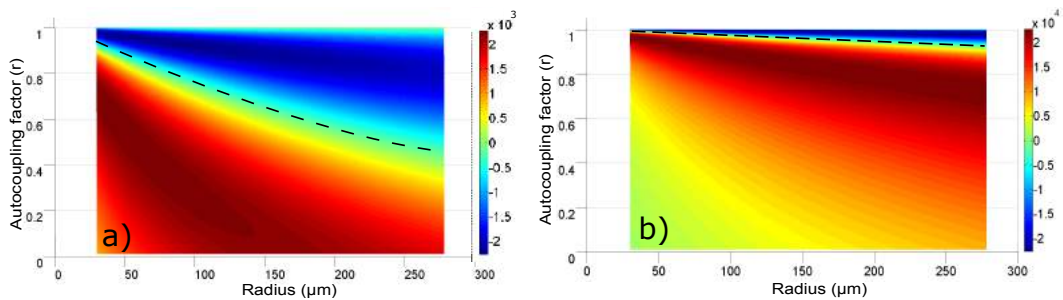


Figure 2.39: Sensitivity is represented with the colorbar versus the ring radius and the autocoupling factor r for two different propagation losses (a) 10 cm^{-1} , (b) 1 cm^{-1} . The dash line represents the critical coupling separating the undercoupling and overcoupling regimes.

2.8.6 Detection limit

The limit of detection (LoD) is defined as the minimum measurable quantity of analyte that a sensor can detect and measure. Therefore, during absorption sensing, the LoD is given by the minimum distinguishable power variation (δT) measurable by a photodiode. This minimum power variation is related to the complex part of the refractive index (n_i) and the sensitivity $\Delta n_i = \delta T / S$. As stated before, sensitivity is proportional to the optical path and strongly dependent on the resonance sharpness. Low losses provide correct measurable power drop but very sharp resonances make the sensor extremely dependent on external conditions. For example, environmental temperature changes lead to an uncontrollable mismatch between the pre-laser linewidth and the resonance which adds additional noise measurement. If we consider the values presented above, state-of-the-art for ring resonators operating at visible wavelengths with $a=0.967$, $\Gamma = 0.25$ ($\alpha = 1.07 \text{ cm}^{-1}$) would provide $S \simeq 20000$. Assuming distinguishable power variations of about 2% at resonance, it allows for a LoD down to $\Delta n_i = 10^{-6}$.

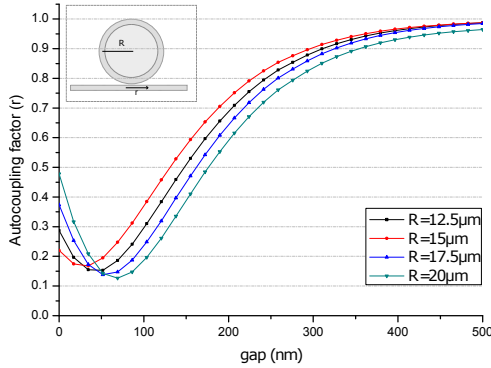
As an application example, in [32] we determined the variation of the complex refractive index of a colorimetric metallic complexation of hexavalent chromium with 1,5 diphencylcarbazine (DPC). For this complexation we reported $\alpha = 0.2 \text{ cm}^{-1}$ ($n_i = 1 \cdot 10^{-6}$) corresponding to $200 \mu\text{g}/\text{L}$ of Hexavalent Chromium diluted in water. Supposing ring resonators with the performances cited above, it leads to the limiting distinguishable concentration of the ring resonator. Therefore ring resonators with well characterized propagation losses a can be used as microspectrometers. Low propagation loss provides high enhancement factor and the subsequent power shift at resonance. However, the sensitivity is also limited by the power resolution of the measurement tools.

2.8.7 Validity of the model

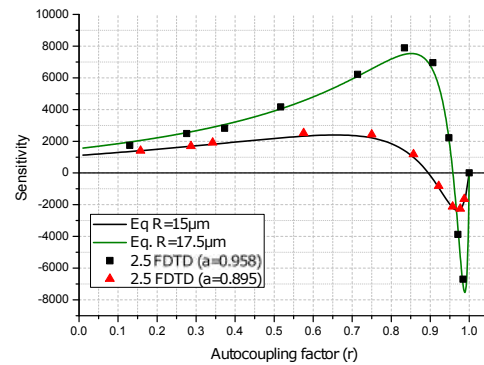
In this section we simulate the ring resonator as microspectrometer in order to compare the obtained performances with the predicted. More precisely, we simulate the response of a ring resonator with the geometry outlined in Sec.2.8 varying the autocoupling factor (different ring gaps). We study the difference between the transmission of the ring resonator with water cladding and when the cladding is modified by $\Delta n_i = 10^{-5}$. The difference is extracted at resonance. First of all, the autocoupling factor r is calculated studying the transmission of the directional coupler section of the ring resonator. The obtained r factor values are shown in Fig.2.40a. Then, we simulate full ring resonator with two radii $15 \mu\text{m}$ and $17.5 \mu\text{m}$, the power drop is studied for different gap sizes at resonance $\lambda_r=534.6 \text{ nm}$ and compared with the proposed equation Eq.2.20. The results are plotted in Fig.2.40b with the 2.5FDTD values shown in Tab.2.3.

Gap (nm)	r	Ref.T (Water)	Lossy T($n_i = 10^{-5}$)	Difference
0	0.287	0.695	0.678	0.017
55	0.157	0.784	0.770	0.014
110	0.342	0.677	0.658	0.0252
167	0.575	0.474	0.448	0.025
222	0.750	0.232	0.207	0.024
278	0.857	0.054	0.042	0.011
333	0.921	0.045	0.036	-0.008
389	0.957	0.195	0.217	-0.021
444	0.976	0.430	0.453	-0.022
500	0.987	0.641	0.657	-0.016

Table 2.3: The table shows the gap for each value with the associated r factor. The transmitted power values for each r at the output of the water cladding resonator are compared to the output after adding an absorptive perturbation to the cladding ($n_i = 10^{-5}$).



(a) Auto-coupling factor for different ring radius.



(b) Verification of the model with 2.5FDTD simulation.

Figure 2.40: (a) When $r = 1$ no power is coupled into the ring. When the gap is too small ($r \sim 0$) ($<70\text{nm}$), the power coupled into the ring resonator comes back to the bus waveguide. Simulations were done at $\lambda=532\text{nm}$. (b) Comparison between the proposed equation and the results from the 2.5 FDTD simulations ($\Gamma = 0.25$, $R=17.5 \mu\text{m}$ and $R=15 \mu\text{m}$)

For each coupling configuration (r), the lossy transmission at resonance (Lossy T($n_i=10^{-5}$)) is subtracted from the lossless transmitted power reference (Ref.T(Water)). If $R=15 \mu\text{m}$, the bent loss dominates with a single round trip propagation loss of $a = 0.895$. If the ring radius is $R=17.5 \mu\text{m}$, the effective optical path can be increased by a factor 2.5. As shown, resonators with lower intrinsic losses can present higher enhancement factors. This is illustrated with a larger ring radius $R=17.5 \mu\text{m}$. The sensitivity is enhanced up to 4 times ($r = 0.9$) due to the larger optical path but also, due to the reduction of the bent losses. For this larger ring, the total round trip loss is $a = 0.958$ with an optical path enhancement close to four times the single round trip absorption ($r = 0$). Allowing to compare these results, full experimental results are extremely challenging needing repeatable fabrication process controlling accurately

the gap.

2.8.8 Conclusion

In this chapter we have presented the basis of the nanostructuring of polymers with soft imprint lithography. Important aspects such as the design of the master stamp and the sizing of the waveguides were also discussed to manage the effects of the RL. We concluded that 350 nm x 350 nm waveguides made of UVNIL allow single mode propagation for both water and air claddings. The influence of the residual layer was studied for the waveguide, the grating couplers and the ring resonator. Detailed information about the discussed process and characterization strategies are given in the next chapter. Regarding the sensing strategy, we have presented an analytical approach for the microring resonator performance as microspectrometer which provides the theoretical support for the experimental works referred in this thesis. Similar to the optical path based sensors, low-propagation losses and large optical paths are the main requirements to obtain the best performances. Nonetheless, in this work we report additional considerations regarding the coupling parameters. Over-coupled or under-coupled resonators must be designed instead of the intuitive critical coupling. This criterion is of main importance saving worthless optimization efforts during the fabrication steps which would not provide better sensor performances. The results provided by the equations discussed in this work show both well agreement to the experimental results found in the literature and to the FDTD simulations. Considering the discussed sensing strategy, state-of-the-art propagation loss devices lead to optical path enhancements up to 10 times and LoD of 10^{-6} . Being this limit enough to detect concentrations down to $200\mu\text{g}/\text{L}$ of Hexavalent Chromium. For large ring resonators ($R > 100\mu\text{m}$) it implies mm-sized optical paths as found in commercial spectrometers. These results support the use of ring resonators as microspectrometers for applications requiring the handling of resonator footprint-like volumes of liquids providing a feasible integration within small packages.

Chapter 3

Fabrication and characterization results

The experimental results concerning the fabrication and test of the designed devices are reviewed in detail along this chapter. We divide the chapter in two main sections: the first section is devoted to the fabrication results and the second one, to present the optical response of the imprinted devices. We show the original fabrication process resulting from the dedicated master stamp design as well as some interesting results regarding the behavior of the polymer under thermal cycling. These results would be of main importance when considering further performance of these devices for the long-term use.

3.1 Nanostructure fabrication and characterization

The general process flow, the design of the structures and the proposed utilization of the microring resonators as micro-spectrometers is reviewed in the Chapter 2. Along this chapter we transform the proposed design into real devices with two nanopatterning technologies: the EBL and the soft-imprint lithography. A close regard is given to the fabrication details and the characterization of the imprinted nanostructures. The fabrication process begins by transferring the discussed geometries in the layout. Then the optimal EBL configuration is chosen after long optimization cycles, the best trade-off between energy dose is shown in the Annexe. Once the master stamp is patterned, the transferred structures are characterized by atomic force microscopy (AFM) and by the scanning electron microscope. Subsequently, we proceed to use the master stamp for the soft stamp replication. We also show the nanoimprint process and as figure of merit of the replicated structures we show the overlap of the AFM characterization curves for both the master stamp and the final imprinted device. To study the polymer thin film, we use two optical characterization techniques: a phase retarded ellipsometer and a M-line characterization by prism coupling. The ellipsometer is used to characterize the thermo-optic coefficient (TOC) of the resist and the M lines is used to determine the effective index of the layer. The TOC is extremely important to characterize the variations of the refractive index with the temperature, since this will be useful to characterize the optical response of the ring

resonators. The measurement of the effective index serves as a first comparison with the effective index calculated by LUMERICAL.

3.2 Polymer patterning and characterization tools

3.2.1 Layout generation of the master stamp

The structures are designed in the layout which is a specific vectorial design tool for mask design of Raith. The chip size is set to an standard $1 \times 1 \text{ cm}^2$ prototype size. The chip shows single transmission lines either with simple waveguides or with and without OMR. Each line presents the tapered shape with an embedded grating coupler with period of 290 nm. Some lines were done with the double grating (input-output Fig.3.1(a)) with ring resonators (Fig.3.1(b)). We also designed devices with only a single grating (Fig.3.1(c)) performing the output coupling by the end waveguide facet. We tried to extract as much data as possible by distributing different patterns for optimization. For example, grating coupler matrices were added to the layouts to study the optimal dose-line-width configuration Fig.3.1(d).

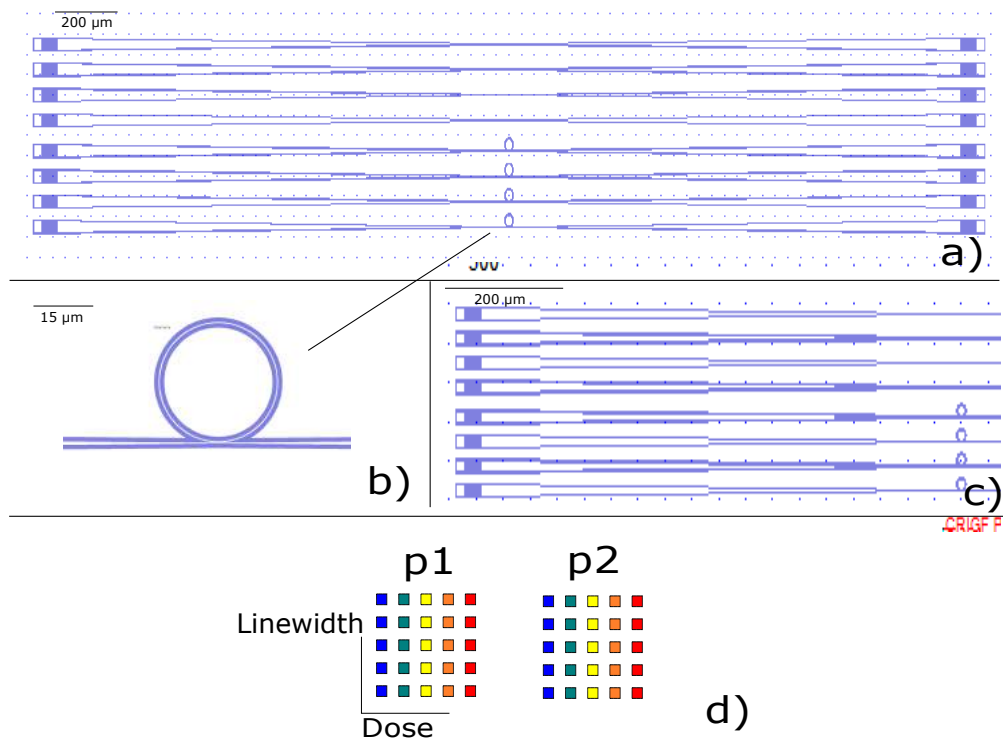


Figure 3.1: Layout design of the structure for the master stamp. (a) Long waveguide (6mm) with/without ring resonators and grating couplers. (b) Close view of the trenches defining the ring resonator ($R = 15 \mu\text{m}$). (c) Waveguides with/without ring resonator and a single grating coupler. (d) Linewidth/dose test to study the optimal grating coupler recipe

Similar matrices were added to find the optimal dose for the gap. As mentioned, we only pattern the waveguide edges with the EBL. Therefore the final dimension depends on the dose, the beam energy but also of the trench size which has to be optimized. In the tiniest part of the line, the waveguide is 450 nm width with constant trenches of 2 microns around and along the waveguide. If larger trenches are patterned nearby, the resulting waveguide width is reduced due to the add-up of the proximity effects along the waveguide.

3.2.2 EBL exposure

The silicon substrates are first immersed in a piranha solution ($H_2O_2 + H_2SO_4$, 1: 1 vol.) for 4 minutes, rinsed with deionized water (DI) and dried with nitrogen before being exposed to plasma O_2 treatment (200W, 2 minutes). Then, the substrates are dehydrated under a thermal exposure for 15 minutes at $200^\circ C$. We spin coat 400 nm of positive-tone resist PMMA on the wafer. We consider this thickness enough taking into account the etching of both waveguide and grating. Then the resist is soft-baked at $90^\circ C$ to relax the polymer chains. As discussed, the shallower structures are exposed first (grating). Therefore, a second spin coating of 400 nm is enough to cover homogeneously the already etched grooves without producing excessive swing effect¹ around the grating, which is controlled with the mechanical profilometer. If the waveguides are etched first, we would probably need a planarization layer to ensure the spin coating over a flat surface as done by Finn. However, it supposes expensive SiO_2 deposition and additional steps. Like a double exposure process, we must produce alignment marks on the waveguide corners to set-up the coordinates for the electron beam alignment. The alignment step is required to expose the waveguide edges around the already patterned grating.

Once the grating is exposed, we develop the exposed resist with a combination of organic solvents already optimized by the LAAS. The combination is IPA: MIBK providing an adequate selectivity between both solvents. The development is set-up to 1 minute, then the samples are etched using an Inductively Coupled Plasma - Reactive Ion Etching machine (ICP-RIE ALCATEL AMS4200). Process parameters are as follows: pressure 8.10-3mbar, power 450W (coil) / 30W (platen), gas mixture $SF_6 : C_4F_8 : O_2$ with respectively 30:45:3 sccm of flow rate. The average selectivity of the formulation of PMMA on Si for this recipe is 1.4 nm etched Si for 1 nm etched of PMMA (1.4/1). This etch ratio is valid for micronic structures. Submicrometric structures need more time than larger structures to achieve the same etch depth, this process is known as ARDE effect (Aspect Ratio Dependent Etching). Since the tolerance set-up for the etch depth is high (20%) we compensate with a short additional time of few seconds with no process optimization. The grating couplers are etched during 130 seconds while the waveguides are etched during 4 minutes.

¹The swing effect is the oscillation of the resist thickness due to the spin coating process around a nanostructure

3.2.3 Master stamp results

The grating images were taken making the transversal cross-section with a Focused-Ion Beam (FIB). These figures have not the optimized period, but they serve as an example due to the limited quantity of fabrication batches. Two height master stamp (grating and waveguide) were patterned via double exposure Fig.3.2(a). The grating shows a etch depth around 150 nm for a period of 400 nm Fig.3.2(b). Several ring resonators were fabricated with different gaps Fig.3.2(c). The Fig.3.2(d) shows a close view of the smallest gap obtained which is 80 nm on the upper region and 50 nm at the bottom of the gap groove. Other periods and gaps were achieved, but they are not shown in the manuscript.

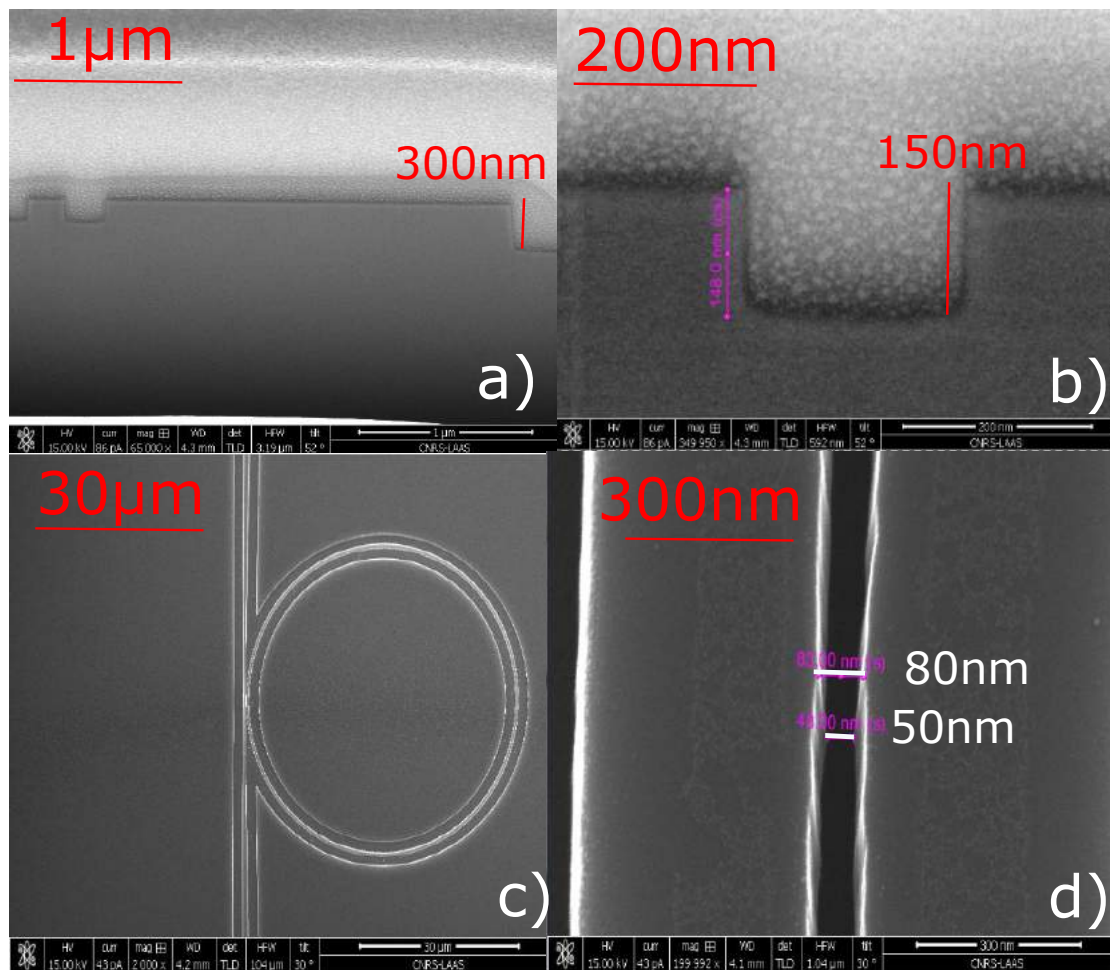


Figure 3.2: SEM images of the two height master stamp. (a) A cross-sectional view of two heights (150/300 nm). (b) A grating groove with a period of 400 nm and 150 nm of etch depth. (c) Overview of a ring resonator of the master stamp. (d) Close image of the ring gap.

3.2.4 Intermediate soft stamp

Once the master stamp is fabricated, and before further utilization for imprinting processes, we have applied an anti-sticking layer to avoid ripping-off of the waveguides. We have deposited the anti-sticking treatment with the Surface Preparation and Deposition equipment from MEMSSTAR. The surface treatment consists in a self-assembly monolayer of Perfluorodecyltrichlorosilane (FDTS). Such a process step allows to lower the surface energy of the SOI master stamp with deionized water contact angles of 108° .

The intermediate stamp is done with the COC8007(TOPAS) polymer sheet which due to his low $T_g=74^\circ\text{C}$ allows for imprinting at low temperatures. Proper cavity filling is obtained from 150°C to 120°C . When lower temperatures are applied, we appreciate defects related to the cavity filling (e.g. gray scales around the grating edges). The applied load is 400 psi for 5 minutes, which is the maximum processing time allowed by the machine. As we are not seeking for industrial production, the time is not optimized to improve the device throughput. The Fig.3.3 shows details

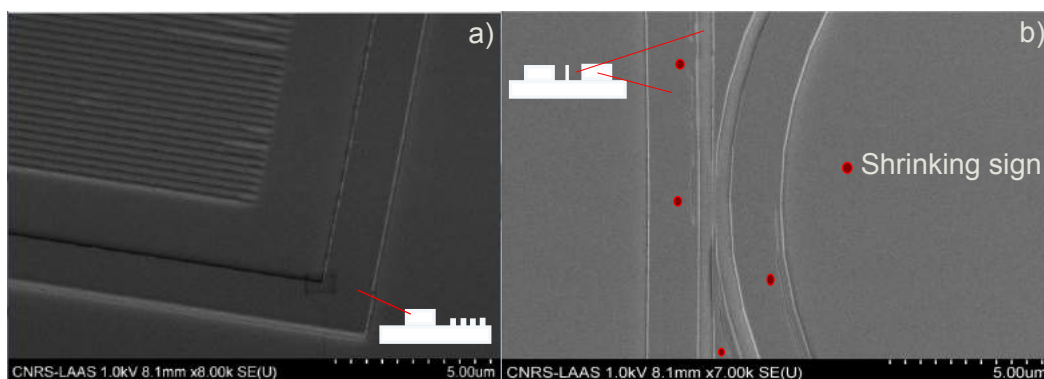


Figure 3.3: SEM image of the soft-imprint stamp. a) Grating coupler transferred to the COC(TOPAS) showing the trenches used to enhance the polymer flow (MPSM). (b) SEM image of the gap of the ring resonator. We can appreciate shrinking marks (red spots) around the gap, ring, and waveguide.

of the intermediate soft stamp. The grating coupler and ring resonator are imprinted ensuring that the cavity filling is good enough (Fig.3.3(a)). However, probably due to the thermal expansion signs of shrinking or drifting are present around the waveguide structure. We can notice that these kinds of signs always appear on one side of the structure suggesting that this occurs due to thermo-mechanical expansion along a preferred axis. This drift is extremely difficult to control as far as we don't know the expansion axis of the amorphous sheet of COC. This drifting occurs along ≈ 100 nm more or less. Therefore, smaller gaps are bent or collapsed not being replicated to thermoplastic sheet. Despite the indicate defects on the ring resonator, larger gaps can be imprinted. However, the exact gap cannot be known preliminary due to the

drift of the thermoplastic. FIB cross section would provide the information but destroying the device after all.

3.2.5 Cladding layer

Despite the defects shown around the ring resonator, the waveguides and the grating couplers can be perfectly imprinted with almost-no defects. Prior to the nanoimprint process, we clean a wafer with piranha bath and O_2 plasma treatment as we have done for the master stamp fabrication. Our devices, composed of grating couplers and waveguides are processed from standard silicon substrates coated with CYTOP as bottom cladding and NILUV-394 photo-resist is used for both the waveguide and the grating couplers.

To reach a thickness near 500 nm, the 9% of solid content of CYTOP (CTL-809M, AGC Chemicals) is diluted in CT-SOLV 180 (AGC Chemicals) to obtain a 5% final solid content. The objective of this dilution is twofold:

- reach the final thickness at reasonable speeds of spin-coating (around 1000rpm for 20s),
- get rid of the non-uniformity observed for thick layers .

After the spin-coating step, the samples are baked at 180°C during 3 hours. The oven have been chosen instead of the hot plate because it allows simultaneous curing of multiple wafers. Due to the CYTOP hydrophobicity, a surface treatment is mandatory to obtain a good adhesion during spin-coating of the waveguides material. We used the same method that consists in the deposition of a thin (100 nm) Al layer via thermal evaporation, followed by wet etching, DI water rinsing and nitrogen blow drying as reported in [80]. With such a method, both an improvement of the wettability (DI water contact angle $< 20^\circ$) and a good adhesion of additional spin-coated layers as well as reproducible deposits have been obtained.

3.2.6 Nanoimprint

Then, NILUV-394 is immediately spin-coated on the CYTOP layer without prior dehydration. One can note that a heating of the CYTOP at this step would reestablish its natural hydrophobicity. After a 3min baking step at 60°C on a hotplate, the sample is then introduced in a Nanonex NX2500, covered with the previously obtained COC8007 soft stamp and exposed to the soft-UVNIL step at 200 psi and 5 minutes at room temperature with UV-exposure. The sample is then unloaded and the soft stamp manually peeled in the direction of the waveguides. To allow edge emission, polymer waveguides are cleaved along the crystalline axis of the Si substrate without posterior polishing or etching. The obtained polymer waveguide is shown in Fig.3.4.

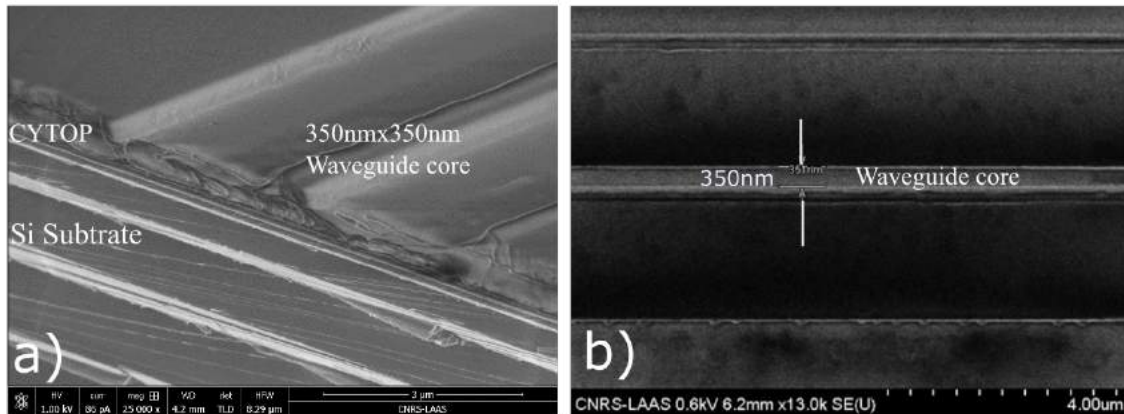


Figure 3.4: (a) SEM image of the transversal cross-section of a cleaved waveguide. (b) 350 nm^2 cross-section polymer waveguide with 50 nm of RL. This layer thickness is measured combining optical ellipsometry and a mechanical profilometer.

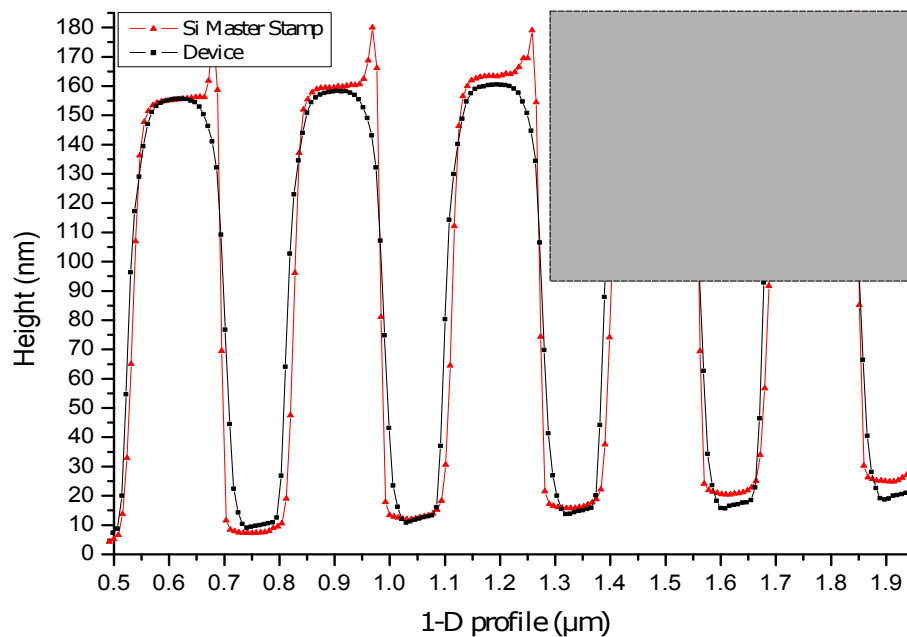


Figure 3.5: Comparison between the grating profile of the SOI master mold (red) and the final device (black) obtained with an intermediated COC8007 soft stamp. The final device is made in NILUV-394 deposited atop the CYTOP cladding on a silicon substrate. The inset shows a SEM picture of the fabricated grating ($\Delta = 289 \text{ nm}$).

The grating coupler, taper and waveguide, that made up the whole polymer structure, were successfully imprinted in a single step. The thickness of waveguide and the grating depth measured by AFM are 350 nm and 150 nm respectively. As

a figure of merit, a comparison between the imprinted structure and the SOI master stamp feature is presented in Fig.3.5 showing high imprint fidelity between the master stamp and the polymer grating. The use of the COC soft stamp with its low Tg helps to reduce the thermo-mechanical residual stress resulting from the imprint process, with no visible defects along the 4mm waveguide nor modification of the grating period. In contrast, shrinkage effects up to 1%, leading to defects especially on the edge of the waveguides have been routinely observed using high temperature thermoplastics as ZEONOR. To summarize, low Tg COC/COP soft stamps (solvent-free resists for soft-UVNIL) or hardened PDMS (solvent-based resist for soft-TNIL) are the most relevant materials to imprint very large structures with nanometer features.

3.2.7 Samples

Cleaving is a fast solution to provide acceptable optical facets in the polymer. Larger polymer facets such as micrometric waveguides can be polished mechanically. However, due to the low cross-section of our waveguide they cannot be polished without damage of the thin polymer films [32]. Other possibilities consist of double grating couplers one for both input and output. Along with a large number of structures available we focus our attention on three types of devices. Cleaved waveguides (A), cleaved waveguides with ring resonator (B) and waveguides with input/output grating couplers (C). The material combination and dimension are shown in the Fig.3.6. Most of the results shown in this thesis focus around devices of the family A and B. We have also used UV curable polymer ORMOCORE which has a higher refractive index than UVNIL. This is useful for the final application regarding the ring resonator.

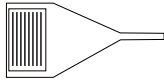
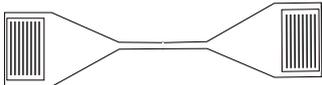
	Structure	Period	Material	Length
A		290nm	UVNIL394	4mm
B		290nm	ORMOCORE	4mm
C		330nm-440nm	ORMOCORE	6mm

Figure 3.6: Table with the devices addressed in this work.

3.3 Characterization of thin waveguide polymer films

After the regular inspection of the fabricated devices. It's crucial to study the optical properties to test if the waveguides can serve as designed. In this part, we focus our interest on two optical characterization techniques: ellipsometry and prism coupling. The ellipsometry is not only performed to verify the thickness and refractive index of the imprinted materials but also to study the feasibility and limitations of the TOC measurement which will be of major importance during characterization. The measures were performed with a Phase-Modulated Spectroscopic Ellipsometer. In the other hand, we have used the M-lines method to couple light into the waveguide layer to study the effective index of a layer of NILUV this is a first experimental value to compare with the simulations and the effective index calculations.

3.3.1 General ellipsometry of thin films

A spectroscopic ellipsometer (SE) measures the change in polarization between the incident light and reflected light. The ellipsometer obtains raw data: amplitude Ψ and phase shift Δ from the measurement at a single angle of incidence (AOI or Φ) at single wavelength. From this data, the film thickness d and the refractive index ($n + jk$) can be calculated. These equations can be found in general literature about spectrometric ellipsometry. The relationship can be expressed generally as:

$$(d, n, k) = f(\Psi, \Delta, \lambda, \Phi) \quad (3.1)$$

If the angle and the wavelength are fixed the equation becomes:

$$(d, n, k) = f(\Delta, \Psi) \quad (3.2)$$

Although there are three unknown quantities in the above equation, only two independent variables can be measured with a single-wavelength ellipsometer. Therefore, one of the three unknown quantities (d, n, k) must be fixed as a known quantity. However, we can obtain all the parameters varying the incident angle or using a broadband source (white LED, supercontinuum source). The equation becomes:

$$(d, n(\lambda), k(\lambda)) = f(\Delta(\lambda), \Psi(\lambda)) \quad (3.3)$$

The refractive index n and extinction coefficient k can be determined by fixing the thickness of the layer under test which is wavelength independent. The typical principle of the ellipsometry is shown in Fig.3.7. The incident wave is polarized and sent onto the surface to analyze with an incident angle Φ . The reflected spot presents an shifted ellipsoid, the shifts in phase Δ and in polarization Φ are measured with a

photo-elastic modulator and a polarization analyzer².

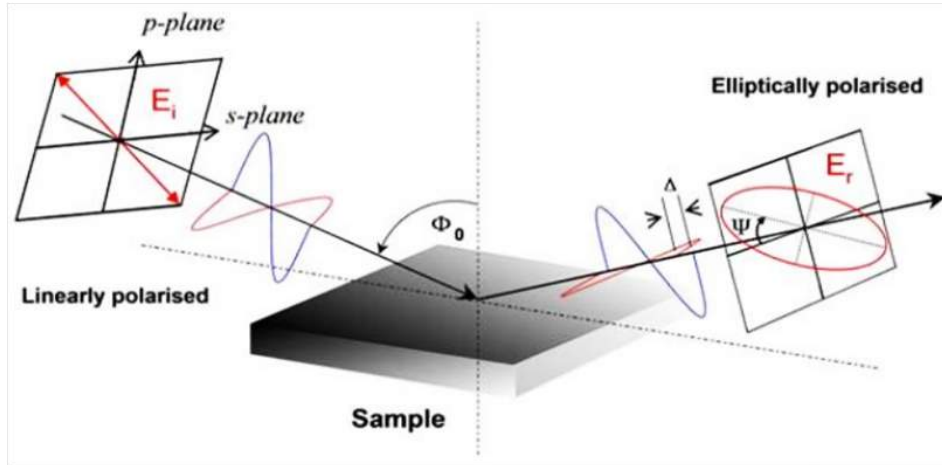


Figure 3.7: The change in polarization is measured with an ellipsometer. An incident plane wave with an angle Φ with a fixed polarization (p,s) is reflected from the surface. The reflected elliptical spot is analyzed. The ellipsometer measures the shift in Δ and Ψ .

The ratio of the reflected wave is related to the parameters Δ and Ψ can be written as:

$$\frac{\tilde{r}_p}{\tilde{r}_s} = \tan(\Psi)e^{i\Delta} \quad (3.4)$$

Most of ellipsometer users are more familiar to the I_c and I_s term which are related to the ellipsometer parameters as follows:

$$I_s = \sin(2\Psi)\sin(\Delta) \quad (3.5)$$

$$I_c = \sin(2\Psi)\cos(\Delta) \quad (3.6)$$

Which provides values comprised between -1 and 1.

The complexity of the problem increases when the thickness also varies for example due to thermal expansion, or when there are several layers without showing enough index contrast. The thickness of the substrate is not constant and geometry dependent, besides, all the layers of the stack also expand and change their optical properties. Therefore we must try to distinguish the contribution of each layer both in terms of refractive index and thickness variation before determine the parameters of the polymer layer. In order to address this problem we propose the following steps

- Modeling the problem (multi-layer, parameters, roughness..)
- Determining material properties which can be easily verified

²<http://www.horiba.com/scientific/products/ellipsometers/ellipsometry-academy/ellipsometry-tutorial/phase-modulation-spectroscopic-ellipsometer/overview-of-phase-modulation-technology/>

- De-correlating index-thickness measurements for the polymer.

In the next section we address the cited points, first we need to propose a mathematical model to reproduce physical results. This model involves assumptions about the stack of materials, the temperature gradient and the state of the surface. Subsequently, it is helpful to know some of the "true" physical parameters of the stack of materials to compare with our results. These parameters can be the TOC of the Si wafer and the index and thickness of the polymer. These parameters can be already found in the literature or determined previously by other metrology techniques. Finding the same physical parameters with our model ensure the quality of our acquisition process. For example before determining the behavior of the polymer we must obtain a reliable method to decorrelate the influence of the bottom substrate. Finally, we propose a strategy to reduce the correlation between the index and thickness of the polymer which will consist in a refractive index measurement on a polymer bulk.

3.3.2 Ellipsometry of the multilayer stack: TOC of the Si substrate

To perform the measure we must present the polymer onto an adequate substrate. To the extent possible, the properties of the substrate must be known prior to the study of the top polymer layer. In our case the thin polymer layer must present a good surface state and approximately the same thickness as the final waveguides (≈ 400 nm). Therefore, we consider 2 different substrates Si or glass. Si wafer is our preferred choice because, besides the good conductivity and good surface roughness, its behavior with temperature are well known in the literature. SiO_2 can also be a good choice; however, the low index contrast with polymers can negatively affect the sensitivity of our measurements. However, the Si wafers surface oxidate in the presence of Oxygen; this oxidation produces a thin layer of SiO_2 on top of the Si surface usually called "native oxide". This thin oxide layer of 1-4 nm of thickness has to be taken into account in the ellipsometry measurement. The multilayer of materials to is shown in Fig.3.8.

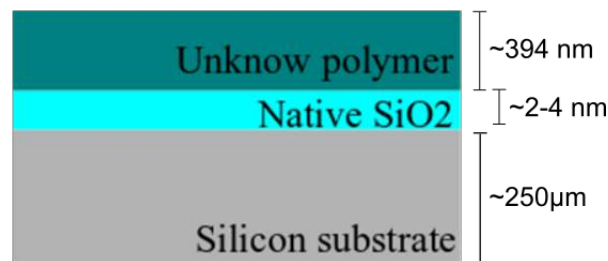


Figure 3.8: Stack of materials studied by a phase modulated ellipsometer.

As we are working with thin layers the contribution of each material interface must be perfectly known. So we propose to study the thermal response of the substrate and compare the obtained TOC with the values found in the literature. This

is very useful to validate our measurement methodology and to properly know the underlying layers. In this case, the interface $Si/SiO_2/air$ should be modeled. We start with the assumption that the thin native SiO_2 layer optical properties are the same as bulk SiO_2 . However, the optical properties of thin and bulk SiO_2 are different as shown in the literature. For this comparison, we have fixed the thickness and the index of the SiO_2 layer. For the first study, we have measured the TOC of only the Si substrate. We have fixed the thickness and the index of the SiO_2 layer. Several references have been found studying the TOC coefficient of Si/SiO_2 materials, as a reference we have chosen [119] [120]. We have repeated lots of measurements with different incident angles, different wavelengths, under an inert gas atmosphere, up and down temperature cycling. After averaged TOC coefficient for the Si is determined to be $5.2 \cdot 10^{-4}$ at $\lambda = 530$ nm with standard deviations up to 10% over the average value. This variation is mainly due to the movement of the wafer due to the thermal expansion. However, this is good agreement with the values obtained in the literature ($5 \cdot 10^{-4}$). This variation around $\delta = 10^{-5}$ during the index-thickness acquisition is reported to the TOC determination of the polymer layer. Despite this variation, the model obtained for the Silicon provides very similar values to those found in the literature.

We have validate our set-up and our acquisition process. since the bottom layer is know we can perform the thermal measurement on the polymer. In order to do that, we spin coat 394 nm of NILUV on top of the same Si substrates. Once the substrate TOC is know we can decorrelate the influence of the polymer individually. This problem is addressed in the following subsection.

3.3.3 Thermo optic coefficient of thin polymer films

Polymers, with weak, secondary, intermolecular bonds (low melting points) have very high expansion coefficients and low strain polarizability constant which results in large negative thermo-optic coefficients. This property is present in several organic and inorganic materials. The TOC can be obtained from the Lorentz-Lorenz equation (3.7) which shows the relationship between the TOC and the coefficient of thermal expansion (CTE).

$$\frac{dn}{dT} = -\rho\gamma \left. \frac{\partial n}{\partial \rho} \right|_T + \left. \frac{\partial n}{\partial T} \right|_\rho \quad (3.7)$$

Where ρ is the density of the polymer and γ is the volumetric thermal expansion. $\frac{dn}{dT}$ is the temperature-caused index change. The $\left. \frac{\partial n}{\partial \rho} \right|_T$ stands for the variation of the index change a constant temperature and $\left. \frac{\partial n}{\partial T} \right|_\rho$ is the index change at constant density. The variations in refractive index are governed by the high volume expansion coefficient of the polymer therefore the TOC is negative for most of polymers. Complementary information describing the thermo-optical properties of the polymers can be found in the literature [121].

The thickness and the refractive index are well known for the polymer at ambient temperature, moreover, the influence of the Si substrate with the temperature have been verified. Prior to the TOC measurement of the polymer, we have induced variations on the SiO_2 native layer which did not provide significant variation on the already known polymer parameters. Therefore the thickness native SiO_2 is considered constant. Finally, the polymer is modeled as a dielectric layer with anomalous dispersion (one oscillator). Then, in addition to the already known thicknesses the model parameters are the following:

- Si (TOC values measured and compared with the literature)
- SiO_2 (Considered invariant (2 nm))
- Polymer (One oscillator, Unknown TOC)

Previously to the measurement, we have optimized the set-up in order to reduce all the systematic errors (planarity, wafer displacements...) since they have to be maintained during all the measurement procedure. We have performed multiple measurements at different positions with different input angles as we have done for the Si wafer in order to increase the set of data and reduce the index-thickness correlation. The Fig.3.9 show the acquisition of the ellipsometry measurement I_c and I_s which are directly related to the polarization change. The curve at 25°C and 85°C show a very similar behavior since the small temperature change does not produce large variations in the polymer. In addition we have carried the measurements in normal ambient conditions (Cyan and magenta) and under a nitrogen atmosphere (Blue and red). The fit overlaps each curve.

Even if the model fits the experimental data for the thin film of polymer, it is still a mathematical model. To both validate the model with real physical measurements and reduce the index-thickness correlation we have performed direct index measurements on bulks of UVNIL394. The bulk material is considered semi-infinite since there is no reflection coming from the substrate. Dedicated supports were manufactured to study the index of the bulk material; this supports are done in such a way to obtain good surface roughness and no reflexion from the bottom. The index is obtained directly from the ellipsometer without any further modeling. The dispersion curves for the thin film of UVNIL and for the bulk are shown in Fig.3.10. The different curves of curves were taken along 1 month. It is very delicate to compare the refractive index for a bulk and a thin layer of polymer since they do not have strictly the same physical properties. In addition, we can observe a high variation in the measurements done in the bulk material. This is mainly due to the temperature gradient created inside the bulk which provides a refractive index gradient all the bulk thickness. In addition the metallic bulk support also expands with temperature which increases the noise associated to the measurement. Despite this issues, the measured dispersion on the refractive index for the bulk material and the thin layer were very similar. Thus, we can conclude that our mathematical model used

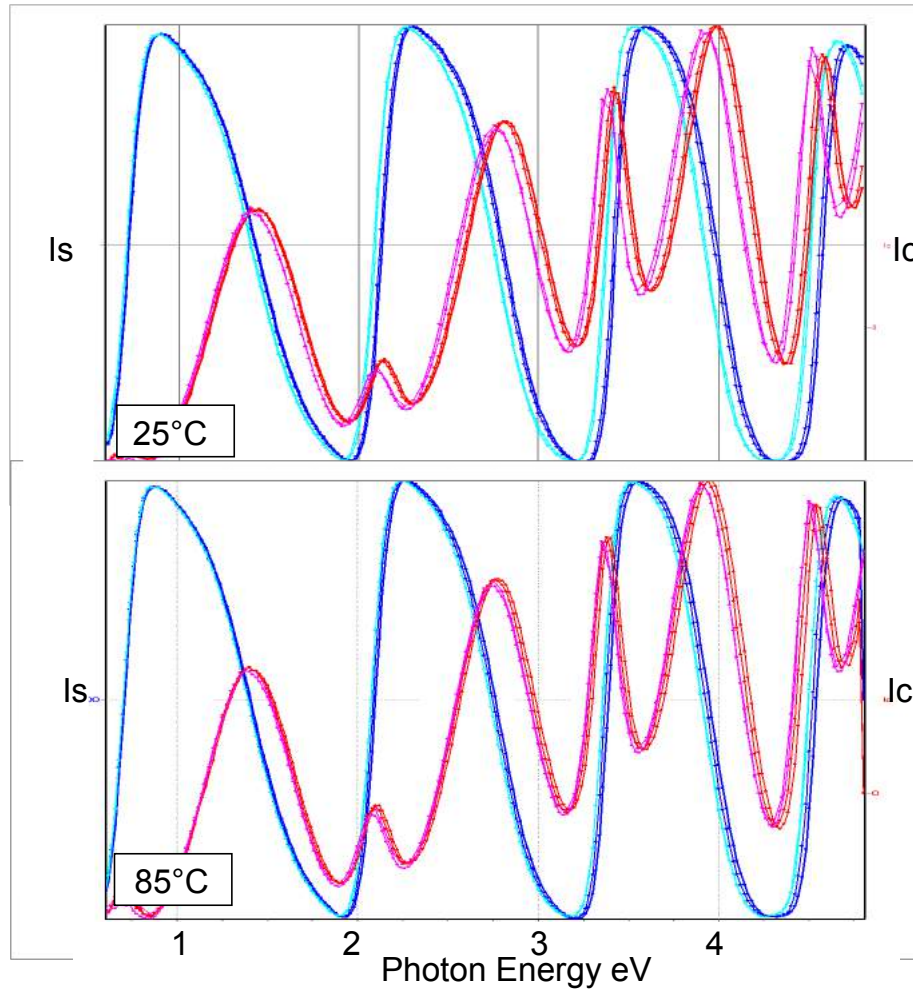


Figure 3.9: Calculated I_c (Bluish) and I_s (Reddish) values for different input conditions, the model fit perfectly the obtained values. The curves are shown for two different wafer temperature 25°C and 85°C . Cyan and magenta are measured at 70° AOI with surrounding air. Blue and red curves correspond to two measurements at 70° AOI with a surrounding atmosphere of N_2 .

to extract refractive index from thin layers of the polymer provides physical results as obtained from the bulk material (no modeling).

Other strategies to reduce the correlation is a combination of mechanical stylus thickness measurements with variable-angle spectroscopic ellipsometry [122]. After numerous measurements we converge towards a TOC of $-2.2 \cdot 10^{-4}$ extracted from the data treatment of the obtained refractive index. The dn/dT could not be obtained with the bulk due to the displacements and variations enunciated before. The uncertainty of the obtained dn/dT is around 10% as obtained with the Si Wafer. The TOC of the Ormocore is also measured but it can also be found in the literature or in the data sheet about $3 \cdot 10^{-4} K^{-1}$.

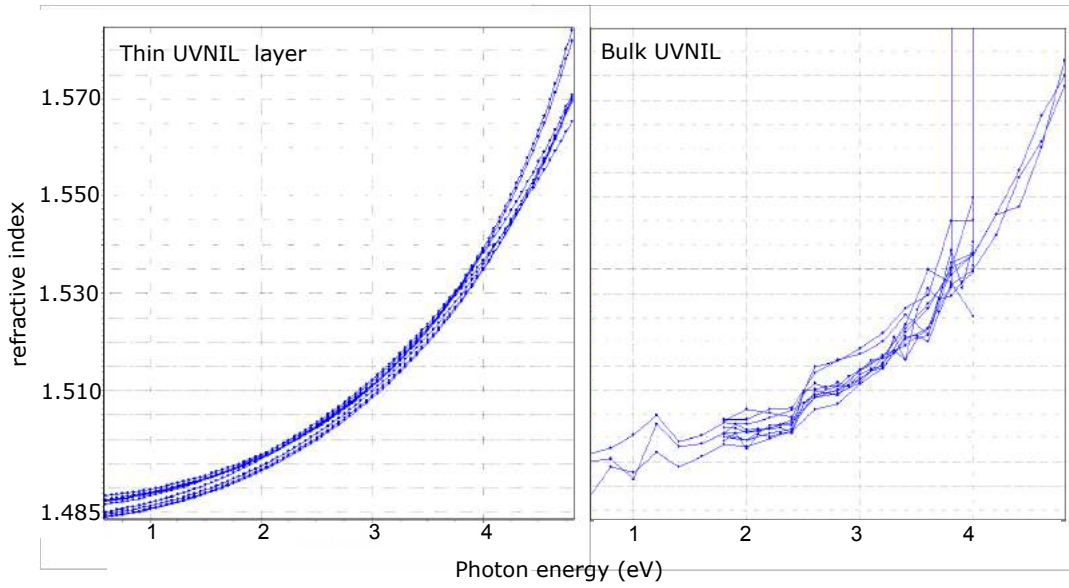


Figure 3.10: Refractive index dispersion for the UVNIL thin film obtained with the ellipsometry model (left). Direct measurement of the refractive index dispersion for the bulk of UVNIL. The similar dispersion trend obtained between the model and the bulk validates our model.

3.3.4 Incertitude associated to the refractive index variation

We must discuss about the incertitude associated to the measurement of the refractive index and how it affects the dn/dT . As shown, there is a noticeable bias between the refractive index of the UVNIL announced ($n=1.52$, $\lambda = 586$ nm) and the obtained values of refractive index (≈ 1.51). It is totally possible to have a biased measure depending the measurement protocol. Typically the ellipsometer with the adequate configuration provides high reproducible results with an error around $\alpha \approx 10^{-3}$ on the refractive index. It is worthy to ask ourself how it is possible to announce refractive index variations ($\Delta n \approx 10^{-4}$) with temperature when the incertitude associated to the refractive index is higher than the announced TOC values ($10^{-3} > 10^{-4}$). This is due how the error propagates around a stable operating point.

The true refractive index n_{true} and the measured refractive index n_{mes} are related by the error during measurement δ as:

$$n_{mes} = n_{true} + \delta(n_{true}) \quad (3.8)$$

This can be written in terms of the relative error α and systematic errors β

$$n_{mes} = n_{true}(1 + \alpha) + \beta \quad (3.9)$$

If we suppose no systematic error $\beta = 0$, the relative error can be expressed as:

$$error = \frac{n_{mes} - n_{true}}{n_{true}} = \frac{n_{true}(1 + \alpha) - n_{true}}{n_{true}} = \alpha \quad (3.10)$$

Therefore, in the case of a measure of refractive index we can suppose $\alpha < 10^{-3}$ Now regarding the variation between refractive index at two temperatures T_1 and T_2 :

$$\Delta n_{mes} = n_{mes}(T_1) - n_{mes}(T_2) = n_{true}(T_1) + n_{true}(T_1)\alpha - n_{true}(T_2) - n_{true}(T_2)\alpha \quad (3.11)$$

Rewriting as in Eq.3.8

$$\Delta n_{mes} = \Delta n_{true} + \Delta n_{true}\alpha \quad (3.12)$$

Therefore, the refractive index difference between two temperatures (Δn_{mes}) is the true variation (Δn_{true}) plus an uncertainty proportional to $\Delta n_{true}\alpha$. As the TOC for polymers is about the magnitude order of 10^{-4} , the error associated to the TOC variation would be around 10^{-7} .

3.3.5 Final observations on the polymer film

We have observed an anomalous thinning of the polymer film, moreover no significant changes in the refractive index were noticed. This unexpected evolution can be due to the evaporation of the remaining solvents inside the resist or due to a progressive strain relaxation of the polymer chains with the temperature. The Fig.3.11 illustrates this behavior which can be highly problematic if a long term use of polymer devices is expected. The values of the CTE directly obtained from the curve remain unchanged about $\alpha = 5 \cdot 10^{-4} K^{-1}$. The values obtained for both CTE (α) and TOC are compared in Fig.3.12 with other polymers showing a good match with other polymers as show the curve extracted from Zhang et al.

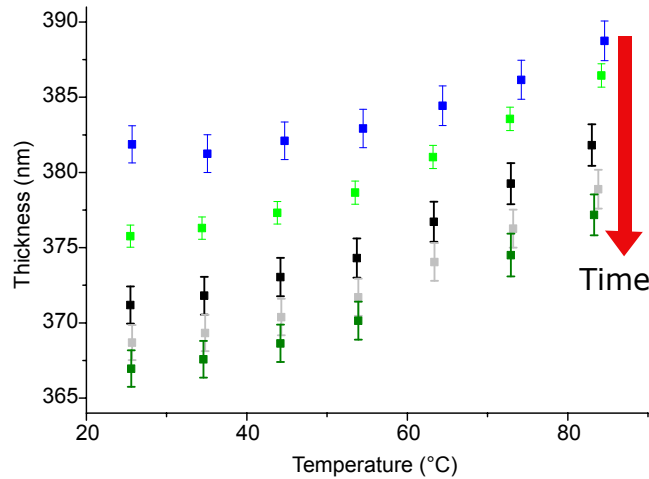


Figure 3.11: We show the thickness versus temperature for the UVN1394 resist. The curves were taken in a row of 5 days. The thickness shows a mechanical hysteresis since the layer does not seem to recover the initial thickness

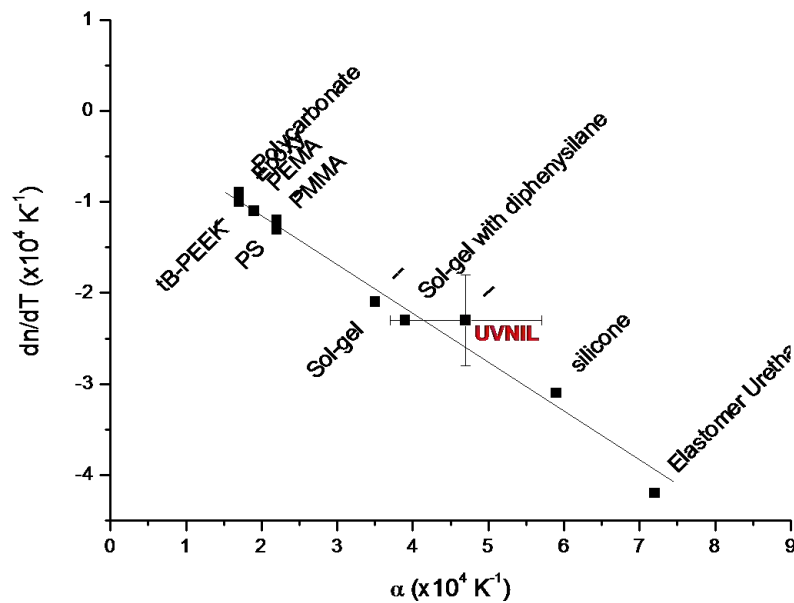


Figure 3.12: TOC versus CTE for different polymers used for waveguide applications. The curve is presented in [123]. We place the NIL UV regarding the behavior of the other polymers.

3.3.6 Effective index measurement with a prism coupler

Ellipsometry is an extremely powerful technique which provides information about the index, the thickness, the reflectance, the extinction ratio and so on. If we want to determine index and thickness uniquely, the prism coupling method is preferred as the bottom layers (e.g., Si substrate) do not contribute to the measurement and the heavy multilayer modeling is avoided [124]. We already have developed an appropriate model to determine the refractive index, layer thickness, and TOC with ellipsometry. Despite the ellipsometry study, our primary interest in the prism coupling technique is to provide feedback about the effective index of the waveguide layer, which is not given by the ellipsometer. Then, we compare the measured effective index with the values obtained by the simulations (MODE solver).

The prism coupling allows a part of the light to travel inside the planar core layer without complex fabrication process, such method can be found in the literature [125]. A high refractive index prism is maintained in close contact against the guiding layer, the gap between the prism and the layer must be shorter than the test wavelength to allow evanescent field coupling. An incident beam reach one facet of the prism, then reflects on the prism-core interface and comes out for the opposite facet. For a discrete set of input angles, some of the light can be coupled via evanescent field to the waveguide layer. The remaining light not coupled inside the waveguide can be collected or imaged at the output. Several dark lines (absence of light) can appear, which correspond to the modes coupled into the prism, the main

interest of this technique is to measure the input angle at which each dark line appears. This method is also known as M-lines, and it can be found in the literature [126]. The Fig.3.13 shows the set-up for the M-lines experiment.

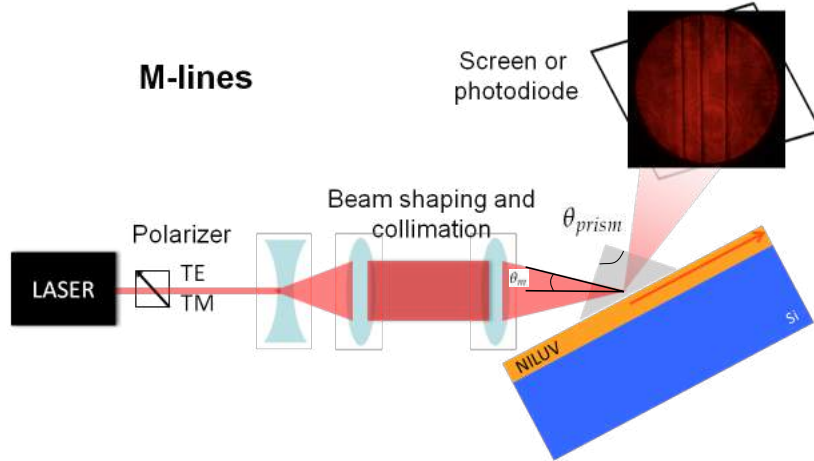


Figure 3.13: The set-up used to visualize the dark modes of the waveguide. The dark lines in the screen correspond to the guided modes into the waveguide.

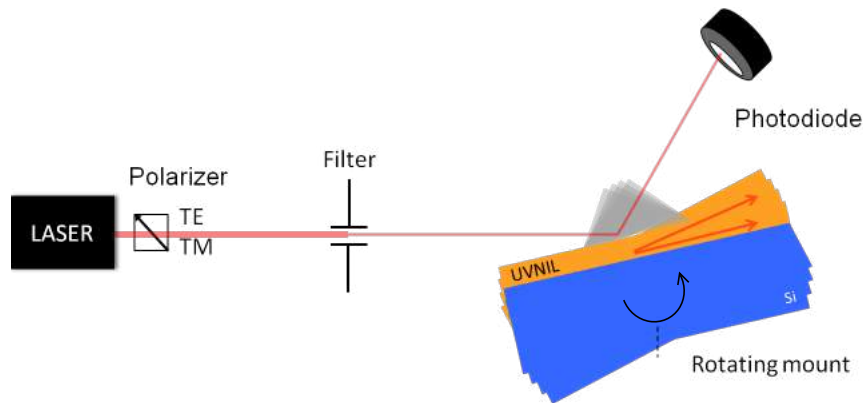


Figure 3.14: The set-up used to measure the coupling angle of the guided modes of the waveguide. The device and the prism are rotated while a Si photodiode collects the reflected light.

Once the modes are observed in the screen with the M-lines technique we proceed to the measurement as shown in Fig.3.14. A collimated laser is used to excite and measure the single modes individually. The input angles are swept with an automated goniometer and the power is collected with a photodiode, both photodiode and goniometer are automated to enhance the data acquisition. We have used several lasers emitting in the visible and a SF11 prism with a refractive index of $n_{prism} = 1.792$ ($\lambda = 543$ nm) and $n_{prism} = 1.778$ ($\lambda = 632$ nm) with a prism angle of

$\theta=60^\circ$. We have tried two polarizations and two different wavelengths. The values of the effective index n_{eff} can be found by directly measuring the input coupling angle θ_m .

We can use the equation:

$$n_{eff} = n_{prism} \sin(\theta_{prism} + \sin^{-1} \frac{(n_{air} \sin(\theta_m))}{n_{prism}}) \quad (3.13)$$

where n_{prism} and θ_{prism} are the prism refractive index and the prism angle θ_{prism} respectively. In the Tab.3.1 we show the data extracted from two measurements of two

Table 3.1: Measured coupling angles with the prism coupling technique. The obtained effective index were calculated with the equation Eq.3.13 and compared with the values obtained with LUMERICAL for the stack of materials.

Laser $\lambda(nm)$	Measures		Calculation		Simulation		$\Delta n(TE-TM)$	
	$\theta_m.TE$	$\theta_m.TM$	$n_{eff.TE}$	$n_{eff.TM}$	$n_{eff.TE}$	$n_{eff.TM}$	TE	TM
543	18.159	17.250	1.468	1.457	1.474	1.465	$5.5 \cdot 10^{-3}$	$7.3 \cdot 10^{-3}$
632	17.517	16.259	1.452	1.440	1.463	1.451	$1.1 \cdot 10^{-2}$	$1.1 \cdot 10^{-2}$
543	18.197	17.288	1.468	1.460	1.474	1.465	$5.2 \cdot 10^{-3}$	$5.1 \cdot 10^{-3}$
632	17.538	16.299	1.452	1.440	1.463	1.451	$1.08 \cdot 10^{-2}$	$1.06 \cdot 10^{-2}$

different slices of the same wafer. The effective index were calculated by using the equation Eq.3.13 and compared with the effective index obtained by Lumerical. The input coupling angles are higher for the TE than the TM as TE is the fundamental mode of the planar waveguide and posses the higher effective index. The experimental values are very similar to those obtained by simulation which are slightly higher. This difference can be due to multiple reasons; it can be mainly due to the exact refractive index set in the simulation as we have did not considered the material dispersion for the calculation of the modes. Moreover, some systematic errors can also be made while setting the normal incidence. Nonetheless, the difference (Δn) between the effective index for both polarizations is constant between the different wafers validating the measurement method.

3.3.7 Conclusions about the characterization

In this section, we have shown the standard fabrication process of polymer waveguides on CYTOP. We have revealed some problems which have to be considered in further works. If tiny gaps (<100 nm) are needed other stamps than thermoplastics should be used to avoid the noticed drifting. X-PDMS soft stamps can be an option despite the fabrication effort needed to manufacture such a stamp. Risk of pattern collapse still will be present. Regarding the characterization, we have developed an appropriate ellipsometry methodology to directly obtain TOC of polymers. This model is tested by comparison with physical measurements, it is valid for other

polymers. However, regarding the further operation of the polymer devices, a stable fabrication process should be found since we evidence the long-term polymer thinning which affect the effective index. This variation is neither addressed in simulation nor considered in this work. Complementarity, we have measured the effective index of the polymer layer with the M-lines method showing a good agreement with the spatial modes, both calculated analytically and by simulations (Ch.2, Fig.2.18).

3.4 Optical characterization of imprinted devices

Here, we present the optical characterization of the grating couplers and ring resonators. First, we discuss the optimal set-up according to the requirements imposed by the visible optical sources. Cleaved waveguides with and without ring resonators were characterized with different fixed-wavelength lasers. Angular acceptance and efficiency are shown as a figure of merit of the grating coupler. Thermal tuning of ring resonators resonance is considered; therefore prior to the temperature tuning of the OMR the influence of temperature on grating couplers is studied in detail. Once the grating couplers are fully understood, the optical characterization of polymer ring resonators is presented and discussed. Other characterization strategies are shown in this chapter which can be implemented shortly.

3.5 Set-up requirements for integrated structure interrogation in the visible range

The optimal source for on-chip spectroscopy must fulfill strict requirements concerning both wavelength and power stability. An additional important characteristic is broadband or tunable-wavelength emission, which can facilitate the real-time scanning of absorption or resonance peaks.

Regarding the input set-up, grating couplers are used to perform light coupling with a slight off-vertical input angle. Since optical fibers can be cleaved to adjust the output beam to the input angle of the grating coupler, they can be a suitable choice to perform the input coupling. Also, this allows the fiber to be nearly in physical contact with the coupler, thus reducing the distance and avoiding large beam divergence. Polarization can be maintained with dedicated fibers (PMF), and commercial lasers are available with output PMF.

However, full sets of tunable, short line-width visible laser modules with a fibered output and which maintain polarization are not yet available. For this reason, to adjust laser beam characteristics, and due to the lack of commercial devices at the aimed wavelengths, the set-up should allow both beam modification and polarization control, with successive fiber coupling reducing the overall system efficiency. As an example, a set-up is proposed in the Fig.3.15 to characterize cleaved waveguides with a grating coupler. The input beam should be shaped with the appropriated

optical systems. At the same time, we must allow selecting different input coupling angles. The output beam is measured directly with a photodiode. The details of the selected optics are given in Sec.3.6. We propose to discuss different input beam possibilities for visible wavelength operation; in the following, We consider important criteria such as broadband emission, wavelength tuning, and integration of the different sources.

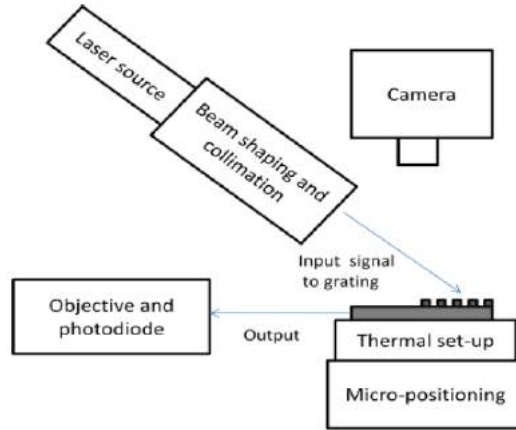


Figure 3.15: Experimental set-up used for the optical characterization of the fabricated structures (taper, grating and waveguide). Input coupling is ensured through the grating and the output light is measured with a silicon photodiode.

3.5.1 LED

Light-emitting diodes (LED) present power stability and a relative large emission spectrum (~ 40 nm) in the visible region. However, high power LED chip footprint (e.g., M530L3d 1 mm) is too large to couple light into visible single-mode fibers (core size ≤ 10 μm), which results in very low coupling efficiencies. In LEDs, light is produced by spontaneous emission from the light-emitting region of chip. Therefore, the generated light presents a low coherence length L_c ($\lambda = 550$, $\Delta\lambda = 40\text{nm}$, $L_c \leq 10$ μm) which can affect the characterization of devices where high coherence length is required. From the radiometric point of view, before exiting the chip, the light generated in this region propagates through different media. The light pattern generated by an LED is the result of a combination of Gaussian-Lambert emission, besides, the light is reflected and modified by the encapsulating lens and waveguide effects. Therefore, as far as the beam quality degrades, the coupling efficiency will be low.

Also, one of the fundamental rules of designing optical systems is that of the etendue or optical invariant. These are related quantities that describe the fact that the product of the source size and its emission angle are at best constant in an optical system. This means that no optical system can make the product of the source size and emission angle smaller without throwing away light. Therefore, in addition to the quality beam consideration, the small collimated LED beam will provide

unacceptable low output power with large optomechanical set-ups. LED coupling would be a better option if large waveguides were considered (optofluidic chips, multimode optical fibers).

3.5.2 Solid Lasers

Laser Diode

Output fiber solid-state lasers and diode lasers produce high-quality beams. The laser linewidth should be chosen carefully if intended for visible spectroscopy applications. Between the available laser diode sources, green laser emission is produced by non-linear conversion (GaAs) or by direct emission of GaN [127] [128]. Different techniques to achieve narrow-linewidth emissions, such as the distributed feedback (DFB) or distributed Bragg reflector (DBR) feedback techniques, are well established for GaAs-based laser devices; however these techniques are still under development for GaN-based diode lasers. Green laser diodes present relatively large linewidths (1-2 nm), which is due to the envelope of the lasing modes. However, if a single frequency is analyzed with a spectrometer, the power of each mode potentially present endless power variations due to competition between the lasing modes. Therefore, this kind of laser diode should be avoided if we are interested in single-frequency power measurements. None of these solutions are wavelength tunable, single frequency and tunable GaN-based laser diode are still under development, recent advances have shown output powers up to 500 mW with a tunable range of 2 nm [129]

DPSSL

Single-frequency emission can be achieved with diode-pumped solid-state lasers (DPSSL) or with a laser diode with a high mode suppression ratio (MSR) where one mode is clearly dominating. By this way, the obtained linewidth can be reduced to several MHz. Unfortunately, this solution does not allow for wavelength tuning.

VCSEL

Alternative sources of interest are VCSEL or organic lasers. VCSEL lasers can provide green emission by intracavity second-harmonic generation [130]. They allow for 2D hybrid integration, representing a realistic future alternative to couple light with an off-vertical angle [131].

3.5.3 Supercontinuum

Simultaneous access to multiple wavelengths can be achieved with supercontinuum generation [132]. In this kind of source, a broadband spectrum is generated inside an optical fiber due to non-linear effects. The optical fiber is a single-mode photonic crystal fiber pumped by a mid-infrared laser. The emitted spectrum is broadband in the visible region and the infrared. Output beam can be shaped as another type

of laser with collimators and beam polarizers. The main drawbacks of these sources are the elevated cost and the need for post filtering in order to select the wavelength of interest. The output power per wavelength is usually relatively low for supercontinuum sources, with a cost below 10k. On-chip generation of supercontinuum has already been reported, but this usually requires external high power pump lasers.

3.5.4 Other sources

Organic lasers can provide on-chip tunable visible emission under optical pumping; however, commercially available devices are still under development [133]. While lasers based on parametric oscillators and liquid dye lasers are visible tunable solutions, these options are costly and bulky compared to other types of sources discussed in this section.

In the Tab.3.2 we show an overview of the different sources considered. None of the presented sources are wavelength tunable excepting both organic and GaN laser diodes which, from our knowledge, are not commercially available. For our study, we have tried different solutions. We have used a doubled laser diode with a relatively large bandwidth, a DPSSL and a supercontinuum laser. VCSEL and organic laser can be good options for future integration, however, this topic is not covered in this work.

Table 3.2: Considerations on the visible input beam source for microring resonator applications.

Group	Beam	Frequency	Portability	Power Range
LED	Bad	Broad	Very Good	W
LD	Good	Multimode	Good	W
DPSS	Good	Single frequency	Medium	W
Supercontinuum	Good	Broad	Medium	μ W
VCSEL	Good	Single frequency	Very good	mW
Organic	Good	Single frequency	Good	μ W

3.6 Experimental set up: Grating-waveguide-photodiode

Optical efficiency characterization of the grating couplers patterned onto the sub-micron waveguides has been made using an OXXIUS LBX-515 (frequency doubled GaAs) laser diode emitting 3mW at 507 nm with an spectral width of 2 nm. The 4 mm long taper allows efficient mode size conversion to the submicron waveguides. A TE-polarized laser beam with a spot size of 21 μ m FWHM is achieved from the fiber. The complete setup is shown in Fig.3.16 complementing Fig.3.15. The beam is shaped using triplet fiber optic collimator with a very low divergence(0.09°). Then, a beam splitter with a half-wave plate selects the TE-polarization and an output lens focuses (10 mm) the spot on the grating. The focal distance is chosen to allow a

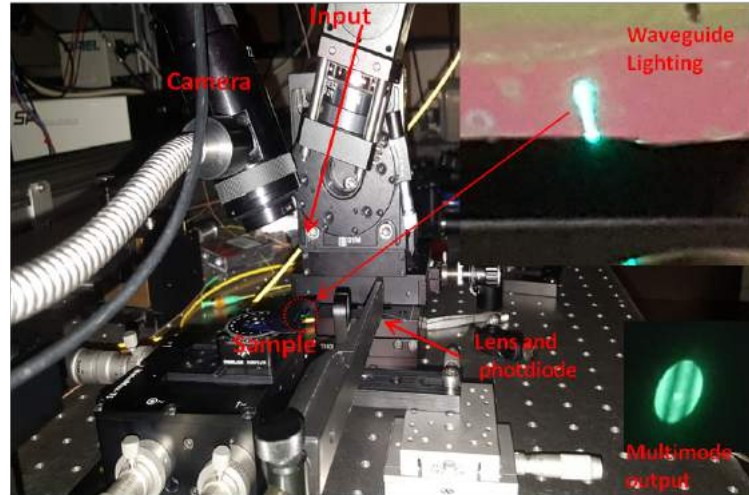


Figure 3.16: Experimental set-up used for the optical characterization of the fabricated structures (taper, grating and waveguide). Input coupling is ensured through the grating and the output light is measured with a silicon photodiode.

small spot size and a comfortable working distance. Smaller spot size can enhance efficiency, however during angular acceptance characterization is important to remain with an almost incident plane wave without adjusting the focal point at each time. From Gaussian optics this condition determines the Rayleigh distance which is estimated to be $z_r \simeq 2.5\text{mm}$ for our optical configuration. The whole input light injection assembly is mounted on a goniometer with a minimum angular step of 0.2° , which allows to adjust the input angle of the beam onto the grating. Due to the large thermo-optic coefficient of polymer materials and to avoid variations of the coupling efficiency of the grating as a function of temperature, the samples were placed onto a suitable thermoelectric cooler in order to carefully control the device operating temperature. The output signal is collected at the end facet of the cleaved waveguide through a high numerical aperture (X50, $\text{NA} = 0.8$) microscope objective and measured with a silicon photodiode from Ophir Photonics, while a long working distance camera allows beam spot imaging. Slight variations of the bottom cladding thickness can alter coupling efficiency. This is due to the modulation of the coupling strength given by the interferences between the upward and the downward wave into the cladding. This modulation is well-known in SOI photonics where cladding thickness is precisely controlled during plasma-enhanced chemical vapor deposition of the SiO_2 layer. To investigate on such an effect in our structures, three different samples have been fabricated with CYTOP cladding thicknesses of 520 530 and 540 nm obtained at corresponding spin coating speed of 1200,1100,1000 rpm. Thickness measurements were reliably obtained by ellipsometry. With the spectrometric ellipsometer Horiba Jhon Yvon. Experimental results of total transmission are plotted in Fig.3.17 and summarized in Tab.3.3 as a function of the CYTOP cladding thickness. Regarding the obtained results the optimum CYTOP thickness would be 520 nm.

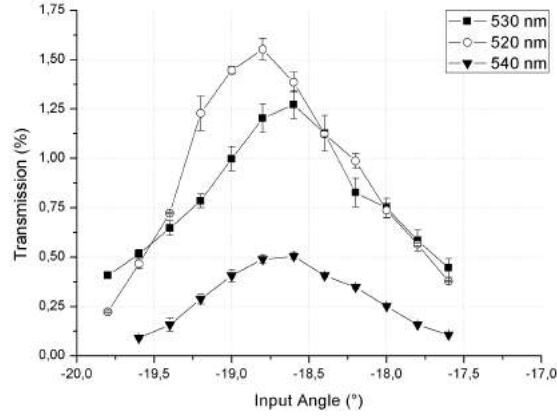


Figure 3.17: Efficiency versus input angle for three different CYTOP claddings. Angular width is extracted at FWHM.

Table 3.3: Experimental values of angular width ($\Delta\theta$), coupling angle (θ_c) and efficiency (α) for samples versus different thicknesses of CYTOP. The coupling length is determined analytically.

CYTOP spin speed (rpm)	CYTOP thickness (nm)	$\Delta\theta$	θ_c	Γ	$L_c(\mu m)$
1200	520	1.51	18.8	1.55	6.5
1100	530	1.57	18.6	1.27	6.2
1000	540	1.25	18.6	0.5	7.8

Coupling length is found directly from the equation $\Delta\theta = \lambda / \pi \cos\theta L_c$ which gives an approximation in the case of semi-infinite gratings.

In order to compare these experimental results with the predicted ones, two-dimensional FDTD simulations have been performed to study the optical efficiency of the grating coupler. Since waveguides only contribute to the overall propagation loss they are not considered to study the coupling efficiency. For these simulations, it is assumed that the grating region is illuminated by a Gaussian beam. The simulation conditions are the following:

The waist radius of the laser beam is assumed to be equal to $10.5\mu m$ at 507 nm .

The divergence of the beam at the focal point is set to the theoretical limit $\gamma = 0.83^\circ$ for the given beam parameters.

The focus of laser spot is located at $10\mu m$ the x position from the grating edge. Fig. 3.18 gives the simulated grating coupler coupling efficiency versus CYTOP thickness for the experimental input parameters. The coupling efficiency variations are due to upward and downward waves interferences occurring into the cladding. Increasing the reflection at the Si surface (e.g with metallic coatings) could enhance this effect. The overall input efficiency is in agreement with other polymer grating couplers found in the literature. In [134], the input efficiency of the measured grating coupler with a single diffraction order was 67%.

From Tab. 3.3, one can conclude that the measured coupling angle is equal to $18.7 \pm 0.1^\circ$ whatever the CYTOP cladding thickness is, which is in very good agreement

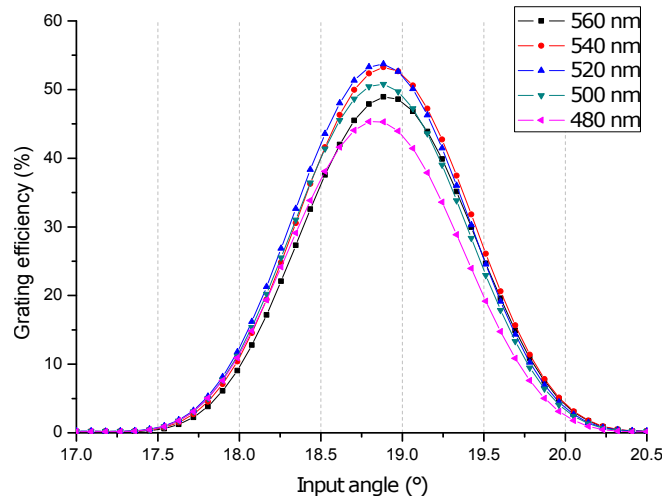


Figure 3.18: Simulation results of optical efficiency versus angular width for different CYTOP cladding thicknesses when considering only the grating (without waveguide). The input light corresponds to a focused Gaussian beam with $11 \mu\text{m}$ waist radius and 0.83 beam divergence. The center wavelength of the beam is 507 nm and the angular width at FWHM is 1.23° .

with the predicted 18.9° value obtained from simulations. The slight difference is probably due to variation of the RL, but despite this slight variation, the three samples present the same coupling angles thus proving the repeatability of the imprint process. Grating couplers show angular acceptance width up to 1.57° . These experimental results are slightly above those predicted by simulations, and these differences are attributed due to the spectral width of the source and the divergence of the real beam.

The transmission efficiency obtained through experiments for each structure present larger differences than those predicted by simulations. The differences between the plotted curves probably come from the irregular cleaving of each waveguide. In addition, these variations are larger than the predicted variations obtained from simulation. Besides irregular cleaving process, the efficiency shift shown in Fig.3.17 could be related to structural defects occurring along the waveguide (e.g., sidewall detachment, stitching field errors during electron beam patterning...). Besides, homogeneous thin layers obtained by spin coating with thicknesses variations below 4% on the full wafer are extremely challenging. Maximum measured transmission efficiency for the fabricated devices is 1.55% that represents 18 dB of total transmission loss. By comparison, higher losses (21.5 dB) have been measured in shorter polymer transmission lines on SiO_2 claddings as reported in [47] [135].

We believe that the estimated losses of our structures could be reduced both by improving the waveguide structural defects and the quality of the optical output facet. The total loss depends on the quality of the facets grating coupler efficiency can be estimated with reproducible output structures. This can be estimated from

devices with two grating couplers for the input and output respectively. We measured a device of the C type (Double grating). A double grating structure is measured collecting the output with a multimode optical fiber. As we work with two gratings, we can estimate the efficiency of the coupler. The best efficiency of this transmission line of 6 mm is -26.19 dB (0.0024%) at the output of the fiber. Supposing the coupling loss for a grating-fiber coupling (-1 dB) and the typical propagation losses in polymer waveguides -4.5 dB/cm. Grating coupler efficiency is estimated to be around 8% for each grating coupler. Compared to the simulations, several reasons can be attributed to this efficiency: the inhomogeneities of the etch depth on the edges of the grating, the subsequent aberrations of the optical systems, the deviations from the theoretical beam divergence and a low quality input beam can be considered as a main sources of experimental deviations which negatively affect the measured efficiency.

3.7 Characterization of ring resonator at fixed wavelength

Tunable visible source is bulky and expensive if no broadband source is available we must study alternative characterization strategies. These strategies usually rely on refractive index modification of the waveguide materials while the input laser wavelength is maintained constant. When the optical path matches an integer multiple of the laser wavelength we fulfill the resonant conditions and the built-up factor is maximized inside the ring. One straightforward method consists of heating the device to modify its refractive index due to the variation of both the electronic polarizability and thermal expansion. The ratio of refractive index variation is given by the thermo-optic coefficient of the material which is not always perfectly known since process flow and the material disposition (bulk/layer) can affect the optical properties. refractive index variation of the cladding can also be achieved with liquid crystals properties, for example, ring resonators were fabricated onto a liquid crystal substrate, the refractive index of the substrate is tuned electrically allowing for high Q ORR characterization [136] [137]. Although this can not be done in our particular case (CYTOP cladding), we can tune the cladding of ORR inducing a refractive index variation in the top cladding. This can be accomplished by mixing over the ring resonator liquids with different refractive index with microfluidic handling [138], or by controlling the ration of ring covered by a liquid [139]. In this section, we show and review the principles relying on the characterization of the imprinted ring resonators at a fixed wavelength. First, we discuss temperature tuning of ring resonances as well as the influence of the temperature in the grating coupler. We show the experimental characterization of grating couplers and ring resonators with temperature.

3.7.1 Thermal resonance tuning of ring resonators

As stated before, an increment in the temperature brings a modification of the waveguide refractive index. Semiconductor and SiO_2 waveguide resonators can be successfully characterized with a temperature sweep. However, polymers are organic materials and they present more important CTE than other dielectrics which has to be taken in account. As discussed during the ellipsometry characterization (Sec.3.3) polymers present negative thermo-optics coefficient due to the major influence of the CTE over the polarizability constant. An increment in temperature implies a decrease in the RL with a CTE around 10^{-4} for most of polymers. As the ring is heated, supposing uniform expansion, each part expands by the same amount in every direction therefore the ring radius gets larger. The dependence of the effective index and the ring radius with temperature can be included in the ring resonator equation for two resonances m and $m - 1$:

$$2\pi R(T_1)n_{eff}(T_1) = m\lambda_{res} \quad (3.14)$$

$$2\pi R(T_2)n_{eff}(T_2) = (m - 1)\lambda_{res} \quad (3.15)$$

Where n_{eff} is the effective index, λ_{res} is the resonance wavelength and R is the ring radius. The ring parameters are set for two different temperatures T_1 and T_2 with $T_2 > T_1$. Therefore due to the negative TOC of polymers $n_{eff}(T_1) > n_{eff}(T_2)$. The family of m -curves are plot in Fig.3.19 The modulation of effective index induced by

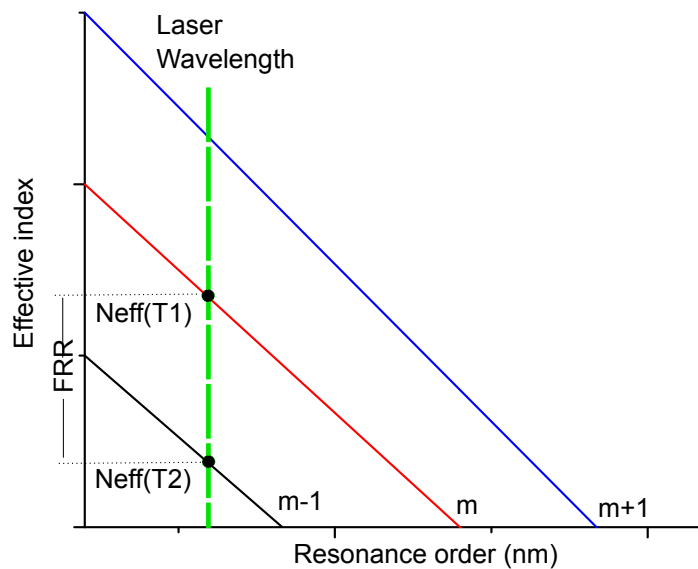


Figure 3.19: The increase of device temperature implies a reduction of effective index proportional to T and the negative TOC of the polymer. The temperature variation from T_1 to T_2 allows us to modify the optical path between $n_{eff}(T_1)$ and $n_{eff}(T_2)$. In both points the ring is in resonance with the laser wavelength.

temperature allows to sweep between resonance orders. As the T raises the effective index diminishes, the optical path of the ring is tuned until the device is in resonance

with the laser wavelength. The refractive index separation between two adjacent resonances ($m, m-1$) is called the Free Refractive Range (FRR) in analogy to the Free Spectral Range (FSR). The system of equations can be reduced as follows:

$$n_{eff}(T_1) = \frac{R(T_2)m}{R(T_1)(m-1)}n_{eff}(T_2) \quad (3.16)$$

Consider the thermal expansion of the radius $R(T) = (1 + \alpha\Delta T)$:

$$\frac{n_{eff}(T_2)}{n_{eff}(T_1)} = \frac{(m-1)}{m(1 + \alpha\Delta T)} \quad (3.17)$$

This is the cross-product which relies the ratio of the effective index required to sweep a full FRR (at least two resonance peaks). As shown, it depends on the resonance number m and the linear expansion of the ring. We can also rewrite the equation in function of the laser resonant wavelength:

$$2\pi(R(T_1)n_{eff}(T_1) - R(T_2)n_{eff}(T_2)) = m\lambda_{res} - (m-1)\lambda_{res} \quad (3.18)$$

$$n_{eff}(T_1) - (1 + \alpha\Delta T)n_{eff}(T_2) = \lambda_{res}/(2\pi R(T_1)) \quad (3.19)$$

The FRR strongly depends on the CTE, if CTE is large the difference between the effective index also will. Wavelength is directly proportional to the FRR while the ring radius is inversely proportional. Therefore large radius contributes to reduce the FRR.

We illustrate an example to estimate the FRR considering the values for a ring made of Ormocore ($n=1.56$). The simulations of the ring waveguide with a 50 nm of RL indicates an effective index of approximately $n_{eff}=1.4$. Considering a ring radius of $15\mu m$ at $\lambda = 532$ nm, if we set these values in the ring resonator equation Eq.3.14 we obtain $m=248$. Once we have the resonance order, we can calculate the FRR with the Ormocore CTE given in the data-sheet ($CTE=10^{-4} K^{-1}$). Supposing a moderate $\Delta T = 50^\circ$ With the equation Eq.3.17 we obtain a FRR=0.0126.

Once the FRR is estimated we have to discuss if we are able to sweep at least one resonance peak. The effective index variation with temperature is proportional to the polymer TOC. It can be studied as an averaged TOC considering the the confinement factor in the different waveguide layers. The equation can be written as follows for small temperature changes:

$$\frac{dn_{eff}}{dT} = \Gamma_{cladd} \frac{dn_{cladd}}{dT} + \beta_{core} \frac{dn_{core}}{dT} \quad (3.20)$$

Where Γ_{cladd} and β_{core} are the confinement factor of the cladding and core respectively. As both materials have different TOC, this expression stand for the fraction of power "seeing" each material change. However, determining accurately the TOC of the different polymer is very complex and very dependent of the material conditions (composition, surface state, aging). However we can estimate approximately

the achievable variation on effective index with temperature. The value of the TOC for the Ormocore can be found in the datasheet or the literature ($-3.2 \cdot 10^{-4} K^{-1}$). If we consider the core confinement factor of a rectangular waveguide of Ormocore as $\Gamma = 0.65$ (Sec 2.8, Fig. 2.35), we obtain $\frac{dn_{eff}}{dT} = -2.1 \cdot 10^{-4} K^{-1}$ applying a reasonable $\Delta T = 50^\circ C$ we can obtain a $\Delta n_{eff} = 0.0105$ being enough to sweep at least one resonance peak. The contribution of the cladding is neglected in this case due to its lower $dn/dT = 10^{-5} K^{-1}$.

These values are extremely approximative, first the TOC of polymer are complex to obtain as discussed during the ellipsometry measurements. The determination of the TOC present important variability depending on the exact composition and processing parameters of the polymer layer. Also, the effective index seeing by the resonator waveguide depends on the inhomogeneity of the RL since the effective index seeing by the wave is an average index of all the waveguide long rather than a local effective index at fixed dimensions. Besides, no information is found in the datasheet about the dn/dT extraction of the polymer (bulk/thin layer). Despite this is a rough estimation, it is enough to sweep almost a complete FRR with thermal tuning.

3.7.2 Effects of temperature on the set-up

Increments in temperature can have extremely negative effects contributing to fiber-device misalignment. For example, aluminum is usually chosen for optomechanical manufacturers for practical reasons. Aluminium and other metals has a CTE around $10^{-5} K^{-1}$. If opto-mechanical set-ups consist in several blocks and supports, variations of 1 degree in 10cm of metal can produce optical fiber misalignment around several microns. Device temperature and room temperature should be stabilized to avoid this concerns. If the in-and out-coupling is performed with optical fibers, the discussed problems will be more pronounced. In this case a solution could be to put in contact directly the optical fiber facet with the optical waveguide. Slightly movement of the wafer would not greatly affect the measurement. However if engineered optical fibers are used the physical contact can cause damage to the fiber.

Microheaters remain one of the best solutions to locally heat waveguide devices limiting the expansion of the wafer and the set-up. If no clean room facilities are available thermo electric coolers are a fast and well understood devices to control the wafer temperature. However, thermo-electric cooler also expands with temperature. We have observed lateral shift of $30\mu m$ on the TEC corner while the temperature is swept 50° . This will be enough for complete misalign the grating and the input beam. The bottom part of the TEC must be thermalized in order to evacuate the calories while avoiding further expansion of the set-up. This can be achieved with refrigerant-filled copper coil which is in direct contact with the thermoelectric cooler. In order to limit the additional layer of materials (which will expand and contract) we recommend to put directly the DUT onto the TEC. Another important thermo mechanical effect affecting the wafer is the thermal gradient which

can cause mechanical stress and strain. One of the main observed strain effect is the wafer bending due to the temperature. If a temperature gradient exist there will be a gradual expansion along the wafer thickness. This implies different expansions per unit cube of material on all the wafer thickness producing undesirable bends and movements of the wafer. Several strategies can be proposed, of course if microfabri-

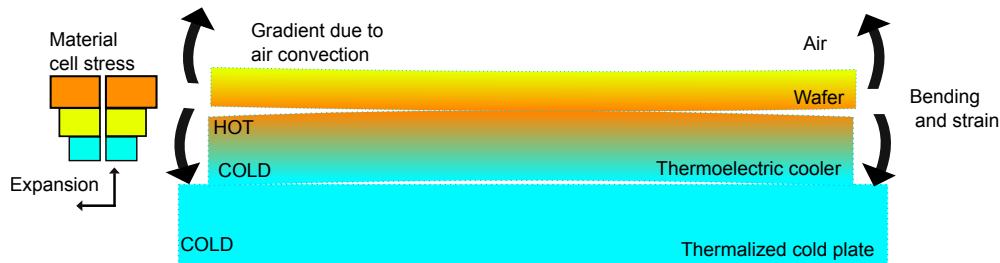


Figure 3.20: Thermal gradients create stress in the set-up and wafer which implies misalignment due to device expansion and wafer bending.

cated resistances are placed near to the ring resonator, all this effects will be limited. However additional fabrication steps for optical characterization are expensive and not application oriented. Other mechanisms of heating consist in reducing by heating trough convection. Air flow convection can be chosen however usually air flow provide vibrations which emphasizes the misalignment and the stability of the measurement. Lamps can be an option however dedicated set ups should be conceived to heat the device from the back face ensuring that the photo diode does not see the IR radiation which can alter the measure. Also if the global support is heated with IR the whole mechanical set up will also expands. There is not optimal solution to the wafer and set-up expansion. The grating coupler minimize power drop caused by thermo-mechanical misalignments with the output power being directly measured by a photodiode.

3.7.3 Thermo-optic response of polymer grating coupler

The optical transmission line consist in a grating coupler with a straight waveguide and a ring resonator, the used polymer is Ormocore which has a higher refractive index 1.56. The devices were imprinted with the same master stamp and cleaved as the devices presented in Sec.3.6. The aim of this study is to characterize the resonance of a microring resonator with temperature, inducing a thermo-optic change of the refractive index due to the thermal expansion. Even if this set-up minimises the effect of the misalignment, grating couplers are also affected by thermal expansion, therefore we have to analyse the coupler response to temperature in order to decorrelate the signal from the grating and the ring resonator. For this characterization, we use the same set-up shown in the characterization of UNVIL devices. We have replaced the OXXIUS laser diode for a DPSS laser in order to work with a single frequency at 532nm.

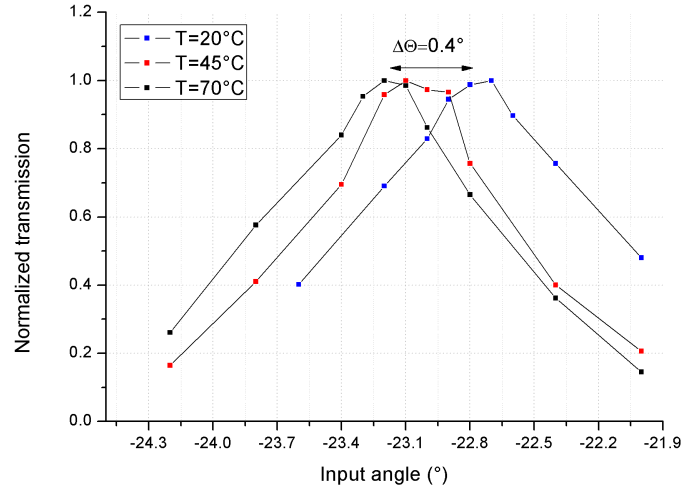


Figure 3.21: Efficiency versus input angle for three different temperatures. Measures were taken at $\lambda = 532nm$. The optimal input angle shift to the more negative angles (lower refractive index).

The measurement of the angular acceptance bandwidth is repeated for 3 different temperatures, 70°C 50°C and 20°C as ambient temperature. As the TEC heats the device and the support expands gradually trending to a set-up alignment loss. Then, optimal coupling position must be set up at each point of the curve to ensure that the powers variation comes from the grating coupler and not from the set-up. This is done manually for each 2 degrees.

In Fig.3.21 we can appreciate a negative shift of the optimum coupling angle when the temperature is increased. Optimum coupling angle is determined by the effective index of the grating and the pitch. The effective index of the grating is approximately $n_{grat}=1.446$ and its obtained directly from the grating equation $\sin(-22.6) = n_{eff} - \lambda/\Delta$. This is in agreement with the estimation of the grating effective index from the LUMERICAL solver. The effective index at groove level is $n_{eff,groove}=1.4$ while the average effective index for a 0.5 form factor grating with an air/Ormocore index contrast is $n_{grat} = (n_{eff,layer} - n_{eff,groove})/2 = 1.43$.

Prior to the thermal sweep, the first step is to set the optimum coupling angle. However, when the temperature raises, a small input angle offset can have noticeable variations in the output efficiency. For a fixed coupling angle, when the device is heated the output power will change depending the sign and the magnitude of the offset. We can explain the variations of efficiency in terms of the couple of parameters angle and temperature as summarized in Fig.3.22.

The characterization set-up is calibrated to obtain the optimal efficiency $\eta(\theta_1, T_1)$ (c point). When the temperature raises from T_1 to T_3 the efficiency decreases. If the system is set-up at the initial temperature and a different coupling angle $\eta(\theta_3, T_1)$ (point a) an angle variation from θ_3 to θ_1 will restore the initial efficiency following the draw *abc* line. The same applies for the other configurations. If the optimal efficiency is found at $\eta(\theta_3, T_3)$ (point h), when temperature decreases from T_3 to T_1

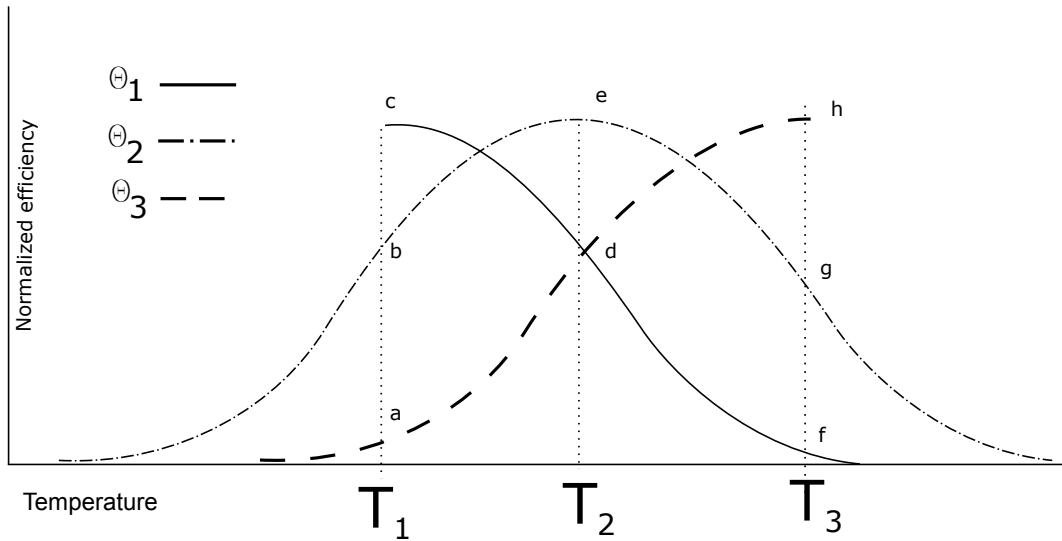


Figure 3.22: Draw of the angle-efficiency curve for different temperatures. If we consider the curve at 20°C we can see how the efficiency will evolve for three different coupling angles.

the efficiency decreases. Angle variations will flow the line fgh . A particular case occurs when we set $\eta(\theta_2, T_2)$ as we will find the optimum efficiency at T_2 . Similarly, When varying the coupling angle around θ_2 the efficiency will oscillate following the trajectory designed as ded .

Now, we analyze the different cases adding a slight angle offset to the optimum coupling angle at ambient temperature. Considering $\theta_{T=20^{\circ}} = 22.6^{\circ}$ and depending on angle offset we can distinguish several cases by comparison to the Fig.3.21:

- There is no offset ($\Delta\theta = 0^{\circ}$). Any change in temperature implies getting out from the optimal coupling condition, thus the output power drops.
- If a small positive shift is applied ($\Delta\theta=+0.2$, $\theta_{T=20^{\circ}} = -22.4^{\circ}$) we enhance the power drop if temperature is increased.
- A shift of $\Delta\theta=-0.2$ ($\theta_{T=20^{\circ}} = -22.8^{\circ}$) an up-down efficiency variation since we move to higher temperature operation points. The input coupling angle corresponds to an intermediate temperature (45°C). Therefore when temperature is increased from 20 to 70 degrees, the optimal efficiency is reached at the middle of the temperature sweep.
- If large positive shifts are applied ($\Delta\theta=-0.6$, $\theta_{T=20^{\circ}} = -23.2^{\circ}$). Displacing the optimal coupling point to higher temperatures. Therefore the power transmitted at ambient temperature will be low and it will increase reaching an optimal value

The problem relies on the characterization experience, as we do not know accurately where are the optimal operation point for each pair of angles and temperature.

In reality, we set an approximate coupling angle, then, controlled variations in temperature will indicate how far from the optimal position we are. These variations were measured as shown in the Fig.3.23.

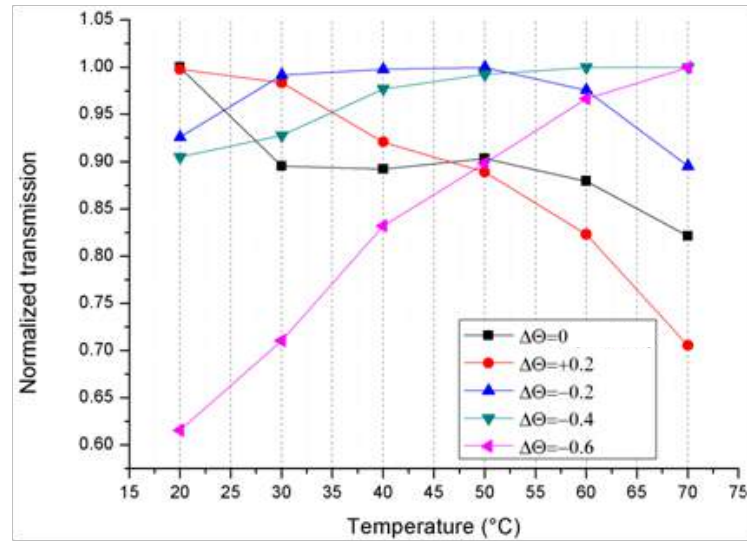


Figure 3.23: Power variation versus temperature for different angle offset. The offset is applied to the optimum coupling angle at $T=20^\circ$. As the offset is higher the slope of the curve is larger.

We set the optimum operation point $\eta(T_1 = 20^\circ\text{C})$ at the optimum coupling angle ($\Delta\theta = 0^\circ$). When the temperature raises we observe a decrease in the efficiency about 15%. If we apply an offset ($\Delta\theta \neq 0^\circ$) from this operation point and we increase the temperature we can observe efficiency drops up to 40% for angle offsets up to 0.6° . We should note that for an offset of -0.2° we observe an up and down trend, because the input angle correspond to its optimum value at approximately 45°C which is the mid-point of the temperature span. For higher temperatures the power starts decreasing. Despite the difficulty to exactly get the optimum input coupling angle at a concrete temperature, we should minimize the offset of the input coupling angle in order to work with tolerable power variations which do not hide ring resonances.

The sign of the angle shift must be discussed, we observed a shift to positive coupling angles when the temperature is increased. Thermal expansion contributes to both decrease the refractive index ($\text{TOC} < 0$) and expand the grating geometry. More negative effective index implies more negative coupling angles regarding the grating equation. However, larger periods implies more positive coupling angles. The final shift is determined by how really the grating expands as certainly it does not expand homogeneously in all the directions. Further discussions can be addressed regarding the anisotropic expansion of imprinted layers of polymers or studying the cross-linking inhomogeneities which can increase the anisotropic behavior. However this discussion is out of the scope of this thesis.

3.7.4 Thermo-optic characterization of ring resonators

As far as we understand how the power changes due to the grating coupler, we can identify power variation due to resonances more efficiently. Using the same set-up, we can characterize microring resonators, however since temperature raises, the set-up alignment is slightly altered. So for each measurement the set up is manually realigned to compensate wafer movements. The temperature is swept from 16°C to 70°C and, from 70°C to 16°C to check if the initial transmitted power is found preventing undesirable hysteresis effects. This adjustments and sweeps make the measurement extremely time consuming. An Ormocore ($n=1.56$) ring with $R=15\mu m$ and $RL\approx 50$ nm were measured with the DPSS laser ($\lambda = 532$ nm) at the optimum coupling angle at ambient temperature. The cleaved waveguide allowed the measurement of the transmitted power, as we have done with the waveguides with a single grating coupler. The Fig.3.24 shows sets of measurements carried on the same device.

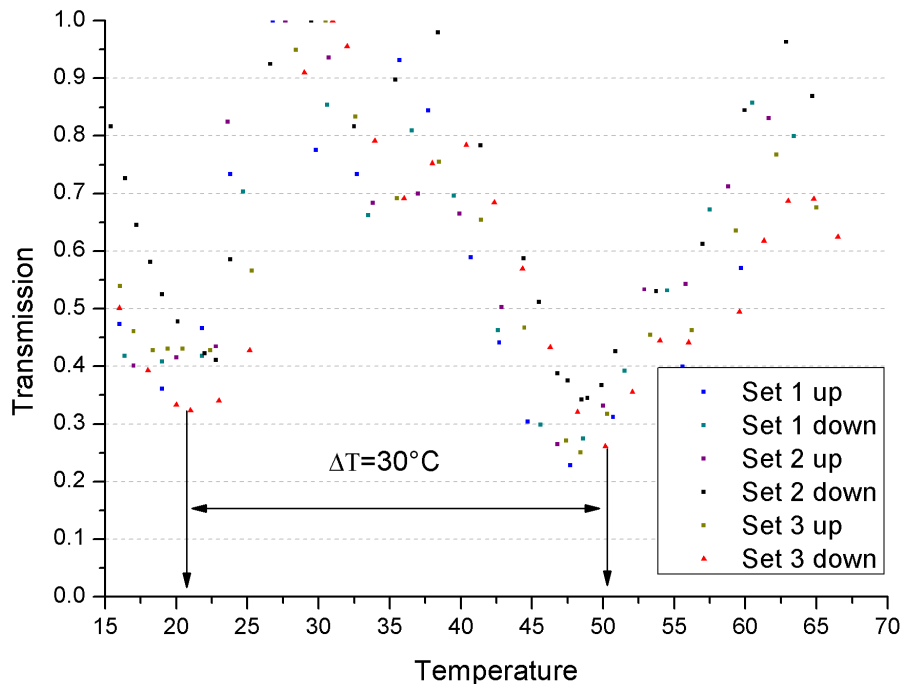


Figure 3.24: Transmission spectrum of a Ormocore ring resonator at a fixed wavelength. The temperature tuning allows for refractive index variations to observe the filtering operation of the all-pass ring resonator.

We can reveal several problems at the extremes of the applied temperatures. Cooling temperatures were stopped at 16°C, since the wafer tends to cumulate humidity, which can be absorbed by the polymer [140] producing drifts in the effective index. In the other hand, high temperatures can lead to polymer aging and volatile compound to evaporate (humidity), then thermal cycles would force the polymer

between these regions, larger scan temperatures are thus not recommended. Thermal expansion contributes to the misalignment; manual adjustment is a temporary solution to test devices but not a large-scale method with integration perspectives. Besides, this tuning method produce sear stress between the surface of the polymers which is enhanced by the large CTE of the polymers Polymers also have internal stress created by the imprint process, remaining solvents, and they swell in the presence of humidity.

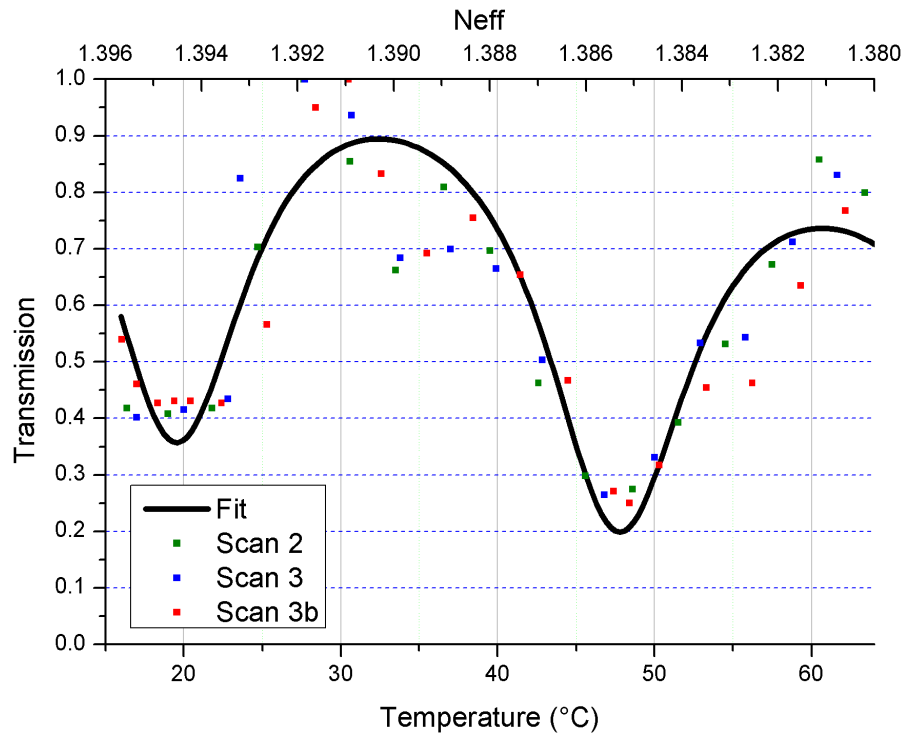


Figure 3.25: Transmission spectrum of a Ormocore ring resonator a fixed wavelength. The black curve fits the behavior of the ring resonator. The FRR found is 0.011 with an TOC close to $3.3 \cdot 10^{-4} K^{-1}$.

Although the large dispersion observed, we can extract the ring parameters with curve fitting. In the Fig.3.25 we plot several set of measurements to perform the fit to the ring resonator equation. Thus, from Eq.2.7 we obtain: $a=0.65$ and $r=0.42$ resulting in a quality factor of $Q \simeq 1000$. The obtained quality factor is reasonable comparing to the simulations presented in Fig.2.34. The value obtained experimentally is lower than the value obtained by simulations probably due to the material propagation losses which were neglected. Regarding the coupling parameters, this low Q resonator is over-coupled due to the small gap and the obtained RL. As described in the fabrication section, concise values of RL and gap are tough to know at the gap level without destructive analyses.

The fit is obtained with the equation of the ring resonator considering the phase shift (Eq.2.11):

$$\phi = \frac{2\pi}{\lambda} n_{eff}(T)L(T) = \frac{4\pi^2 n_{eff}(T)R(1 + \alpha\Delta T)}{\lambda} \quad (3.21)$$

with $dn_{eff}/dT = 3.3 \cdot 10^{-4}K^{-1}$ and $\alpha = 10^{-4}K^{-1}$ (Datasheet) for the curve fit. We have decorrelated the efficiency drop of the grating considering a power drop on the measured transmitted power of 15% due to the coupler. The FRR is obtained from the difference of the two effective index at the resonance dips at the two different temperatures $n_{eff}(19.4^\circ C) - n_{eff}(47.9^\circ C) = 1.394 - 1.385 = 0.011$. The obtained value of FRR is in close agreement with the predicted value from Eq.3.17. Moreover, both the expansion of the ring resonator radius with the temperature and the power drop of the grating were taken into account.

3.8 Conclusions about optical measurements

We have analyzed the fabricated structures developing an appropriate test bench for the devices shown in this thesis. Regarding the grating couplers we have measured the angular acceptance and the influence of the temperature on the couplers, which is of primary interest prior to the thermal tuning of ring resonators. We have shown that the efficiency can show power drops between 15% and 40% when temperature span of 50°C are applied to the device. Depending on the angle and operation temperature different coupler responses are observed and understood. Therefore, smooth variations in the output efficiency are expected when the system is set-up at the optimum coupling position. This operation point is optimal to characterize ring resonators with the temperature since it will not interfere with the expected curve of the ring resonator, in which the power will drastically drops close to resonance.

We have shown that thermal tuning is an effective way change materials refractive index . However, thermal stress shears the device a the heat propagation contributes to the overall alignment loss. In addition, polymer devices show dispersion in the obtained data during each measurement, probably due to the deposition of organic agents, remaining solvents and aging. The ellipsometry study carried on UVNIL supports this hypothesis. The values found experimentally agree with the theory developed for the characterization set-up and with the 3D-FDTD simulations. This thermal tuning would be more appropriate to semiconductor devices where the TOC is dominated by changes in polarizability and not changes in the geometrical dimensions. In this case the optical power is measured directly with a photodiode but if optical fibers or grating couplers are used, the effect of the temperature will be even more important since the misalignment between the output fiber and the waveguide will add up to the misalignment equation. This solution is an affordable solution to test OMR, however in addition to the revealed problems related to wafer stability, large scale and fast characterization would requite dedicated heaters such

as Joule heaters, thin metal lines, metal-silicon or ion-implanted silicon lines. These solutions are easily implemented in silicon photonics but in polymer devices it seems a heavy solution for deployable and low cost devices, which in addition only serves to characterization. Alignment, humidity or volatile elements can still contribute to shifts in the resonant wavelength.

Conclusions and further viewpoints

Here, we review the conclusions and perspectives of the main sections discussed in this work. The results and methods explored in this manuscript show large room for improvement in design fabrication and characterization. The perspectives discussed here can be used as a starting point for future works.

Conclusion

Throughout this work, we have demonstrated the patterning of multi-height structures for visible wavelength operation and emphasized OMR to perform absorption sensing based on colorimetric reactions. We have presented an analytical approach for the OMR performance as microspectrometers which had never been addressed. If the OMR waveguides present state-of-the-art propagation losses regardless the platform, the proposed sensitivity indicates an optimum length as occurs with VIS-Spectrometers. Since the sensitivity is dependent on the optical path, larger ring resonators with low losses provide better sensitivities than smaller rings with the same propagation losses. Therefore the use of large ring resonators with long optical paths is suggested. However, we should discuss if it is well worth to enlarge the ring resonator length instead of using coil or serpentine based waveguides. We suggest that it should be determined depending on the integration restrictions. In the case of using a ring, it must be as long as it is permitted by both optical losses and the final application. The calculations have shown how the coupling affects the optical path enhancement. Critical coupling configuration must be avoided since the resulting power contrast is minimum at this point. Over-coupling configuration was proposed as a suitable design rule providing a larger operation region more tolerant against fabrication variations.

With the nanoimprint process shown in this work we were able to pattern centimeter and nano-sized features over large surfaces. In addition coupling structures can be imprinted in the same step avoiding problems related to the quality of the polymer waveguide facets. This process is scalable to micrometer features being possible to use other wavelengths. The patterned devices were coupled with CYTOP bottom claddings for application in liquid sensing. Polymer submicron waveguides formed with grating couplers, have been successfully imprinted with alternative soft-NIL on CYTOP in one single imprint process. Soft stamps with COC8007

(TOPAS) have been fabricated allowing low defect rate due to the low T_g of the thermoplastic material. Such T_g represents an issue when imprinting very large structures with submicron features. The imprinted grating with sub-wavelength periods showed high fidelity compared to the master stamp. Finally, the devices demonstrate a correct operation of grating couplers and tapered waveguides in the visible region. Efficiencies of 1.5% and large angular acceptance width (1.5°) have been achieved from the tested devices at the predicted coupling angles. Structures presenting ring resonators and grating couplers made with ORMOCORE were tested. Among the different solutions, we had tuned the refractive index of the microring resonator with the temperature. Despite successful observation of resonance dips, the results obtained by ellipsometry suggest that this method compromises reproducibility due to the variation of the polymer layer properties in the long term use. We suggest that this behavior is due to the evaporation of remaining solvents in the polymer in addition to the internal stresses created by subsequent temperature cycling.

Perspectives

Before the integration of the sensor elements in the whole system, several issues should be addressed regarding device design, fabrication, and characterization. We propose to consider the next points as a starting point for future works. The design of the master stamp required knowledge on the device performances, the fabrication process, and the considerations about characterization set-up. Regarding the device performance, grating couplers can be improved by adding concentric grooves to improve the adiabatic mode conversion. In a first prototype, we preferred straight lines to ease the demolding of the soft-stamp and focus on the process development. We believe that this kind of curvature at the groove level can produce larger constraints concerning polymer detachment. A deep etched reflector behind the grating grooves can also enhance the efficiency. However, it will involve additional etching steps. Regarding the grating periods, we suggest the arrangement of geometries providing near-vertical coupling. Large coupling angles should be avoided because it will enlarge the laser spot providing an elliptical shape of the input spot beam. Moreover, increasing parasitic reflection to the detection elements. The same applies to counter propagative coupling. If the double grating coupler configuration is selected we suggest to set two different grating periods allowing both counter-propagative and co-propagative coupling. Preferably the shorter period should be used to perform the input coupling while the larger period must be preferred to perform the output coupling. By this way, we avoid optical fiber overlap during characterization.

Regarding the ring resonator design based on the absorption scheme we propose large ring radius for future designs. Larger rings offer two main advantages: the first one is to provide closely spaced resonances which is beneficial to quickly tune the

resonances (with a tunable source) improving the dynamic of the ring resonator; the second advantage concerns the gap of the ring resonator. As the ring becomes larger the gap region is seen by the guided mode as a directional coupler. For this reason the coupling region is larger when the ring resonator radius is increased. This applies for both laterally coupled ring resonator and vertically coupled ring resonator. Also, racetrack structures can be implemented to enhance the optical path and increase the gap between the ring and the waveguide, it will also enhance the optical path increasing the sensitivity. Several issues were revealed during the fabrication of the devices. The EBL was optimized to match our dimensions, similar optimizations can be done with other writing strategies, for example in order to write very long waveguides alternative (and expensive) vector scan modules are implemented in the machine. By doing this, the wafer is continuously exposed reducing the EBL time and the cost. Combining both a vector scan exposure with gray scale lithography will dramatically reduce the price per chip of the master stamp. Regarding the intermediate soft stamp the thermo-mechanical expansion was a important concern since the smaller gaps can shift or disappear; however, if large ring resonators and large gaps are preferred this problem will be drastically minimized. As an alternative, we can always manufacture soft stamps combining different types of hard materials and elastomers. Concerning the fabrication of the grating coupler, several implementations can be done such as bottom metallic reflectors or metallic gratings on the CYTOP surface which would increase the index contrast and thus, the efficiency. However, each metallic grating must be patterned individually with EBL.

Future works are oriented towards the study of coupled ring resonators on CYTOP and the performance of these devices for liquid sensing. As the main problem is the characterization of the resonator at fixed wavelength, we proposed an alternative method to tune the ring resonances compatible with the operation as a sensor. The resonance tuning system would be based on a microfluidic cell to adjust the refractive index of the top cladding. Two liquids having different refractive index (water $n=1.33$, and polyethyleneGlycol $n=1.47$) which can be mixed before injection in the microfluidic circuit. The proposed microfluidic set-up is detailed in the figure shown bellow. The inset shows a 3D image of the microfluidic channel. This sketch shows the main set-up to perform both the optical characterization of microring resonators at a fixed wavelength and the performance as sensors. Indeed, we introduce two liquids inside the microfluidic mixer, resulting one liquid of refractive index proportional to the concentration of the solution. Then, the mixed liquid flows into the microfluidic channel passing atop the ring resonator.

The microfluidic channel is specially conceived to allow on-chip coupling by both sides of the channel through the grating couplers. The characterization can be performed changing the proportion of the two liquids while the power is collected at the output. The variation in the top refractive index will tune the effective index of the waveguide core sweeping between the different resonances as we have done

with the temperature. Moreover, the input liquid can be adapted to provide controlled lossy claddings by means of the appropriate colorimetric reactions injected in the channel. In this case, the limit of detection will come from the accuracy of the injected concentration which depends on the liquid pump and the exact concentration of the input liquid made by the operator. Complementary characterizations can be done by varying the speed which the liquid covers the ring. A measurement of the ratio of the ring covered by the liquid also provides an effective ring characterization without the need of tunable sources. The optimal starting points to continue

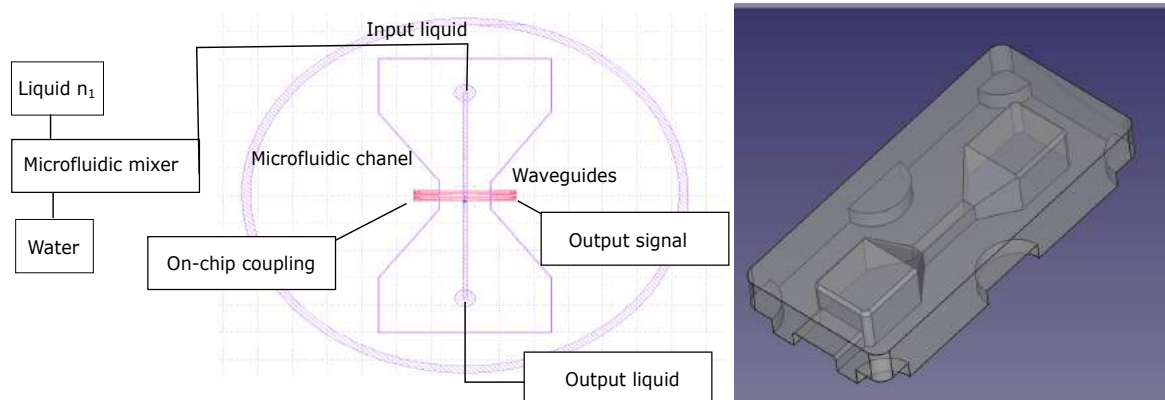


Figure: Sketch of the proposed set-up for the sensing experiments. The refractive index of the liquid is varied in-situ by means of the fluidic pumps and the mixer. The liquid is brought to the optical chip inside the microfluidic channel.

this work are stated as follows:

- We propose very large ring resonators $R \approx 100\mu m$ with large gap dimensions to ease the replication in the soft stamp ($\approx 200nm - 300nm$). Two grating coupler configuration is preferred. Coupling efficiency can be improved but is not the main objective of the work.
- We propose the same fabrication process compatible with the appropriate gap ($\approx 200nm - 300nm$). A study of polymer aging is recommended.
- If the wavelength is fixed we propose a refractive index cladding tuning based on microfluidic handling.

We have demonstrated theoretically the potential use of microring resonator as VIS-microspectrometers with an application based on the detection of small concentration of Hexavalent Chromium. Moreover we have shown that ring resonators and grating couplers can be easily fabricated with low cost fabrication methods. Further efforts must be addressed to the device characterization regarding the future integration within small packages.

Appendix A

EBL parameters

Design

GDSII file: \\pongo\VE-BEAM\DiezGarciaMiguel\CarcenacFranck\26-02-2018-Moule2Niv1Expo.gds
 GDSII structure: Expose
 GDSII layer(s): 1,10-11
 Writefield size: 100 μm ;
 Working area: (4950; 7250) to (11050; 9250) μm
 Dose factor (defined in Positionlist): 1

Coordinates

Stage X, Y, Z in mm: (21.936469, 5.803903, 17.594133)
 Global U, V, W in mm: (7.000000, 9.000000, 6.999914) → used
 Local U, V in mm: (7.000000, 9.000000)

Column parameters

Magnification: 1000 \times
 Working distance: 7.043 mm
 Voltage: 30.000 kV
 Aperture: 20 μm
 Beam current: 0.132701 nA

Patterning parameters

Areas

Step size: 0.01 μm
 Line spacing: 0.01 μm
 Dwell time: 0.003014 ms
 Beam speed: 3.318 mm/s
 Nominal dose: 400.000 $\mu\text{C}/\text{cm}^2$
 Calculated dose: 399.961 $\mu\text{C}/\text{cm}^2$

Curved Elements

Enabled: ON
 Step size: 0.01 μm
 Line spacing: 0.01 μm
 Dwell time: 0.003014 ms
 Beam speed: 3.318 mm/s
 Nominal dose: 400.000 $\mu\text{C}/\text{cm}^2$
 Calculated dose: 399.961 $\mu\text{C}/\text{cm}^2$

Single Pixel Lines

Enabled: ON
 Step size: 0.002 μm
 Dwell time: 0.00015 ms
 Beam speed: 13.333 mm/s
 Nominal dose: 100.000 $\mu\text{C}/\text{cm}$
 Calculated dose: 99.526 $\mu\text{C}/\text{cm}$

Figure: Configuration of the EBL tool for the double exposure patterning

References

- [1] Manju Bhargavi Gumpu et al. "A review on detection of heavy metal ions in water—An electrochemical approach". In: *Sensors and actuators B: chemical* 213 (2015), pp. 515–533.
- [2] COB Okoye et al. "Simultaneous ultraviolet-visible (UVVIS) spectrophotometric quantitative determination of Pb, Hg, Cd, As and Ni ions in aqueous solutions using cyanidin as a chromogenic reagent". In: *International Journal of Physical Sciences* 8.3 (2013), pp. 98–102.
- [3] CW Jenkins, RB King, and I Bresinska. *Synthesis of Polystyrene-Supported Dithi-zone Analogues for Use as Chemical Sensors for Heavy Metals*. Tech. rep. Westinghouse Savannah River Company, Aiken, SC (United States); Westinghouse Savannah River Co., Aiken, SC (United States), 1998.
- [4] Grenville Robinson. "The commercial development of planar optical biosensors". In: *Sensors and Actuators B: Chemical* 29.1-3 (1995), pp. 31–36.
- [5] Vittorio Passaro et al. "Recent advances in integrated photonic sensors". In: *Sensors* 12.11 (2012), pp. 15558–15598.
- [6] Tomoyuki Yoshie, Lingling Tang, and Shu-Yu Su. "Optical microcavity: sensing down to single molecules and atoms". In: *Sensors* 11.2 (2011), pp. 1972–1991.
- [7] Ofer Bar-On et al. "High Quality 3D Photonics using Nano Imprint Lithography of Fast Sol-gel Materials". In: *Scientific reports* 8.1 (2018), p. 7833.
- [8] C Ciminelli et al. "High performance SOI microring resonator for biochemical sensing". In: *Optics & laser technology* 59 (2014), pp. 60–67.
- [9] Katrien De Vos et al. "Silicon-on-Insulator microring resonator for sensitive and label-free biosensing". In: *Optics express* 15.12 (2007), pp. 7610–7615.
- [10] Pauline Girault et al. "Integrated polymer micro-ring resonators for optical sensing applications". In: *Journal of Applied Physics* 117.10 (2015), p. 104504.
- [11] Romain Guider et al. "Sensitivity and Limit of Detection of biosensors based on ring resonators". In: *Sensing and bio-sensing research* 6 (2015), pp. 99–102.
- [12] Christopher C Evans, Chengyu Liu, and Jin Suntivich. "TiO₂ nanophotonic sensors for efficient integrated evanescent Raman spectroscopy". In: *ACS Photonics* 3.9 (2016), pp. 1662–1669.

- [13] Hao Li et al. "Superconducting nanowire single photon detector at 532 nm and demonstration in satellite laser ranging". In: *Optics Express* 24.4 (2016), pp. 3535–3542.
- [14] Vittorio MN Passaro et al. "Photonic resonant microcavities for chemical and biochemical sensing". In: *RSC Advances* 3.1 (2013), pp. 25–44.
- [15] Iñigo Artundo. "Photonic Integration: New Applications Are Visible". In: *Optik & Photonik* 12.3 (2017), pp. 22–25.
- [16] Righab Hamdan et al. "Optical coherence tomography: from physical principles to clinical applications". In: *Archives of cardiovascular diseases* 105.10 (2012), pp. 529–534.
- [17] James G Fujimoto et al. "Optical coherence tomography: an emerging technology for biomedical imaging and optical biopsy". In: *Neoplasia (New York, NY)* 2.1-2 (2000), p. 9.
- [18] BI Akca et al. "Miniature spectrometer and beam splitter for an optical coherence tomography on a silicon chip". In: *Optics express* 21.14 (2013), pp. 16648–16656.
- [19] Ji Yi et al. "Visible light optical coherence tomography measures retinal oxygen metabolic response to systemic oxygenation". In: *Light: Science & Applications* 4.9 (2015), e334.
- [20] Miguel A Pérez, Olaya González, and José R Arias. "Optical fiber sensors for chemical and biological measurements". In: *Current Developments in Optical Fiber Technology*. InTech, 2013.
- [21] Steven R Cordero et al. "A distributed fiber optic chemical sensor for hydrogen cyanide detection". In: *Advanced Environmental, Chemical, and Biological Sensing Technologies III*. Vol. 5993. International Society for Optics and Photonics. 2005, p. 599302.
- [22] Chen-Shane Chu and Yu-Lung Lo. "Fiber-optic carbon dioxide sensor based on fluorinated xerogels doped with HPTS". In: *Sensors and Actuators B: Chemical* 129.1 (2008), pp. 120–125.
- [23] Mohammad F Khanfar, Wisam Al-Faqheri, Ala?aldeen Al-Halhouli, et al. "Low Cost Lab on Chip for the Colorimetric Detection of Nitrate in Mineral Water Products". In: *Sensors* 17.10 (2017), p. 2345.
- [24] Jessica Godin et al. "Microfluidics and photonics for Bio-System-on-a-Chip: A review of advancements in technology towards a microfluidic flow cytometry chip". In: *Journal of biophotonics* 1.5 (2008), pp. 355–376.
- [25] Min Bai et al. "A compact photometer based on metal-waveguide-capillary: application to detecting glucose of nanomolar concentration". In: *Scientific reports* 5 (2015), p. 10476.

- [26] Jiqing Ye et al. "Highly sensitive detection of thrombin using metal-waveguide-capillary based photometer and gold nanorods probe". In: *Sensors and Actuators B: Chemical* 243 (2017), pp. 1255–1260.
- [27] Carlos Angulo Barrios. "Rapid On-Site Formation of a Free-Standing Flexible Optical Link for Sensing Applications". In: *Sensors* 16.10 (2016), p. 1643.
- [28] Yuze Sun and Xudong Fan. "Optical ring resonators for biochemical and chemical sensing". In: *Analytical and bioanalytical chemistry* 399.1 (2011), pp. 205–211.
- [29] Matthew White Royal, Nan M Jokerst, and Richard B Fair. "Droplet-based sensing: optical microresonator sensors embedded in digital electrowetting microfluidics systems". In: *IEEE Sensors Journal* 13.12 (2013), pp. 4733–4742.
- [30] Chung-Yen Chao, Wayne Fung, and L Jay Guo. "Polymer microring resonators for biochemical sensing applications". In: *IEEE journal of selected topics in quantum electronics* 12.1 (2006), pp. 134–142.
- [31] Miguel Diez et al. "Direct patterning of polymer optical periodic nanostructures on CYTOP for visible light waveguiding". In: *Optical Materials* 82 (2018), pp. 21–29.
- [32] Farida Meziane et al. "Study of a polymer optical microring resonator for hexavalent chromium sensing". In: *Sensors and Actuators B: Chemical* 209 (2015), pp. 1049–1056.
- [33] Yang Wang et al. "Determination of trace chromium (VI) using a hollow-core metal-cladding optical waveguide sensor". In: *Optics Express* 21.25 (2013), pp. 31130–31137.
- [34] Arthur Nitkowski, Antje Baeumner, and Michal Lipson. "On-chip spectrophotometry for bioanalysis using microring resonators". In: *Biomedical optics express* 2.2 (2011), pp. 271–277.
- [35] Roel GF Baets et al. "Silicon Photonics: silicon nitride versus silicon-on-insulator". In: *Optical Fiber Communication Conference*. Optical Society of America. 2016, Th3J–1.
- [36] Sebastian Romero-Garcia et al. "Silicon nitride CMOS-compatible platform for integrated photonics applications at visible wavelengths". In: *Optics express* 21.12 (2013), pp. 14036–14046.
- [37] Gloria Micó et al. "Silicon nitride photonics: from visible to mid-infrared wavelengths". In: *Silicon Photonics XIII*. Vol. 10537. International Society for Optics and Photonics. 2018, 105370B.
- [38] Arne Leinse et al. "TriPleX™ platform technology for photonic integration: Applications from UV through NIR to IR". In: *Information Photonics (IP), 2011 ICO International Conference on*. IEEE. 2011, pp. 1–2.

- [39] GAJ Besselink et al. "Performance of arrayed microring resonator sensors with the TriPleX platform". In: *Biosens. Bioelectron* 7 (2016), p. 2.
- [40] Farshid Ghasemi et al. "Multiplexed detection of lectins using integrated glycan-coated microring resonators". In: *Biosensors and Bioelectronics* 80 (2016), pp. 682–690.
- [41] Farshid Ghasemi et al. "Self-referenced silicon nitride array microring biosensor for toxin detection using glycans at visible wavelength". In: *Nanoscale Imaging, Sensing, and Actuation for Biomedical Applications X*. Vol. 8594. International Society for Optics and Photonics. 2013, 85940A.
- [42] Chantal Paquet and Eugenia Kumacheva. "Nanostructured polymers for photonics". In: *Materials Today* 11.4 (2008), pp. 48–56.
- [43] Fabian Dortu et al. "Composite polymeric-inorganic waveguide fabricated by injection molding for biosensing applications". In: *Transparent Optical Networks (ICTON), 2014 16th International Conference on*. IEEE. 2014, pp. 1–4.
- [44] Maria Nordström et al. "Single-mode waveguides with SU-8 polymer core and cladding for MOEMS applications". In: *Journal of Lightwave Technology* 25.5 (2007), pp. 1284–1289.
- [45] Camille Delezoide et al. "Vertically coupled polymer microracetrack resonators for label-free biochemical sensors". In: *IEEE Photonics Technology Letters* 24.4 (2012), pp. 270–272.
- [46] Bjorn Agnarsson et al. "Fabrication of planar polymer waveguides for evanescent-wave sensing in aqueous environments". In: *Microelectronic Engineering* 87.1 (2010), pp. 56–61.
- [47] Andreas Finn. "Direct Patterning of Optical Coupling Devices in Polymer Waveguides". PhD thesis. Saechsische Landesbibliothek-Staats-und Universitaetsbibliothek Dresden, 2014.
- [48] Matthew Mancuso, Julie M Goddard, and David Erickson. "Nanoporous polymer ring resonators for biosensing". In: *Optics express* 20.1 (2012), pp. 245–255.
- [49] Paolo Bettotti et al. "Modeling of slot waveguide sensors based on polymeric materials". In: *Sensors* 11.8 (2011), pp. 7327–7340.
- [50] Rodica Morarescu et al. "Fabrication and characterization of high-optical-quality-factor hybrid polymer microring resonators operating at very near infrared wavelengths". In: *IEEE Photonics Journal* 8.2 (2016), pp. 1–9.
- [51] Marianne Hiltunen et al. "Polymeric slot waveguide interferometer for sensor applications". In: *Optics Express* 22.6 (2014), pp. 7229–7237.
- [52] Marianne Hiltunen et al. "Polymeric slot waveguide at visible wavelength". In: *Optics letters* 37.21 (2012), pp. 4449–4451.

- [53] Muhammad HM Salleh et al. "Polymer dual ring resonators for label-free optical biosensing using microfluidics". In: *Chemical Communications* 49.30 (2013), pp. 3095–3097.
- [54] Koji Matsubara, Satoshi Kawata, and Shigeo Minami. "Optical chemical sensor based on surface plasmon measurement". In: *Applied Optics* 27.6 (1988), pp. 1160–1163.
- [55] Yan Deng et al. "Tunable and high-sensitivity sensing based on Fano resonance with coupled plasmonic cavities". In: *Scientific Reports* 7.1 (2017), p. 10639.
- [56] CR Lavers and JS Wilkinson. "A waveguide-coupled surface-plasmon sensor for an aqueous environment". In: *Sensors and Actuators B: Chemical* 22.1 (1994), pp. 75–81.
- [57] Zouheir Sekkat et al. "Plasmonic coupled modes in metal-dielectric multilayer structures: Fano resonance and giant field enhancement". In: *Optics express* 24.18 (2016), pp. 20080–20088.
- [58] Shinji Hayashi, Dmitry V Nesterenko, and Zouheir Sekkat. "Fano resonance and plasmon-induced transparency in waveguide-coupled surface plasmon resonance sensors". In: *Applied Physics Express* 8.2 (2015), p. 022201.
- [59] Tianye Huang et al. "Fano Resonance Enhanced Surface Plasmon Resonance Sensors Operating in Near-Infrared". In: *Photonics*. Vol. 5. 3. Multidisciplinary Digital Publishing Institute. 2018, p. 23.
- [60] Kristof Lodewijks et al. "Tuning the Fano resonance between localized and propagating surface plasmon resonances for refractive index sensing applications". In: *Plasmonics* 8.3 (2013), pp. 1379–1385.
- [61] Kuang-Li Lee et al. "Ultrasensitive biosensors using enhanced Fano resonances in capped gold nanoslit arrays". In: *Scientific reports* 5 (2015), p. 8547.
- [62] Farida Meziane. "Etude de microrésonateurs optiques polymères en anneaux en vue de leur intégration sur une plateforme de microfluidique digitale: application à la détection d'ions métalliques de Cr (VI) dans l'eau". PhD thesis. Bordeaux, 2016.
- [63] Arthur Nitkowski. "Cavity-Enhanced Nanophotonic Spectroscopy In Optofluidic Devices". In: (2011).
- [64] CM Sotomayor Torres et al. "Nanoimprint lithography: an alternative nanofabrication approach". In: *Materials Science and Engineering: C* 23.1-2 (2003), pp. 23–31.
- [65] Canet Acikgoz et al. "Polymers in conventional and alternative lithography for the fabrication of nanostructures". In: *European Polymer Journal* 47.11 (2011), pp. 2033–2052.

- [66] Giuseppe A Cirino et al. "Simulation and fabrication of silicon nitride microring resonator by DUV lithography". In: *Microelectronics Technology and Devices (SBMicro), 2016 31st Symposium on*. IEEE. 2016, pp. 1–4.
- [67] A Ramachandran et al. "A universal biosensing platform based on optical micro-ring resonators". In: *Biosensors and Bioelectronics* 23.7 (2008), pp. 939–944.
- [68] Lloyd R Harriott. "Limits of lithography". In: *Proceedings of the IEEE* 89.3 (2001), pp. 366–374.
- [69] Yifang Chen. "Nanofabrication by electron beam lithography and its applications: a review". In: *Microelectronic Engineering* 135 (2015), pp. 57–72.
- [70] Ampere A Tseng et al. "Electron beam lithography in nanoscale fabrication: recent development". In: *IEEE Transactions on electronics packaging manufacturing* 26.2 (2003), pp. 141–149.
- [71] Kezheng Li et al. "High speed e-beam writing for large area photonic nanostructures—a choice of parameters". In: *Scientific reports* 6 (2016), p. 32945.
- [72] Vincent M Donnelly and Avinoam Kornblit. "Plasma etching: Yesterday, today, and tomorrow". In: *Journal of Vacuum Science & Technology A: Vacuum, Surfaces, and Films* 31.5 (2013), p. 050825.
- [73] Sandra Gilles et al. "UV nanoimprint lithography with rigid polymer molds". In: *Microelectronic engineering* 86.4-6 (2009), pp. 661–664.
- [74] Hongbo Lan and Yucheng Ding. "Nanoimprint lithography". In: *Lithography*. InTech, 2010.
- [75] Lei Chen et al. "Defect control in nanoimprint lithography". In: *Journal of Vacuum Science & Technology B: Microelectronics and Nanometer Structures Processing, Measurement, and Phenomena* 23.6 (2005), pp. 2933–2938.
- [76] Zhaoning Yu, He Gao, and Stephen Y Chou. "In situ real time process characterization in nanoimprint lithography using time-resolved diffractive scatterometry". In: *Applied Physics Letters* 85.18 (2004), pp. 4166–4168.
- [77] Kazutomo Osari et al. "Evaluation of filling behavior on UV nanoimprint lithography using release coating". In: *Microelectronic Engineering* 87.5-8 (2010), pp. 918–921.
- [78] Rémi Courson et al. "SAMs vapor deposition: a ready to use functionalization technology for monitoring wettability properties in microfluidic devices". In: *The 18th International Conference on Miniaturized Systems for Chemistry and Life Sciences (MicroTAS 2014)*. 2014.
- [79] Weimin Zhou et al. "Characterization of anti-adhesive self-assembled monolayer for nanoimprint lithography". In: *Applied Surface Science* 255.5 (2008), pp. 2885–2889.

- [80] Kristjan Leosson and Björn Agnarsson. "Integrated biophotonics with CYTOP". In: *Micromachines* 3.1 (2012), pp. 114–125.
- [81] Richard Daviau et al. "Fabrication of surface plasmon waveguides and integrated components on Cytop". In: *Microelectronic Engineering* 87.10 (2010), pp. 1914–1921.
- [82] Savas Kaya et al. "A systematic study of plasma activation of silicon surfaces for self assembly". In: *ACS applied materials & interfaces* 7.45 (2015), pp. 25024–25031.
- [83] Tommi Suni et al. "Effects of plasma activation on hydrophilic bonding of Si and SiO₂". In: *Journal of the Electrochemical Society* 149.6 (2002), G348–G351.
- [84] Joyce KS Poon et al. "Polymer microring coupled-resonator optical waveguides". In: *Journal of Lightwave Technology* 24.4 (2006), p. 1843.
- [85] Teri W Odom et al. "Improved pattern transfer in soft lithography using composite stamps". In: *Langmuir* 18.13 (2002), pp. 5314–5320.
- [86] Emmanuel Delamarche et al. "Stability of molded polydimethylsiloxane microstructures". In: *Advanced Materials* 9.9 (1997), pp. 741–746.
- [87] Zhiwei Li et al. "Hybrid nanoimprint- soft lithography with sub-15 nm resolution". In: *Nano letters* 9.6 (2009), pp. 2306–2310.
- [88] Yonggang Y Huang et al. "Stamp collapse in soft lithography". In: *Langmuir* 21.17 (2005), pp. 8058–8068.
- [89] Colleen E O'Neil et al. "Characterization of activated cyclic olefin copolymer: effects of ethylene/norbornene content on the physiochemical properties". In: *Analyst* 141.24 (2016), pp. 6521–6532.
- [90] Zahra Faraji Rad et al. "High-fidelity replication of thermoplastic microneedles with open microfluidic channels". In: *Microsystems & Nanoengineering* 3 (2017), p. 17034.
- [91] J Gaudioso and HG Craighead. "Characterizing electroosmotic flow in microfluidic devices". In: *Journal of Chromatography A* 971.1-2 (2002), pp. 249–253.
- [92] Jessienta Anthony et al. "Characterization of a microstructured Zeonex terahertz fiber". In: *JOSA B* 28.5 (2011), pp. 1013–1018.
- [93] Getinet Woyessa et al. "Zeonex-PMMA microstructured polymer optical FBGs for simultaneous humidity and temperature sensing". In: *Optics letters* 42.6 (2017), pp. 1161–1164.
- [94] T Nielsen et al. "Nanoimprint lithography in the cyclic olefin copolymer, Topas®, a highly ultraviolet-transparent and chemically resistant thermoplast". In: *Journal of Vacuum Science & Technology B: Microelectronics and Nanometer Structures Processing, Measurement, and Phenomena* 22.4 (2004), pp. 1770–1775.

- [95] Dan Mario Johansen. "Investigation of Topas® for use in optical components". MA thesis. Technical University of Denmark, DTU, DK-2800 Kgs. Lyngby, Denmark, 2005.
- [96] C Gourgon et al. "Study of the behaviour of monomers in thermal nanoimprint lithography". In: *Microelectronic Engineering* 87.5-8 (2010), pp. 1024–1028.
- [97] Sung-Won Youn et al. "Microstructuring of SU-8 photoresist by UV-assisted thermal imprinting with non-transparent mold". In: *Microelectronic Engineering* 85.9 (2008), pp. 1924–1931.
- [98] Sung-Won Youn et al. "Microstructuring of 45- μm -Deep Dual Damascene Openings in SU-8/Si by UV-Assisted Thermal Imprinting with Opaque Mold". In: *Japanese Journal of Applied Physics* 48.6S (2009), 06FH09.
- [99] JiHyeong Ryu et al. "A modified squeeze equation for predicting the filling ratio of nanoimprint lithography". In: *Nano convergence* 4.1 (2017), p. 14.
- [100] Harry D Rowland et al. "Impact of polymer film thickness and cavity size on polymer flow during embossing: toward process design rules for nanoimprint lithography". In: *Journal of Micromechanics and Microengineering* 15.12 (2005), p. 2414.
- [101] Ji Hyeong Ryu et al. "Polymer filling behaviors with various levels of imprinting velocity in nanoimprint lithography". In: *Microelectronic Engineering* 117 (2014), pp. 67–71.
- [102] Harry D Rowland et al. "Simulations of nonuniform embossing: The effect of asymmetric neighbor cavities on polymer flow during nanoimprint lithography". In: *Journal of Vacuum Science & Technology B: Microelectronics and Nanometer Structures Processing, Measurement, and Phenomena* 23.6 (2005), pp. 2958–2962.
- [103] Linghua Wang et al. "A label-free optical biosensor built on a low-cost polymer platform". In: *IEEE Photonics Journal* 4.3 (2012), pp. 920–930.
- [104] FDTD Lumerical. *Solutions*. 2016.
- [105] Jean-Pierre Berenger. "A perfectly matched layer for the absorption of electromagnetic waves". In: *Journal of computational physics* 114.2 (1994), pp. 185–200.
- [106] Richard R Grote and Lee C Bassett. "Single-mode optical waveguides on native high-refractive-index substrates". In: *APL Photonics* 1.7 (2016), p. 071302.
- [107] Amnon Yariv and Pochi Yeh. *Photonics*. 2007.
- [108] Lukas Chrostowski and Michael Hochberg. *Silicon photonics design: from devices to systems*. Cambridge University Press, 2015.
- [109] Peter Bienstman. "Rigorous and efficient modelling of wavelength scale photonic components". PhD thesis. Ghent University, 2001.

- [110] Katsunari Okamoto. *Fundamentals of optical waveguides*. Academic press, 2006.
- [111] John C Brazas and Lifeng Li. "Analysis of input-grating couplers having finite lengths". In: *Applied optics* 34.19 (1995), pp. 3786–3792.
- [112] Theodor Tamir and Song-Tsuen Peng. "Analysis and design of grating couplers". In: *Applied physics* 14.3 (1977), pp. 235–254.
- [113] Francisco Javier Salgado-Remacha, Luis Miguel Sanchez-Brea, and Eusebio Bernabeu. "Effect of fill-factor on the Talbot effect of diffraction gratings". In: *Journal of the European Optical Society-Rapid publications* 6 (2011).
- [114] Wei-Hsuan Hsu, Hong Hocheng, and Jow-Tsong Shy. "A method for in situ measurement of residual layer thickness in nano-imprint lithography". In: *Microelectronic Engineering* 110 (2013), pp. 132–140.
- [115] Xiuguo Chen et al. "Accurate characterization of nanoimprinted resist patterns using Mueller matrix ellipsometry". In: *Optics Express* 22.12 (2014), pp. 15165–15177.
- [116] Wim Bogaerts et al. "Silicon microring resonators". In: *Laser & Photonics Reviews* 6.1 (2012), pp. 47–73.
- [117] Chung-Yen Chao and L Jay Guo. "Design and optimization of microring resonators in biochemical sensing applications". In: *Journal of Lightwave Technology* 24.3 (2006), pp. 1395–1402.
- [118] Arthur Nitkowski, Long Chen, and Michal Lipson. "Cavity-enhanced on-chip absorption spectroscopy using microring resonators". In: *Optics express* 16.16 (2008), pp. 11930–11936.
- [119] Junbo Gong et al. "Temperature dependent optical constants for SiO₂ film on Si substrate by ellipsometry". In: *Materials Research Express* 4.8 (2017), p. 085005.
- [120] Martin A Green. "Self-consistent optical parameters of intrinsic silicon at 300 K including temperature coefficients". In: *Solar Energy Materials and Solar Cells* 92.11 (2008), pp. 1305–1310.
- [121] Larry R Dalton et al. *Organic Electro-Optics and Photonics: Molecules, Polymers and Crystals*. Cambridge University Press, 2015.
- [122] Shuwen Guo et al. "Determination of refractive index and thickness of thick transparent films by variable-angle spectroscopic ellipsometry: application to benzocyclobutene films". In: *Applied optics* 35.10 (1996), pp. 1693–1699.
- [123] Zhiyi Zhang et al. "Thermo-optic coefficients of polymers for optical waveguide applications". In: *Polymer* 47.14 (2006), pp. 4893–4896.
- [124] Thomas Wood et al. "Comparison of refractive indices measured by m-lines and ellipsometry: application to polymer blend and ceramic thin films for gas sensors". In: *Instrumentation, Metrology, and Standards for Nanomanufacturing, Optics, and Semiconductors VI*. Vol. 8466. International Society for Optics and Photonics. 2012, 84660T.

- [125] R Ulrich and R Torge. "Measurement of thin film parameters with a prism coupler". In: *Applied Optics* 12.12 (1973), pp. 2901–2908.
- [126] S Morino et al. "Photoinduced refractive index change and birefringence in poly (methyl methacrylate) containing p-(dimethylamino) azobenzene". In: *The Journal of Physical Chemistry* 99.25 (1995), pp. 10280–10284.
- [127] Takashi Miyoshi et al. "510–515 nm InGaN-based green laser diodes on c-plane GaN substrate". In: *Applied Physics Express* 2.6 (2009), p. 062201.
- [128] Adrian Avramescu et al. "True green laser diodes at 524 nm with 50 mW continuous wave output power on c-plane GaN". In: *Applied physics express* 3.6 (2010), p. 061003.
- [129] Mingjun Chi, Ole Bjarlin Jensen, and Paul Michael Petersen. "Green high-power tunable external-cavity GaN diode laser at 515 nm". In: *Optics letters* 41.18 (2016), pp. 4154–4157.
- [130] Rainer Michalzik. *VCSELs: fundamentals, technology and applications of vertical-cavity surface-emitting lasers*. Vol. 166. Springer, 2012.
- [131] KS Kaur et al. "Flip-chip assembly of VCSELs to silicon grating couplers via laser fabricated SU8 prisms". In: *Optics Express* 23.22 (2015), pp. 28264–28270.
- [132] Haohua Tu and Stephen A Boppart. "Coherent fiber supercontinuum for biophotonics". In: *Laser & photonics reviews* 7.5 (2013), pp. 628–645.
- [133] Oussama Mhibik et al. "Broadly tunable (440–670 nm) solid-state organic laser with disposable capsules". In: *Applied Physics Letters* 102.4 (2013), p. 041112.
- [134] Ralf Waldhäusl et al. "Efficient coupling into polymer waveguides by gratings". In: *Applied optics* 36.36 (1997), pp. 9383–9390.
- [135] Rodica Morarescu et al. "Polymer microring resonators for biosensing applications by nanoimprint lithography". In: *Transparent Optical Networks (IC-TON), 2015 17th International Conference on*. IEEE. 2015, pp. 1–4.
- [136] Chun-Ta Wang et al. "Electrically tunable high Q-factor micro-ring resonator based on blue phase liquid crystal cladding". In: *Optics express* 22.15 (2014), pp. 17776–17781.
- [137] Brett Maune et al. "Electrically tunable ring resonators incorporating nematic liquid crystals as cladding layers". In: *Applied Physics Letters* 83.23 (2003), pp. 4689–4691.
- [138] Uriel Levy et al. "On-chip microfluidic tuning of an optical microring resonator". In: *Applied physics letters* 88.11 (2006), p. 111107.
- [139] Romi Shamai and Uriel Levy. "On chip tunable micro ring resonator actuated by electrowetting". In: *Optics express* 17.2 (2009), pp. 1116–1125.
- [140] Benjamin Reig et al. "Study of SU-8 reliability in wet thermal ambient for application to polymer micro-optics on VCSELs". In: *Japanese Journal of Applied Physics* 53.8S2 (2014), p. 08MC03.